Tore Skauge Bysting

Simulation of the Impurity Photovoltaic Effect in GaAs Solar Cells

Master's thesis in Nanotechnology
Supervisor: Turid Reenaas
December 2021

Master's thesis

NTNU
Norwegian University of Science and Technology
Faculty of Natural Sciences
Department of Physics

Norwegian University of
Science and Technology

Tore Skauge Bysting

Simulation of the Impurity Photovoltaic Effect in GaAs Solar Cells

Master's thesis in Nanotechnology
Supervisor: Turid Reenaas
December 2021

Norwegian University of Science and Technology
Faculty of Natural Sciences
Department of Physics

NTNU
Norwegian University of
Science and Technology

Preface

This master's thesis concludes my Master's Degree Programme in Nanotechnology at the Norwegian University of Science and Technology (NTNU) in Trondheim, Norway. The work was carried out at the Department of Physics, under the supervision of Professor Turid Reenaas.

The master's thesis follows my specialization project report, "Numerical Simulation of Single Junction GaAs Solar Cell Performance Using SCAPS", a report written on a topic closely related to that of the master's thesis. As such, I've had the opportunity to keep learning about solar cells and how to use simulation as a tool for improving their performance. Although the work has been both challenging and stressful at times, the process has also been rewarding. I've developed my interest for solar cells and, more generally, my motivation for finding solutions that could help improve the future climate.

I acknowledge Honorary Professor Marc Burgelman and former coworkers Koen Decock, Johan Verschraegen, Alex Niemegeers and Stefaan Degrave for the use of the simulation software SCAPS. A special thanks goes to Marc Burgelman for support and great answers to my questions about SCAPS.

I would like to express my utmost gratitude to my supervisor, Turid Reenaas. She has been of great help, and I am grateful for both constructive discussions and friendly conversations. Through great patience and continuous encouragement she has helped me reach my goal of finishing my studies. I have also received much help with the practical aspects of writing the master's thesis and would like to thank the student advisor of my study program, Brit Wenche Meland, for that. I am deeply grateful for the support of my family, and my parents in particular. Throughout my studies, and especially during the writing of this thesis, they have always been there for me. They deserve a great amount of credit for helping me get to where I am today.

Tore Skauge Bysting
Lørenskog, December 2021

Abstract

In this work, numerical simulations are performed for GaAs solar cells into which deep level impurities are introduced. Such impurities typically act as detrimental recombination centers. However, they can also enable charge carriers to be optically excited in a two-step process from the valence band to the impurity level and from the impurity level to the conduction band, thereby contributing to the photogenerated current. This is known as the impurity photovoltaic (IPV) effect and opens up for utilizing a wider range of the incident radiation, as also photons with energy lower than the main band gap of the cell material can be absorbed.

The solar cell simulation software SCAPS is used for the simulations. In this master project, this software is first evaluated as a tool for simulation of the IPV effect. It is found to be a suitable software for such simulations. SCAPS has a broad functionality, also when it comes to the IPV effect. The mechanism of photon recycling is, however, not included.

Subsequently, SCAPS is used to study the influence of a set of material and design parameters on the performance of the solar cells. These parameters include the photo-ionization cross sections, the thermal capture cross sections, the type of the impurities, shallow background doping and light trapping. The photo-ionization cross sections must be varied over several orders of magnitude to have a noteworthy impact on the cell performance. The thermal capture cross sections are also varied in a logarithmic manner and have a large influence on the cell performance. A suitable combination of impurity type and shallow background doping density has the potential to improve the cell performance. Finally, a high degree of light trapping is found to be essential for the gain of the IPV effect to outweigh the increased recombination associated with the deep level impurities.

Of all the solar cells simulated in this work (except for one cell which credibility is reduced by numerical issues), the highest conversion efficiency obtained is 33.5 %. This is achieved for a cell with maximum light trapping and acceptor type deep level impurities, partly compensated by donor type shallow background doping. A similar cell with no deep level impurities is found to have an efficiency of 28.2 %. If maximum light trapping can be achieved, this indicates a great potential for solar cells with the IPV effect. However, the efficiency of the cells decreases drastically when poorer light trapping is applied.

Sammendrag

I dette arbeidet, gjøres numeriske simuleringer for GaAs-solceller med dype urenheter. Slike urenheter fungerer typisk som ødeleggende rekombineringssentre. De kan imidlertid også muliggjøre optisk eksitasjon av ladningsbærere i en to-stegs prosess fra valensbåndet til urenhetsnivået og fra urenhetsnivået til ledningsbåndet, slik at ladningsbærerne bidrar til den fotogenererte strømmen. Dette er kjent som den urenhets-fotovoltaiske (engelsk: impurity photovoltaic, IPV) effekten og åpner opp for å utnytte en større del av den innkommende strålingen, siden også fotoner med energi lavere enn materialets hoved-båndgap kan absorberes.

Programvaren for solcellesimulering kalt SCAPS brukes til simuleringene. I dette masterprosjektet evalueres først programvaren som et verktøy for simulering av IPV-effekten. Den vurderes til å være en egnet programvare for slike simuleringer. SCAPS har en bred funksjonalitet, også når det gjelder IPV-effekten. Resirkulering av fotoner er imidlertid ikke inkludert.

Etter dette brukes SCAPS til å studere påvirkningen en gruppe material- og designparametere har på solcelle-ytelsen. Disse parameterne inkluderer foto-ioniserings-tverrsnittene, tverrsnittene for termisk fangst, urenhetstype, grunn bakgrunnsdoping og lysfanging. Foto-ioniserings-tverrsnittene må varieres over flere størrelsesordener for å ha en betydelig påvirkning på celle-ytelsen. Tverrsnittene for termisk fangst varieres også logaritmisk og har stor påvirkning på celle-ytelsen. En egnet kombinasjon av urenhetstype og tetthet av grunn bakgrunnsdoping har potensiale til å forbedre celle-ytelsen. En høy grad av lysfanging er essensiell for at gevinsten av IPV-effekten skal være større enn den økte rekombineringen assosiert med de dype urenhetene.

Av alle solcellene som er simulert i dette arbeidet (med unntak av én celle hvis kredibilitet svekkes av numeriske problemer) er den høyeste oppnådde konverteringseffektiviteten 33.5 %. Dette oppnås for en celle med maksimal lysfanging og akseptor-type dype urenheter som er delvis kompensert av donor-type grunn bakgrunnsdoping. En lignende celle uten dype urenheter har en effektivitet på 28.2 %. Hvis maksimal lysfanging kan oppnås, indikerer dette et stort potensial for solceller med IPV-effekt. Effektiviteten avtar imidlertid drastisk ved dårligere lysfanging.

Table of Contents

Preface i

Abstract iii

Sammendrag v

1 Introduction 1
- 1.1 Background . . . 1
- 1.2 Objectives . . . 2
- 1.3 Previous Work . . . 2
- 1.4 Structure of the Thesis . . . 3

2 Solar Cell Theory 5
- 2.1 Key Equations . . . 5
- 2.2 pn-Junction . . . 6
  - 2.2.1 Formation . . . 6
  - 2.2.2 Space Charge . . . 7
  - 2.2.3 Electric Field . . . 7
  - 2.2.4 Potential . . . 8
  - 2.2.5 Width of Space Charge Region . . . 8
- 2.3 Energy Band Diagram . . . 9
  - 2.3.1 Thermal Equilibrium . . . 9
  - 2.3.2 Quasi-Fermi Levels . . . 10
- 2.4 Current-Voltage Characteristics of Ideal Diode . . . 12
- 2.5 Quantum Efficiency . . . 14
- 2.6 Loss Mechanisms . . . 14
  - 2.6.1 Recombination . . . 14
  - 2.6.2 Optical Losses . . . 14

3 The Impurity Photovoltaic Effect: Theory and Models 17
- 3.1 Conventional Shockley-Read-Hall Recombination . . . 17
- 3.2 Theory of the IPV Effect . . . 21
- 3.3 The Lucovsky model for the Photo-Ionization Cross Section . . . 23
- 3.4 Terminology . . . 24

4 SCAPS: A Solar Cell Simulation Software **25**
4.1 Introduction to SCAPS . . . 25
4.2 Performing Simple Simulations . . . 26
4.2.1 Action Panel . . . 26
4.2.2 Solar Cell Definition Panel . . . 27
4.2.3 Layer Properties Panel . . . 29
4.2.4 Contacts . . . 29
4.3 Summary of the Simulation Procedure . . . 30
4.4 Introducing Impurities and Defects . . . 31
4.5 Implementation of the IPV effect in SCAPS . . . 32
4.6 Displaying and Saving Results . . . 33
4.7 Scripting . . . 34

5 SCAPS Simulations of GaAs IPV Solar Cells **37**
5.1 General Settings and Parameters . . . 37
5.1.1 Versions of the SCAPS software . . . 37
5.1.2 Settings Used for All Simulations . . . 38
5.1.3 Parameters kept at fixed values . . . 39
5.1.4 Numerical Settings . . . 41
5.1.5 Overview of Cells and Simulations . . . 41
5.2 Parameters of the Impurity Free Cells . . . 42
5.3 Parameters of the Reference Cell . . . 42
5.4 Testing of SCAPS as a Tool for Simulating IPV Solar Cells . . . 43
5.4.1 SRH Recombination in SCAPS . . . 43
5.4.2 Implementation of the Lucovsky Model for Photo-Ionization Cross Section 43
5.5 Varying Design and Impurity Parameters . . . 44
5.5.1 Photo-Ionization Cross Section Parameters . . . 44
5.5.2 Thermal Capture Cross Section . . . 44
5.5.3 Impurity Type and Shallow Background Doping . . . 46
5.5.4 Internal Front Contact Reflection and IPV-Layer Thickness . . . 46

6 Results and Discussion **47**
6.1 Performance of the Impurity Free Cells . . . 47
6.2 Performance of the Reference Cell . . . 50
6.3 Evaluation of SCAPS as a Tool for Simulating IPV Solar Cells . . . 58
6.3.1 SRH Recombination in SCAPS . . . 58
6.3.2 Implementation of the Lucovsky Model for Photo-Ionization Cross Section 60
6.3.3 Evaluation . . . 61
6.4 Influence of Design and Material Parameters on Cell Performance . . . 62
6.4.1 Photo-Ionization Cross Section Parameters . . . 62
6.4.2 Thermal Capture Cross Section . . . 68
6.4.3 Impurity Type and Shallow Background Doping . . . 71
6.4.4 Internal Front Contact Reflection and IPV-Layer Thickness . . . 73

7 Conclusions and Further Work **75**

Bibliography **77**

Appendix A SCAPS Script Example **81**

Appendix B MATLAB Implementation of the Lucovsky Model **83**

Appendix C Personal Communication **87**

C.1 On the Effective Field Ratio in the Lucovsky Model 88
C.2 On the Implemetation of the Lucovsky Model in SCAPS 94
C.3 On the Implemetation of the IPV Effect in SCAPS 97

Chapter 1

Introduction

1.1 Background

The rapidly changing climate is one of the most important problems of our time. Slowing the global warming is a difficult and complex challenge. As many factors make up the issue, the solution too is probably a combination of many smaller improvements. One major challenge is to generate as much as possible of the electricity we use from renewable energy sources. According BP's report "Statistical Review of World Energy: 70th edition" [1], the world's total electricity generation in 2020 was approximately 2.7×10^4 TW h. Of this electricity generation, hydroelectricity accounted for approximately 16 %, other renewable for approximately 12 % and nuclear energy for approximately 10 %. Although fossil fuels account for more than half of the electricity generation, the share of renewable energy is increasing. Developing efficient solar cells can, of course, be a contribution to further increase of the share of renewable energy.

Solar cells convert sunlight directly into electrical energy. A variety of technologies have been suggested. One of these are solar cells utilizing the impurity photovoltaic (IPV) effect, from this point referred to as IPV solar cells. The principle upon which these cells are based is that deep level impurities will allow for a two-step generation of charge carriers, thus utilizing also the photons with energies lower than the main band gap of the solar cell material [2]. The inevitable recombination associated with the impurities is a major challenge for these cells.

As early as in 1960, Wolf discussed the possibilities for a multitransition solar cell [3]. In 1965, Lucovsky presented a model for calculation of the photo-ionization cross section of deep level impurities, a measure of the probability that an impurity absorbs photons with energy lower than the main band gap [4]. Güttler and Queisser argued in 1970 that the degradation of cell performance through non-radiative recombination would be grater than the improvement caused by the IPV effect [5]. In 1994, Keevers and Green presented a model for the IPV effect, based on a modified Shockley-Read-Hall (SRH) recombination model [6]. This model allows the SRH recombination rate to be negative, indicating a net generation of carriers. Conversely, a positive SRH recombination rate indicate a net recombination of carriers. The solar cell simulation software SCAPS [7] was extended to include the IPV effect, as described by Khelifi et. al. in 2008 [8]. In a 2011 publication of SCAPS simulations, Yuan et. al. [9] argue that the potential for IPV solar cells is largely determined by the thermal capture cross sections (a measure of the probability for charge carriers to be captured by an impurity).

It is the purpose of the current work to study the IPV effect in GaAs solar cells. Numer-

ical simulations using the solar cell simulation software SCAPS are performed, both to test SCAPS as a tool for simulation of IPV solar cells and to study the influence of a selection of material and design parameters on the cell performance. This is done with the hope of contributing, ever so slightly, to the understanding of the IPV effect and to aid future work on this topic.

It is important to remember that there are many challenges associated with solar cells, also beyond the task of improving cell performance. Factors like the large requirement for area for the cells to occupy, environmental impact and variation in energy generation, as well as economical and social factors come into play. Still, it seems likely that solar cells, combined with other energy resources and the will to reduce our consumption, will be an important part of the solution to the climate crisis.

1.2 Objectives

The first objective of the work with this thesis is to examine the details of how of the solar cell simulation software SCAPS implements the IPV effect. Doing this will help understand if SCAPS is a suitable tool to simulate IPV solar cells and what the advantages and limitations of the software are. In relation to this objective, it is also part of the current work to establish SCAPS as a tool for future work in the research group for which this thesis is written. Therefore, part of the current work has been to write an introduction on how to use SCAPS.

Another objective is to investigate the influence of a set of design and impurity parameters on IPV solar cell performance. This is done through SCAPS simulations. Such simulations can give useful indications as to which parameters are the most important to control when attempting to make actual IPV solar cells.

In addition, the current work is carried out in order to gain understanding of the IPV effect, through studies of literature on the topic and own simulations. With this understanding as platform, the potential for IPV solar cells will be discussed.

1.3 Previous Work

This master's thesis builds upon my specialization project report, "Numerical Simulation of Single Junction GaAs Solar Cell Performance Using SCAPS" [10]. The objective of that project was to investigate the influence of a set of design and material parameters on solar cell performance. This was done through solar cell simulations with use of the software SCAPS. The cell in question was a single junction GaAs solar cell consisting of a p- and an n-layer in addition to front and back contacts. The initial values for the set of parameters turned out to result in a rather efficient cell, and the efficiency increase achieved by varying parameter values throughout the project was small.

The specialization project provides a good starting point for the work on this master's thesis. This is largely because the current work needs an impurity free cell to compare those containing impurities to. This comparison will shed light on whether the introduction of impurities has a positive or negative effect on the cell performance. Since the initial cell from the specialization project performed well, and due to its simplicity, it will be the basis for the impurity free cell in the current work. The impurity free cell will, however, include an intrinsic layer between the p- and n-layer, giving it a p-i-n structure. For the cells containing impurities, the impurities will be introduced into such a middle layer.

Both the specialization project and the work for the master's thesis revolve around the same topics and use the same simulation software. As such, there will be some similarities between the specialization project report and the master's thesis when it comes to the

presentation of the theory and the simulation software. More specifically, the general solar cell theory in Chapter 2 was written for the specialization project and is included here for completeness. The theory and models of the IPV effect in chapter 3, on the other hand, is written for this master's thesis. Moreover, some sections on how to use SCAPS in Chapter 4 in this thesis are reworked from the corresponding chapter in the specialization project report. The sections in question will be specified at the beginning of Chapter 4.

1.4 Structure of the Thesis

The thesis is divided into 7 chapters. This section describes briefly the content of the chapters following this introductory chapter.

In Chapter 2 general solar cell theory is presented, as a background for further theory in the next chapter.

In Chapter 3 theory of the IPV effect is presented. An overview is also given of the development of IPV modelling and details of individual models both for the IPV effect and for the IPV parameter photo-ionization cross section.

In Chapter 4 the reader is introduced to SCAPS and how to use the simulation software. It is also presented how the IPV effect is implemented in SCAPS.

In Chapter 5 details of all the simulations of this thesis are provided.

In Chapter 6, the results obtained from the simulations of the previous chapter are presented and discussed.

In Chapter 7 conclusions and suggestions for further work are offered.

Chapter 2

Solar Cell Theory

The content of this chapter was written for my specialization project report [10], and is included here for completeness.

The theory in this chapter is, unless otherwise specified, based on Green's *Solar Cells: Operating Principles, Technology and System Applications*, chapters 1-5 [11, pp. 1-102]. The basic properties of light and semiconductors are assumed known to the reader, and the basic equations of semiconductor devices are not derived, but merely stated along with other key equations. From this point, the pn-junction is examined, followed by a presentation of energy band diagrams. Then, the current-voltage characteristics of the ideal diode are explained and quantum efficiency is briefly defined. Finally, different loss mechanisms are presented.

2.1 Key Equations

The basic equations of (one-dimensional) semiconductor devices relevant for this project are:

$$\frac{d\xi}{dx} = \frac{q}{\epsilon}(p - n + N_D - N_A) \tag{2.1}$$

$$J_e = q\mu_e n\xi + qD_e\frac{dn}{dx} \tag{2.2}$$

$$J_h = q\mu_h p\xi - qD_h\frac{dp}{dx} \tag{2.3}$$

$$\frac{1}{q}\frac{dJ_e}{dx} = R - G \tag{2.4}$$

$$\frac{1}{q}\frac{dJ_h}{dx} = -(R - G) \tag{2.5}$$

where the symbols represent the following quantities:
ξ: Electric field in the x-direction
q: Elemental charge
ϵ: Permittivity of the material
p: Concentration of holes in the valence band (VB)

n: Concentration of electrons in the conduction band (CB)
N_D/N_A: Concentration of donor/acceptor type dopant atoms
J_e: Contribution of the electrons in the CB to the current density in the x-direction
J_h: Contribution of holes in the VB to the current density in the x-direction
μ_e/μ_h: Electron/hole mobility
D_e/D_h: Electron/hole diffusion constant
R: Net recombination rate
G: Net generation rate

Other relevant equations include

- The relation between the the space charge density, ρ, and the electric field (equivalent to Equation 2.1):

$$\frac{d\xi}{dx} = \frac{\rho}{\epsilon}. \tag{2.6}$$

- The relation between the potential, ψ, and the electric field:

$$\frac{d\psi}{dx} = -\xi. \tag{2.7}$$

- The relation between effective mass, m^*, and thermal velocity, v_{th}, through Boltzmann's constant, k, and the absolute temperature, T [12, p. 44]:

$$\frac{1}{2}m^* v_{th}^2 = \frac{3}{2}kT. \tag{2.8}$$

- The Einstein relations

$$D_e = \frac{kT}{q}\mu_e, \quad D_h = \frac{kT}{q}\mu_h. \tag{2.9}$$

2.2 pn-Junction

2.2.1 Formation

To describe the pn-junction it is possible to visualize the formation of such a junction as the process of combining a piece of n-type semiconductor and a p-type semiconductor. Although the formation normally takes place in a different way, this approach makes it easier to understand the physics involved. The process is illustrated in Figure 2.1. When the pieces are in contact, electrons from the n-type material and holes from the p-type material start to diffuse into the other side of the pn-junction, due to the newly created concentration gradients. As they recombine, the charge of the ionized dopant atoms are no longer balanced by the charge of the free charge carriers. Since the dopant atoms are localized, the result is a creation of space charge region in the area around the junction, with negative charge on the p-side of the junction and positive charge on the n-side. This region is also called the depletion region, as it is depleted of free charge carriers. An electric field is created due to the different charges. The direction of this field as well as the ionized dopant atoms are shown in Figure 2.1(b). In equilibrium, the drift caused by the electric field and the diffusion caused by the concentration gradient will be equal, and the net charge carrier flow will be zero. If the two sides have a different concentration of dopant atoms, the space charge region will extend further into the more lightly doped side. This is because the same number of holes and electrons have recombined, leaving behind the same number of

unbalanced ionized dopant atoms. Lower dopant atom concentration means these dopant atoms are spread out over a greater distance.

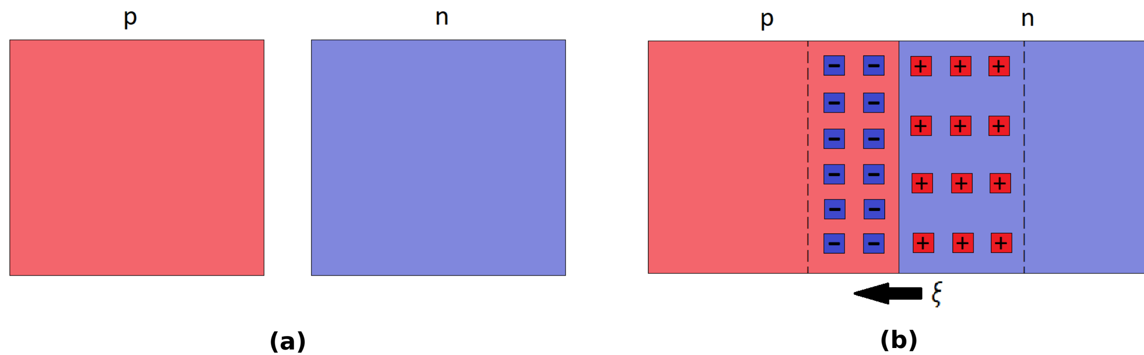

Figure 2.1: Formation of a pn-junction by combining a piece of p-type and a piece of n-type semiconductor. **(a)** The isolated pieces and **(b)** the the pieces combined to form a pn-junction. When the pieces are in contact, electrons and holes recombine, leaving behind unbalanced dopant atoms, which creates an electric field, ξ.

2.2.2 Space Charge

The space charge, ρ, in the pn-junction is illustrated in Figure 2.2(a) as a function of distance, x. The junction between p- and n-type material is placed at $x = 0$, and w_p and w_n are the distances the space charge region extends into the, p- and n-side, respectively. The space charge on the p-side, that is, for $-w_p < x < 0$, is $\rho = -qN_A$. On the n-side, that is, for $0 < x < w_n$, the space charge is $\rho = qN_D$.

2.2.3 Electric Field

Making use of Equation 2.6, the electric field strength throughout the junction can be found. On the p-side, the following expression is obtained:

$$\frac{d\xi}{dx} = \frac{-qN_A}{\epsilon}.$$

Integration yields

$$\xi = \frac{-qN_A}{\epsilon}x + \xi_{0p},$$

where the constant ξ_{0p} can be found by using the boundary condition $x = -w_p \Rightarrow \xi = 0$. The result is

$$\xi = \frac{-qN_A}{\epsilon}(x + w_p). \tag{2.10}$$

Use of the same approach for the n-side yields

$$\xi = \frac{qN_D}{\epsilon}(x - w_n). \tag{2.11}$$

The plot of these expressions within the appropriate ranges is illustrated in Figure 2.2(b).

2.2.4 Potential

To find the potential distribution and potential difference across the junction, and subsequently the width of the space charge region, W, Equation 2.7 is used. The derivation of the potential distribution, potential difference and W is aided by Ref. [2, pp. 134-136]. On the p-side, with the expression for the electric field given in Equation 2.10, Equation 2.7 takes the form

$$\frac{d\psi_p}{dx} = \frac{qN_A}{\epsilon}(x + w_p).$$

Integration yields

$$\psi_p(x) = \frac{qN_A}{\epsilon}\left(\frac{x^2}{2} + w_p x\right) + \psi_{0p}, \tag{2.12}$$

where ψ_{0p} is a constant.

Similarly for the n-side, with the electric field given in Equation 2.11

$$\psi_n(x) = -\frac{qN_D}{\epsilon}\left(\frac{x^2}{2} - w_n x\right) + \psi_{0n}, \tag{2.13}$$

where ψ_{0n} is an constant.

In order for the distribution to be continuous, $\psi_p(0)$ must equal $\psi_n(0)$. This means that $\psi_{0p} = \psi_{0n} = \psi_0$. The potential difference is the built in potential, V_{bi}, with any applied voltage, V_a, subtracted. The value of the potential difference is simply $\psi_n(w_n) - \psi_p(-w_p)$. Hence,

$$V_{bi} - V_a = \psi_n(w_n) - \psi_p(-w_p) = \frac{qN_D}{\epsilon}\frac{w_n^2}{2} + \frac{qN_A}{\epsilon}\frac{w_p^2}{2} + \psi_0 - \psi_0.$$

Simplifying yields

$$V_{bi} - V_a = \frac{q}{2\epsilon}\left(w_n^2 N_D + w_p^2 N_A\right). \tag{2.14}$$

The potential distribution and the potential difference are both illustrated in Figure 2.2(c). Since only the potential difference is of interest, and since this according to Equation 2.14 is independent of the constant ψ_0, this constant is in the figure chosen so that $\psi_p(-w_p) = 0$.

2.2.5 Width of Space Charge Region

Equation 2.14 can be used to find W, which is simply the sum of w_p and w_n. Multiplying both sides of Equation 2.14 with $\left(\frac{1}{N_A} + \frac{1}{N_D}\right)$ and rearranging gives

$$\frac{w_n^2 N_D + w_p^2 N_A}{N_A} + \frac{w_n^2 N_D + w_p^2 N_A}{N_D} = \frac{2\epsilon}{q}(V_{bi} - V_a)\left(\frac{1}{N_A} + \frac{1}{N_D}\right).$$

Since the total space charge is equal in both sides of the junction, $w_p N_A = w_n N_D$. Making use of this, the previous expression becomes

$$w_p^2 + w_n^2 + 2w_p w_n = \frac{2\epsilon}{q}(V_{bi} - V_a)\left(\frac{1}{N_A} + \frac{1}{N_D}\right),$$

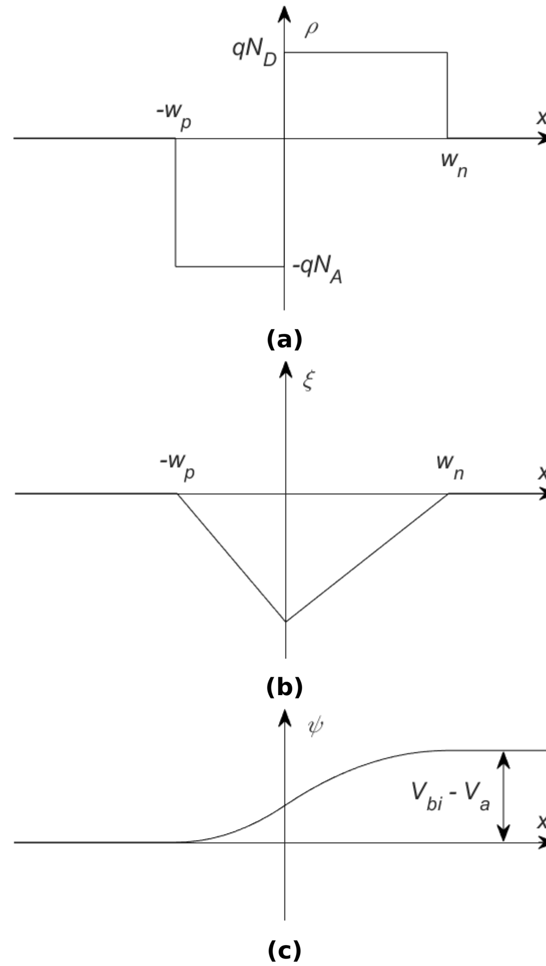

Figure 2.2: (a) Space charge, **(b)** electric field and **(c)** potential distribution across the pn-junction. The figure is based on a similar figure in Ref. [11, p. 67].

which by further rearranging results in the expression for W:

$$W = w_p + w_n = \sqrt{\frac{2\epsilon}{q}(V_{bi} - V_a)\left(\frac{1}{N_A} + \frac{1}{N_D}\right)}. \tag{2.15}$$

2.3 Energy Band Diagram

2.3.1 Thermal Equilibrium

Figure 2.3(a) illustrates energy band diagrams for isolated pieces of p- and n-type semiconductor. Included are the edges of the conduction band and valence band, E_C and E_V, respectively, and the Fermi level, E_F, of the two pieces. The energy differences between E_F and the band edges are related to the charge carrier concentrations in the bands. The concentration of holes in the valence band, p is

$$p = N_V e^{(E_V - E_F)/kT}, \tag{2.16}$$

where, N_V is the effective density of states in the valence band, k is the Boltzmann constant and T is the absolute temperature.

The concentration of electrons in the conduction band, n, is

$$n = N_C e^{(E_F - E_C)/kT}, \tag{2.17}$$

where N_C is the effective density of states in the conduction band.

Figure 2.3(b) illustrates what happens when the pieces are combined to form a pn-junction. In thermal equilibrium, the Fermi levels of the isolated pieces must align to form one single Fermi level throughout the junction. This means there will be a change in energy of the band edges across the junction. This energy change, or band bending, corresponds to the built in potential as qV_{bi}.

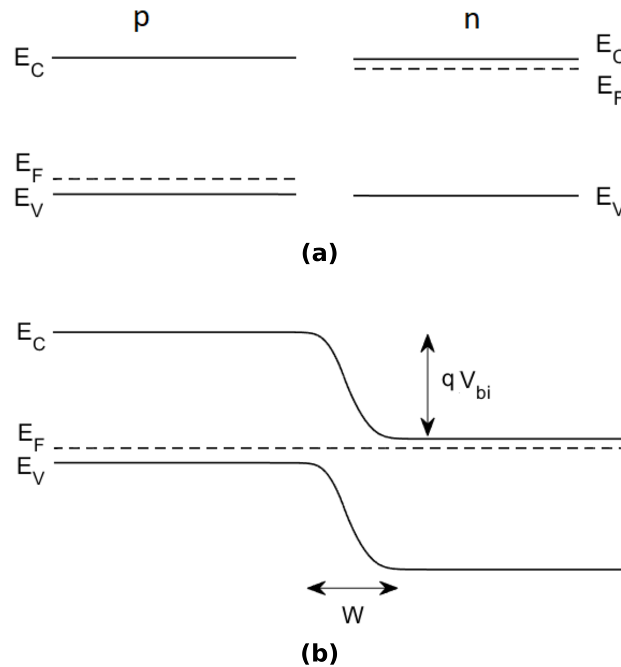

Figure 2.3: (a) Energy bands of isolated pieces of p- and n-doped semiconductor. **(b)** Energy band diagram for the pn-junction in thermal equilibrium. Also shown is the width of the space charge region, W. The figures are based on similar figures in Ref. [11, pp. 64-65]. The figures are made with the aid of the SCAPS software.

2.3.2 Quasi-Fermi Levels

This subsection is based on Ref. [2, pp. 57-59] and Ref. [13, pp. 154-171].

When the pn-junction is under illumination, it is no longer in thermal equilibrium. In this case, the Fermi level and the corresponding Fermi distribution are not able to describe the occupation of states in both the conduction band and the valence band. This is because the number of charge carriers increase from their equilibrium values under illumination, and a Fermi distribution would have to be shifted toward higher energies to properly describe the occupation of states in the conduction band, and toward lower energies to describe the occupation in the valence band. To be able to describe the occupation in both bands at the same time, the concepts of quasi-Fermi distributions and quasi-Fermi levels are introduced. One quasi-Fermi distribution describes the occupation in the conduction band, another in the valence band. The corresponding quasi-Fermi levels are referred to as $E_{F,n}$ for the occupation in the conduction band and $E_{F,p}$ for the occupation in the valence band.

Equations 2.16 and 2.17 can now be modified to include $E_{F,p}$ and $E_{F,n}$ instead of E_F:

$$p = N_V e^{(E_V - E_{F,p})/kT} \tag{2.18}$$

$$n = N_C e^{(E_{F,n} - E_C)/kT} \tag{2.19}$$

Equations 2.18 and 2.19 show the relation between the charge carrier densities and the difference between the quasi-Fermi levels and the band edges. The closer to the band edge the quasi-Fermi level is, the higher is the charge carrier concentration in that band. The increase in the number of charge carriers when the cell is illuminated can thus be seen in the change of the energy difference between the quasi-Fermi levels and the respective band edges. Both types of charge carriers will increase by the same amount under illumination, since each electron exited to the conduction band leaves behind a hole in the valence band. However, the relative increase is greater for the minority carrier. Thus, owing to the form of Equations 2.18 and 2.19, the quasi-Fermi level of the minority carrier deviates more from the equilibrium value E_F than the majority carrier quasi-Fermi level does. That means the deviation of $E_{F,n}$ from E_F on the n-side is small compared to the one of $E_{F,p}$, and the other way around for the p-side. The quasi-Fermi levels may vary as a function of position in the junction (as is the case for a pn-junction without any applied voltage), and are commonly displayed in energy band diagrams. This is illustrated in Figure 2.4(b).

Applying an external voltage, V_a, also brings the cell out of thermal equilibrium. The band bending is in this case given as $q(V_{bi} - V_a)$. This is illustrated in Figure 2.4(c), in which the cell is not illuminated. The effect of both illumination and an applied voltage is illustrated in Figure 2.4(d).

From looking at the figures, a relation between the applied voltage and the energy difference between the quasi-Fermi levels becomes evident. Assuming the quasi-Fermi levels of the majority carriers ($E_{F,p}$ on the p-side and $E_{F,n}$ on the n-side) have the same energy relative to the band edges as E_F, then their energy difference is $E_{F,n} - E_{F,p} = qV_a$. This is clearest in the case of the cell in the dark, but also visible for the illuminated cell, by comparing $E_{F,n}$ on the n-side and $E_{F,p}$ on the p-side.

The spatial variation of the quasi-Fermi levels also provide information on the net current density in the cell. The electron current density given in Equation 2.2 can now be expressed as a function of the appropriate quasi-Fermi level. The differential of the electron concentration can, by using Equation 2.19, be written as

$$\frac{dn}{dx} = \frac{d}{dx}\left[N_C e^{(E_{F,n}-E_C)/kT}\right] = \frac{N_C}{kT} e^{(E_{F,n}-E_C)/kT} \frac{d}{dx}\left[E_{F,n} - E_C\right] = \frac{n}{kT}\left[\frac{dE_{F,n}}{dx} - \frac{dE_C}{dx}\right].$$

Using this result and Equation 2.9, the net electron current density can be written as

$$J_e = q\mu_e n\xi + qD_e \frac{dn}{dx} = q\mu_e n\xi + \mu_e n\left[\frac{dE_{F,n}}{dx} - \frac{dE_C}{dx}\right] = q\mu_e n\xi - \mu_e n\frac{dE_C}{dx} + \mu_e n\frac{dE_{F,n}}{dx}.$$

The term $\mu_e n \frac{dE_C}{dx}$ can be expressed in terms of the potential change across the pn-junction. As already mentioned, the bending of the energy bands relates proportionally to the potential difference and the elemental charge. Since an increasing potential across the junction leads to a decreasing of the energy of the band edges, the relation can be written as $\frac{dE_C}{dx} = -q\frac{d\psi}{dx}$. From Equation 2.7, $\frac{d\psi}{dx} = -\xi$, and thus is $\frac{dE_C}{dx} = q\xi$. The expression for the

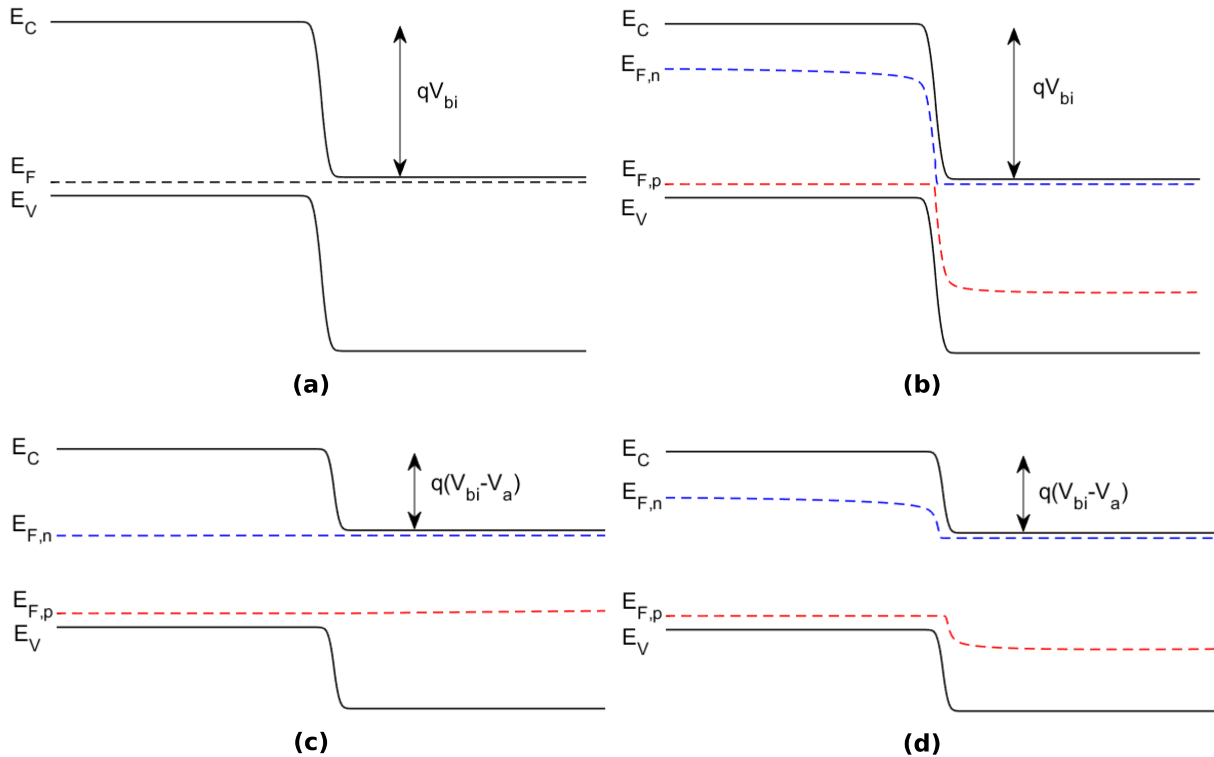

Figure 2.4: The effects of illumination and applied voltage on the energy bands of a pn-junction. Energy band diagrams of a pn-junction **(a)** in thermal equilibrium (equivalent to Figure 2.3(b), included here for comparison), **(b)** under illumination with no applied voltage, **(c)** in the dark with an applied voltage $V_a > 0$ and **(d)** under illumination with an applied voltage $V_a > 0$. The figures are made with the aid of the SCAPS software.

electron current density can now be simplified:

$$J_e = \mu_e n \frac{dE_{F,n}}{dx}. \tag{2.20}$$

Similarly for the hole current:

$$J_h = \mu_h p \frac{dE_{F,p}}{dx}. \tag{2.21}$$

This means that the net current density of either charge carrier can be interpreted by looking at the spatial variation of the appropriate quasi-Fermi level. For example, completely flat quasi-Fermi levels, indicate that the net current density is zero.

2.4 Current-Voltage Characteristics of Ideal Diode

The performance of a solar cell is commonly presented as current-voltage characteristics, that is, the relationship between the voltage applied to the cell and the current flowing through it. More specifically, this relationship is expressed by plotting the current as a function of the voltage in an IV curve. From this point on, the applied voltage previously referred to as V_a, is now referred to as just V. The current is referred to as I, and is useful in order to describe the IV characteristics. However, in later chapters, the current density, J, is of greater interest. The current density and the current relates through the cross-sectional area through which the current is flowing, A, as $J = I/A$. The current density is therefore a

useful quantity for the cells in this project, as they have undefined cross-sectional areas.

To derive IV characteristics, a series of approximations are commonly made. The depletion region is assumed to be completely depleted of free charge carriers, and the quasi-neutral regions surrounding it are assumed to in fact have a net space charge of zero. Furthermore, it is assumed that the drift and diffusion currents in the depletion region are approximately of equal magnitude. A third approximation is that the majority carrier concentration is much greater than the minority carrier concentration. Additionally, minority carriers in quasi-neutral regions are assumed to flow mainly through diffusion. Finally, the charge carrier currents are assumed to be constant over the depletion region. The resulting relationship between the current and voltage for an ideal diode (corresponding to a solar cell in the dark) is given as

$$I = I_0 \left(e^{qV/kT} - 1 \right), \tag{2.22}$$

where I_0 is a constant dependent on material parameters and the cross-sectional area of the diode.

Under illumination, the relationship is similar, but the total current is now shifted according to the light-generated current, I_L, as

$$I = I_0 \left(e^{qV/kT} - 1 \right) - I_L. \tag{2.23}$$

Illustrations of the curves of Equation 2.22 and 2.23 is shown in Figure 2.5(a). A common way to present IV curves is to define the current in the opposite direction, that is, to invert the curve around the x-axis. The IV curve can then be presented in the first quadrant. This is done in Figure 2.5(b), along with some solar cell performance parameters. The short-circuit current, I_{SC}, is the current when the cell circuit is short-circuited, that is, when the applied voltage is zero. This value is ideally equal to I_L. The open-circuit voltage, V_{OC}, is the voltage of an open cell circuit, that is, when the current is zero. As the power is simply the product of the current and the voltage, the power must be zero at both I_{SC} and V_{OC}, and the maximum power point is found along the curve between these points. The voltage and current at the maximum power point are referred to as V_M and I_M, respectively.

The fill factor, FF, is the ratio of the maximum power to the power that would be obtained if it were possible to achieve the current value I_{SC} at the same time as the voltage value V_{OC}. In more mathematical terms

$$FF = \frac{V_M I_M}{V_{OC} I_{SC}}. \tag{2.24}$$

The efficiency of the cell, η, is simply the power extracted from the cell, $P_{out} = V_M I_M$, divided by the power of the incident light, P_{in}. With the help of Equation 2.24, η can then be written as

$$\eta = \frac{V_{OC} I_{SC} FF}{P_{in}}. \tag{2.25}$$

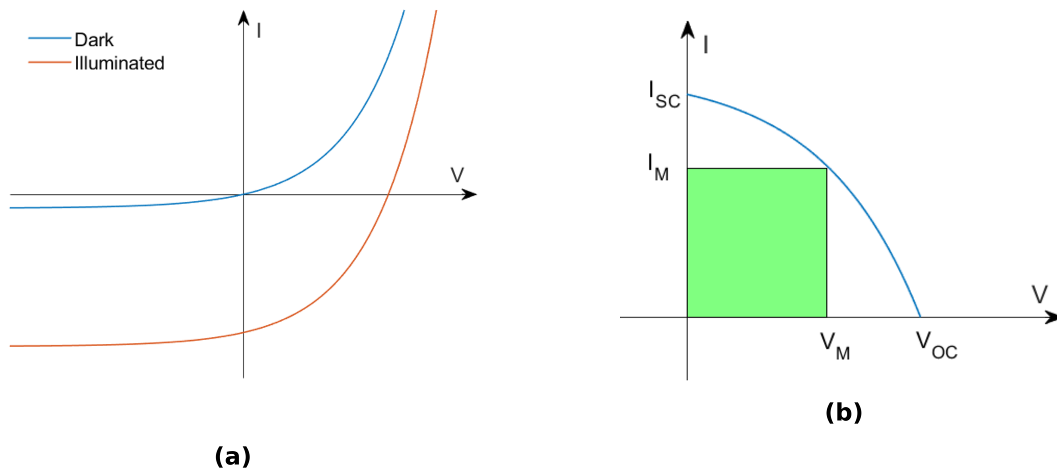

Figure 2.5: (a) IV curves of a diode in the dark and an illuminated diode. The curve of the illuminated diode is shifted downward by the value I_L. **(b)** The curve of the illuminated diode inverted around the x-axis. Indicated are the performance parameters I_{SC}, V_{OC}, I_M and V_M. The area of the green rectangle equals the maximum power the cell can deliver. Note that the figures are mere illustrations and may not accurately represent actual diodes. The figures are based on a similar figure in Ref. [11, p. 79].

2.5 Quantum Efficiency

The quantum efficiency is the ratio of the number of electrons contributing to the light generated current to the number of photons of a given wavelength incident on the cells surface. In other word, it is the probability of a photon of a given wavelength generating an electron that contributes to the current of the cell. The quantum efficiency is a function of wavelength and thus independent of the spectrum of the incident radiation. [14, pp. 7-8]

2.6 Loss Mechanisms

2.6.1 Recombination

Recombination is the process in which electrons and a holes annihilate, giving off photons and/or phonons [2, p. 71]. Radiative recombination, Auger recombination, recombination through traps and recombination at surfaces are among the mechanisms through which recombination can occur.

Radiative recombination occurs when an electron occupying a higher energy state goes into a lower energy state, giving off light. For Auger recombination, the energy from an electron going into a lower energy level is given to another electron, causing this electron to go into a state of higher energy. Recombination through traps involves an electron in the conduction band recombining with a hole in the valence band in two steps, through a defect level in the band gap. Recombination at surfaces occurs much in the same way. The boundary of a surface affects the bonds in the material, causing many defect levels at surfaces. These enable recombination through traps at surfaces.

2.6.2 Optical Losses

Examples of losses of an optical nature are shading from the front contact, reflection of the incident light at the front surface of the solar cell and photons (of appropriate wavelengths)

failing to be absorbed.

The necessity of a front contact gives rise to shading losses. It can be reduced by decreasing the area of the front contact, but this increases the path the charge carriers have to travel in the semiconductor in order to reach the contact, thus reducing the probability of collection of the charge carriers. Therefore, the front contact should be designed in a way that takes both factors into account. Reflection at the solar cell surface is often reduced by applying a layer of an anti-reflection coating.

Finally, photons of different wavelengths have different probabilities of being absorbed a certain distance into the material, owing to their different values of absorption coefficient. This means that some photons requires a thicker cell to get absorbed, otherwise they will be transmitted through the cell. The decay of the light intensity, β, is described by the simple Beer-Lambert law:

$$\beta(x) = \beta_0 e^{-\alpha x}, \tag{2.26}$$

where $\beta_0 = \beta(0)$, x is the distance the light has traveled into the material and α is the absorption coefficient for the wavelength in question (assumed to be uniform throughout the material) [14, p. 88].

The obvious way to make sure all the photons are absorbed is simply to make the cell thick enough. However, having to travel a greater distance again reduces the probability the charge carriers have of reaching the contacts before recombining. As such, the cell design should aim for a compromise.

Chapter 3

The Impurity Photovoltaic Effect: Theory and Models

This chapter presents theory and a selection of models for the impurity photovoltaic (IPV) effect. First, the conventional Shockley-Read-Hall (SRH) recombination rate is derived. The motivation for this derivation is to aid the understanding of the mechanisms also relevant for the IPV effect. Second, the theory behind the IPV effect is presented. Third, a model for the photo-ionization cross section found literature is presented. Finally, a summary of the terminology regarding the IPV effect and recombination is included. There are many terms and symbols to keep track of, and meaning assigned to some of the terms and symbols in this thesis might be somewhat unfamiliar. The summary is thus included to avoid confusion.

3.1 Conventional Shockley-Read-Hall Recombination

The recombination mechanism and recombination rate in this section was presented by Shockley and Read [15] and by Hall [16][1] in the early 1950's. The theory and derivation in this section is to some extent based on these original publications, but follow more closely Sze and Lee's textbook *Semiconductor Devices: Physics and Technology* [12] and Würfel and Würfel's textbook *Physics of Solar Cells: From Basic Principles to Advanced Concepts* [2].

SRH recombination is the recombination of electrons and holes via an energy level in the otherwise forbidden band gap. This is the recombination mechanism that in section 2.6 of Chapter 2 was referred to as recombination through traps. The energy level can be caused by a crystal defect or an impurity, but will here be referred to as an impurity. Its energy level with respect to the valence band edge is denoted E_{imp}.

The impurity can capture electrons from the conduction band, given that there are impurity states which are unoccupied by electrons. Similarly, the impurity can capture holes from the valence band, given that there are impurity states which are occupied by electrons. Electrons and holes can also be emitted from the impurity to their respective bands.

It is important to note that in the conventional SRH model, the emission of charge carriers from the impurity to either band is a thermal process, and not a result of incoming

[1] In ref. [16] the expression for the SRH recombination rate is presented, but not derived. Ref. [16] does, however, reference another publication by the same author from the preceding year: R. N. Hall, *Phys. Rev.*, vol. 83, p. 228, 1951. This publication might be a more precise reference to Hall's contribution to description of the SRH recombination. Unfortunately, I have not been able to find the full-text version of this publication, and I am therefore reluctant to include it in my reference list. For the purpose of this thesis the publication is not necessary, as ref. [15] include a derivation of the same recombination rate.

photons. On the other hand, the energy given up upon capture of the charge carries can be either thermal or radiative; the conventional SRH model is not concerned with the nature of the capture processes. The four relevant processes are illustrated in Figure 3.1.

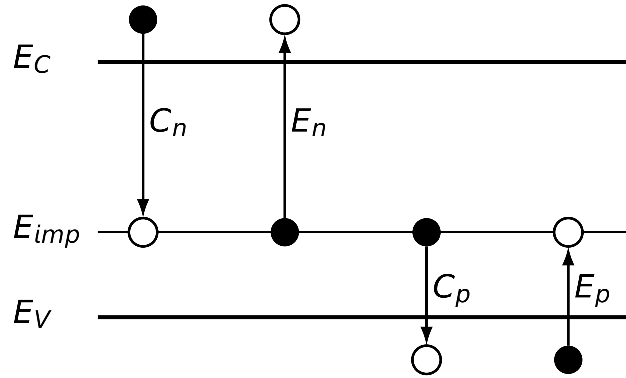

Figure 3.1: Energy band diagram illustrating the four transitions included in the conventional SRH model. Based on similar figures in refs. [12] and [15]. E_C and E_V are the conduction band edge and the valence band edge, respectively. E_{imp} is the energy level of the impurity. Filled circles represent electrons, empty circles represent holes. The depicted situation is the one before the transitions take place and the arrows indicate the direction of the electron transitions. The rates represent the following:
C_n: Capture rate of electrons. E_n: Emission rate of electrons.
C_p: Capture rate of holes. E_p: Emission rate of holes.

The capture rate of electrons can be expected to be proportional to the number of electrons in the conduction band, n, and the number of unoccupied impurity states, $N_{imp}\left(1-f_{imp}\right)$. Here, N_{imp} is the number of impurity states per unit volume and f_{imp} is the probability of a impurity state to be occupied by an electron. f_{imp} is in thermal equilibrium given by the Fermi distribution:

$$f_{imp} = \frac{1}{1+e^{(E_{imp}-E_F)/kT}}, \tag{3.1}$$

where E_F is the Fermi energy, k is the Boltzmann constant and T is the absolute temperature. The probability of an impurity level being unoccupied by an electron can be written as

$$1-f_{imp} = \frac{1+e^{(E_{imp}-E_F)/kT}-1}{1+e^{(E_{imp}-E_F)/kT}} = f_{imp}e^{(E_{imp}-E_F)/kT}. \tag{3.2}$$

The capture rate of electrons can thus be expressed as

$$C_n = v_n^{th}\sigma_n^{th}nN_{imp}\left(1-f_{imp}\right), \tag{3.3}$$

where $v_n^{th}\sigma_n^{th}$ is taken as the proportionality constant. v_n^{th} is the thermal velocity of the electrons, and σ_n^{th} is the electron thermal capture cross section. Given that the impurity is unoccupied, an electron will be captured by an impurity if it passes through the impurity's thermal capture cross section [2, p. 77]. $v_n^{th}\sigma_n^{th}$ (with the unit cm^3s^{-1}) can also be thought of as the volume an electron sweeps through per unit time. The electron will be captured by the impurity if the impurity is located inside this volume [12, p. 553].

The rate of electron emission should by the same logic be proportional to the number of

occupied impurity states:

$$E_n = e_n N_{imp} f_{imp}, \tag{3.4}$$

where e_n is an emission constant yet to be determined. In thermal equilibrium, the rate of electron capture and electron emission must be equal. This fact, along with equations (3.1) and (3.2), can be used to express the emission constant:

$$e_n = \frac{v_n^{th} \sigma_n^{th} n N_{imp} \left(1 - f_{imp}\right)}{N_{imp} f_{imp}} = v_n^{th} \sigma_n^{th} n e^{(E_{imp} - E_F)/kT}. \tag{3.5}$$

In equation (2.17) in Chapter 2 the equilibrium electron concentration in the conduction band was expressed in terms of the effective density of states in the conduction band, N_C, and the conduction band edge, E_C, as $n = N_C e^{(E_F - E_C)/kT}$. This relation is valid when the Fermi energy is several kT below E_C. For the case of an intrinsic semiconductor, this becomes $n_i = N_C e^{(E_i - E_C)/kT}$, where n_i and E_i are the intrinsic carrier concentration and the intrinsic Fermi level, respectively. By using the latter expression, the former can be rewritten as

$$n = n_i e^{(E_F - E_i)/kT}. \tag{3.6}$$

In the same way, an expression for the concentration of holes in the valence band, p, can be found using equation (2.16) in Chapter 2:

$$p = n_i e^{(E_i - E_F)/kT}. \tag{3.7}$$

Using equations (3.5) and (3.6), the electron emission constant can be rewritten as

$$\begin{aligned} e_n &= v_n^{th} \sigma_n^{th} n_i e^{(E_F - E_i)/kT} e^{(E_{imp} - E_F)/kT} \\ &= v_n^{th} \sigma_n^{th} n_i e^{(E_{imp} - E_i)/kT}. \end{aligned} \tag{3.8}$$

The hole capture and emission rates are found in the same manner as those for electrons. The hole capture rate can be expressed as

$$C_p = v_p^{th} \sigma_p^{th} p N_{imp} f_{imp}, \tag{3.9}$$

where σ_p^{th} is the hole thermal capture cross section and v_p^{th} is the thermal velocity of holes. The hole emission rate can be expressed as

$$E_p = e_p N_{imp} \left(1 - f_{imp}\right), \tag{3.10}$$

where the emission constant e_p is found using equations (3.1) and (3.2) and the fact that hole capture and emission must be equal in thermal equilibrium:

$$e_p = \frac{v_p^{th} \sigma_p^{th} p N_{imp} f_{imp}}{N_{imp} \left(1 - f_{imp}\right)} = v_p^{th} \sigma_p^{th} p e^{(E_F - E_{imp})/kT}. \tag{3.11}$$

Using equations (3.11) and (3.7), the hole emission constant can be rewritten as

$$
\begin{aligned}
e_p &= v_p^{th}\sigma_p^{th} n_i e^{(E_i - E_F)/kT} e^{(E_F - E_{imp})/kT} \\
&= v_p^{th}\sigma_p^{th} n_i e^{(E_i - E_{imp})/kT}.
\end{aligned} \tag{3.12}
$$

The next step is to find a steady-state expression for f_{imp}. In steady-state, there can be no build-up of either charge carrier at the impurity level. Therefore, the rate of electrons entering the impurity (the electron capture rate plus the hole emission rate) must equal the rate of electrons leaving the impurity (the electron emission rate plus the hole capture rate):

$$
C_n + E_p = E_n + C_p \Leftrightarrow C_n - E_n = C_p - E_p. \tag{3.13}
$$

Inserting equations (3.3), (3.4), (3.9) and (3.10) into equation (3.13) gives

$$
v_n^{th}\sigma_n^{th} n N_{imp}\left(1 - f_{imp}\right) - e_n N_{imp} f_{imp} = v_p^{th}\sigma_p^{th} p N_{imp} f_{imp} - e_p N_{imp}\left(1 - f_{imp}\right). \tag{3.14}
$$

From equation (3.14) expressions for f_{imp} and $1 - f_{imp}$ are found:

$$
f_{imp} = \frac{v_n^{th}\sigma_n^{th} n + e_p}{v_n^{th}\sigma_n^{th} n + v_p^{th}\sigma_p^{th} p + e_n + e_p} \tag{3.15}
$$

and

$$
1 - f_{imp} = \frac{v_p^{th}\sigma_p^{th} p + e_n}{v_n^{th}\sigma_n^{th} n + v_p^{th}\sigma_p^{th} p + e_n + e_p}. \tag{3.16}
$$

One electron-hole pair recombines when an electron has moved from the conduction band to the impurity level and a hole has moved from the valence band to the impurity level (or in other words, when an electron has moved from the conduction band to the valence band via the impurity level). The net recombination rate must thus equal both the net rate of electrons moving from the conduction band to the impurity level and the net rate of holes moving from the valence band to the impurity level (or in other words, the net rate of electrons moving from the impurity level to the valence band). The net recombination rate via impurities, or the SRH recombination rate, is therefore

$$
U_{SRH} = C_n - E_n = C_p - E_p. \tag{3.17}
$$

An expression for U_{SRH} can now be found by replacing for example $C_n - E_n$ with the expressions in equations (3.3) and (3.4) and using the steady-state expressions for f_{imp} and $1 - f_{imp}$ in equations (3.15) and (3.16):

$$
\begin{aligned}
U_{SRH} &= C_n - E_n \\
&= v_n^{th}\sigma_n^{th} n N_{imp}\left(1 - f_{imp}\right) - e_n N_{imp} f_{imp} \\
&= v_n^{th}\sigma_n^{th} n N_{imp} \frac{v_p^{th}\sigma_p^{th} p + e_n}{v_n^{th}\sigma_n^{th} n + v_p^{th}\sigma_p^{th} p + e_n + e_p} - e_n N_{imp} \frac{v_n^{th}\sigma_n^{th} n + e_p}{v_n^{th}\sigma_n^{th} n + v_p^{th}\sigma_p^{th} p + e_n + e_p} \\
&= \frac{N_{imp}\left(v_n^{th}\sigma_n^{th} n v_p^{th}\sigma_p^{th} p - e_n e_p\right)}{v_n^{th}\sigma_n^{th} n + v_p^{th}\sigma_p^{th} p + e_n + e_p}. \qquad (3.18)
\end{aligned}
$$

The final step is to insert the expressions for e_n and e_p from equations (3.8) and (3.12). As e_n and e_p are derived with the assumption of thermal equilibrium, using them in a steady-state expression requires justification. As I understand it, the following quote from Würfel and Würfel's textbook *Physics of Solar Cells: From Basic Principles to Advanced Concepts* offers such a justification:

> *The thermal capture cross sections and the coefficients of emission are likely to depend on the energy distribution of free charge carriers. Owing to the rapid thermalization, however, electrons and holes have the same energy and velocity distributions under illumination as in the dark. Thermal capture cross sections and emission coefficients are therefore expected to have the same values both in the dark and under illumination* [2, p. 78].

This should serve to justify also the use of the same thermal capture cross sections for both thermal equilibrium and steady-state.

By inserting equations (3.8) and (3.12) into equation (3.18) the following expression for the SRH recombination rate is obtained:

$$
\begin{aligned}
U_{SRH} &= \frac{N_{imp}\left(v_n^{th}\sigma_n^{th} n v_p^{th}\sigma_p^{th} p - v_n^{th}\sigma_n^{th} v_p^{th}\sigma_p^{th} n_i e^{(E_{imp}-E_i)/kT} n_i e^{(E_i-E_{imp})/kT}\right)}{v_n^{th}\sigma_n^{th} n + v_p^{th}\sigma_p^{th} p + v_n^{th}\sigma_n^{th} n_i e^{(E_{imp}-E_i)/kT} + v_p^{th}\sigma_p^{th} n_i e^{(E_i-E_{imp})/kT}} \\
&= \frac{N_{imp} v_n^{th}\sigma_n^{th} v_p^{th}\sigma_p^{th}\left(np - n_i^2\right)}{v_n^{th}\sigma_n^{th}\left(n + n_i e^{(E_{imp}-E_i)/kT}\right) + v_p^{th}\sigma_p^{th}\left(p + n_i e^{(E_i-E_{imp})/kT}\right)}. \qquad (3.19)
\end{aligned}
$$

3.2 Theory of the IPV Effect

The theory in this section is based on the description of the IPV effect in Würfel and Würfel's textbook *Physics of Solar Cells: From Basic Principles to Advanced Concepts* [2] and in the work of Keevers and Green [6].

The impurity photovoltaic (IPV) effect is the optical generation of charge carriers via an impurity level in the band gap of a semiconductor. The impurity level enable electrons to be excited from the valence band to the conduction band in a two-step process. This allows for absorption of photons with too low energies to excite electrons directly from the valence band to the conduction band. As a consequence, the a wider range of the incident spectrum of radiation is utilized.

One can imagine twelve different transitions taking place in a semiconductor with a single impurity level in the band gap (disregarding Auger processes). In addition to band-to-

band generation and recombination, electrons in the conduction band can be captured by, and emitted from, the impurity level. Similarly, holes in the valence band can be captured by, or emitted from, the impurity level. The hole capture and emission processes can be visualized as electrons going from the impurity level to the valence band and from the valence band to the impurity level, respectively. In the case that all the six mentioned transitions can occur either thermally or optically/radiatively, we end up with a total of twelve transitions. These are shown in Figure 3.2.

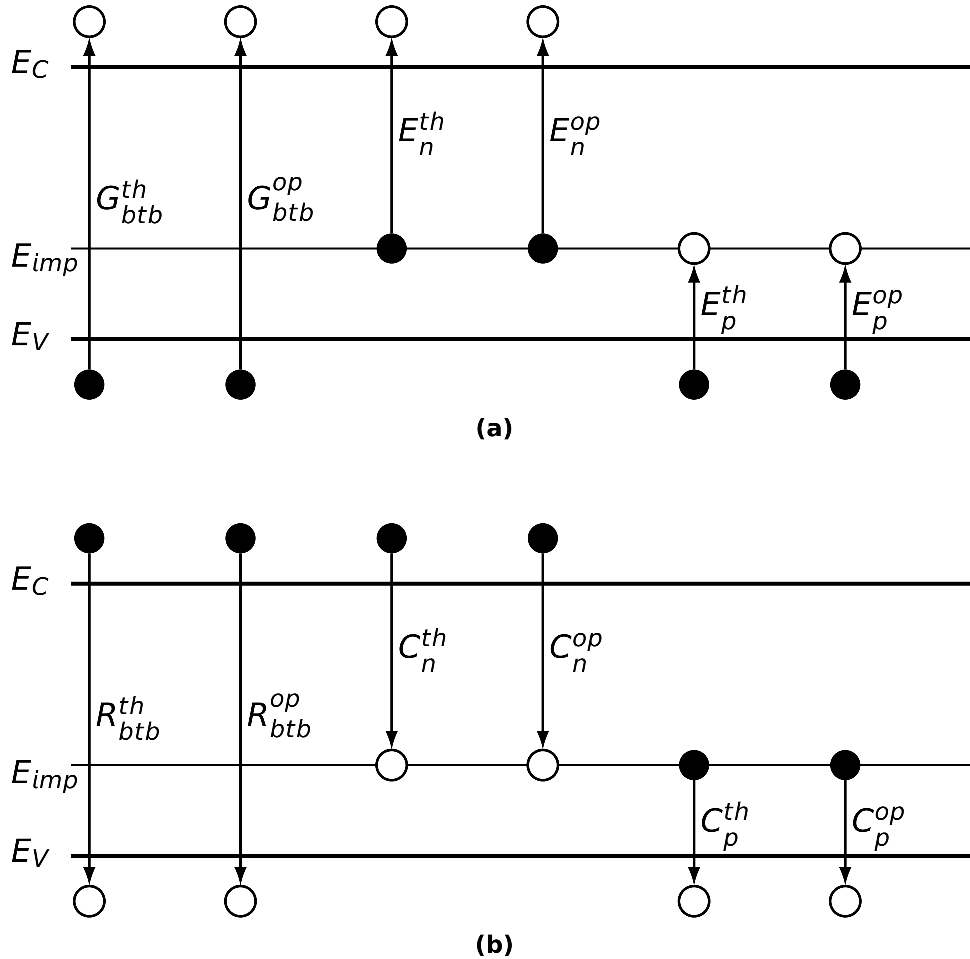

Figure 3.2: Theoretically possible transitions between valence band, conduction band and impurity level. Filled circles represent electrons, empty circles represent holes. The depicted situation is the one before the transitions take place and the arrows indicate the direction of the electron transitions. The rates represent the following:

(a) Generation and emission processes:

G_{btb}^{th}: Thermal band-to-band generation. G_{btb}^{op}: Optical band-to-band generation.

E_e^{th}: Thermal emission of electrons. E_e^{op}: Optical emission of electrons.

E_h^{th}: Thermal emission of holes. E_h^{op}: Optical emission of holes.

(b) Recombination and capture processes:

R_{btb}^{th}: Thermal band-to-band recombination. R_{btb}^{op}: Optical band-to-band recombination.

C_e^{th}: Thermal capture of electrons. C_e^{op}: Optical capture of electrons.

C_h^{th}: Thermal capture of holes. C_h^{op}: Optical capture of holes.

The models describing the IPV effect differ in which of these transitions are included. In the model of Keevers and Green [6], only six impurity-related transitions are included, not eight as in Figure 3.2. Keevers and Green does not take into account the two possible mechanisms for charge carrier capture, but simply operate with electron capture and hole capture. To the best of my understanding, this means that the energy resulting from charge carrier capture is view as lost. Had part of the capture process been regarded as radiative, there would be a possibility for photon re-absorption. This possibility is discussed by Beaucarne et. al. [17]. They propose a model which differentiates between optical and thermal capture, that is, between C_n^{th} C_n^{op} and between C_p^{th} C_p^{op}.

The equations of the two models are found in the articles cited above ([6][17]). The equations themselves will not be discussed further in this thesis and are not included here. Two equations from the model of Keevers and Green are however used later in this thesis. These are the expressions for the absorption coefficients for the two sub band gaps, $\alpha_n(\lambda)$ and $\alpha_p(\lambda)$:

$$\alpha_n(\lambda) = f_{imp} N_{imp} \sigma_n^{op}(\lambda) \tag{3.20}$$

and

$$\alpha_p(\lambda) = \left(1 - f_{imp}\right) N_{imp} \sigma_p^{op}(\lambda), \tag{3.21}$$

where λ is the photon wavelength and σ_n^{op} and σ_p^{op} are the electron and hole photo-ionization cross section, respectively.

3.3 The Lucovsky model for the Photo-Ionization Cross Section

In 1965, Lucovsky [4] published a model with the the following expression for the photo-ionization cross section, σ^{op}:

$$\sigma_{op}(\hbar\omega) = \frac{1}{n_r}\left(\frac{E_{eff}}{E_0}\right)^2 \frac{16\pi q^2 \hbar}{3m^* c} \; \frac{E_i^{1/2}\left(\hbar\omega - E_i\right)^{3/2}}{(\hbar\omega)^3}, \tag{3.22}$$

where $\hbar\omega$ is the photon energy, n_r is the refractive index, $\frac{E_{eff}}{E_0}$ is the effective field ratio, q is the elementary charge, $\hbar$ is Planck's constant, m^* is the effective mass of the charge carrier, c is the speed of light in a vacuum and E_i is the ionization energy.

In 1970, this expression was slightly reformulated by Güttler and Queisser [5]:

$$\sigma(\hbar\omega) = \frac{1}{n_r}\left(\frac{E_{eff}}{E_0}\right)^2 \frac{4q^2 \hbar}{3\epsilon_0 m^* c} \; \frac{E_i^{1/2}\left(\hbar\omega - E_i\right)^{3/2}}{(\hbar\omega)^3}, \tag{3.23}$$

where ϵ_0 is the vacuum permittivity.

Other models for the photo-ionization cross section have been suggested, for example by Grimmeiss and Ledebo [18] and by Edwards and Fowler [19]. They will not be treated in this thesis.

3.4 Terminology

Table 3.1 provides an summary of terms related to the IPV effect, with the meaning ascribed to them in this thesis.

Table 3.1: Summary of various terms related to the IPV effect and the meaning ascribed to them in this thesis.

Term	Symbol	Description
IPV effect		Impurity photovoltaic effect. The optical generation of charge carriers via an impurity level in the band gap of a semiconductor.
IPV solar cell		Solar cell with the IPV effect included.
Conventional SRH recombination rate	U_{SRH}	The SRH recombination rate in the model of Shockley, Read [15] and Hall [16], presented in section 3.1. Does not take the IPV effect into account, that is, optical emission processes are not included.
IPV1 SRH recombination rate	U_{SRH}^{ipv1}	The SRH recombination rate in the model of Keevers and Green [6], presented in section 3.2. Does include the IPV effect, but is not concerned with the possibility of optical capture of charge carriers. A net generation of charge carriers is indicated by a negative U_{SRH}^{ipv1}.
IPV2 SRH recombination rate	U_{SRH}^{ipv2}	The SRH recombination rate in the model of Beaucarne et al. [17]. Includes the possibility for optical capture of charge carriers.
Electron and thermal capture cross section	σ_n^{th} and σ_p^{th}	Measure of probability of thermal capture of charge carriers by the impurity.
Electron and hole photo-ionization cross section	σ_n^{op} and σ_p^{op}	Measure of probability of optical emission of charge carriers from impurity.

Chapter 4

SCAPS: A Solar Cell Simulation Software

This chapter provides an introduction to the software used for the solar cell simulations presented in this thesis, SCAPS, and describes the most relevant functionality.

The content of this chapter is mostly based on the program's manual [20] and a getting started document [21], both found on the SCAPS installation website, available on request from Honorary Professor Marc Burgelman (Marc.Burgelman@ugent.be). To some extent it is also based on the journal articles of refs. [7] and [22]. The figures in this chapter are screenshots of the SCAPS software user interface.

Sections 4.1, 4.2 and 4.3 of this chapter are reworked from the corresponding chapter in my specialization project report [10], and included for completeness. The rest of the chapter (sections 4.4-4.7) is written solely for the master's thesis.

4.1 Introduction to SCAPS

SCAPS (**S**olar Cell **Cap**acitance **S**imulator) is a one-dimensional solar cell simulation software. It is developed by Marc Burgelman, Alex Niemegeers, Koen Decock, Johan Verschraegen and Stefaan Degrave at the Department of Electronics and Information Systems (ELIS) at the University of Gent, Belgium. The software is presented in several publications, a selection of which is given in refs. [7], [22]–[25]. Ref. [7] is considered the basic reference. Ref. [22] presents the algorithms used to simulate multivalent defects. Refs. [23]–[25] are not relevant for the current work, but deals with other features of SCAPS, such as intra-band tunneling and metastable defects.

SCAPS allows the user to "build" a solar cell structure with up to seven layers, in addition to the front and back contact. A range of material properties can be set for each layer, including dopant atom density, which naturally determines whether a layer is p- or n-type. It is recommended to simulate pn-structures, that is, with the p-type layer(s) to the left and the n-type layer(s) to the right. SCAPS is optimized for this configuration, and simulations of np-structures are less stable. The user can, however, freely choose which layer to illuminate. As such, using pn-structures should not be a problem.

Radiative, Auger and Shockley-Read-Hall (SRH) recombination can be included, in addition to surface recombination velocity at the contacts. Properties of the interfaces between layers can be set. Different tunneling mechanisms can be included. Absorption can be determined by different models or by files containing information about the absorption

coefficient. Defects and impurities can be introduced. A range of parameters can be set to determine the properties of the defects/impurities, including those governing the impurity photovoltaic effect.

Illumination can be turned off or on. The illumination can be determined by different models or by files containing information about the solar spectrum. In either case, the generation through the cell is calculated. Alternatively, profiles for generation can be set directly. Series and shunt resistances can be included.

The types of simulations that can be performed include current-voltage, capacitance-voltage, capacitance-frequency and quantum efficiency simulations. There is also an option for batch calculations, in which one or more cell parameters can be varied over a freely chosen range. A recorder option enables the user to keep track of a chosen parameter (such as the efficiency) as a function of the cell parameter(s) varied by the batch calculation.

The results of the simulations are presented graphically, with some key results, such as cell efficiency, directly displayed. The data sets for the graphs can be saved in files for further use, for example to plot in other software. Results are generated from the simulation types mentioned above, in addition to energy band diagrams and occupation probability among others.

SCAPS includes a curve fitting facility, in which a parameter or several parameters can be adjusted in order for the simulation results to match an experimentally measured curve.

There is also a possibility for running SCAPS by the use of scripts, making it possible to write a "recipe" with instructions for SCAPS to execute. This can be a useful way to save settings and actions when doing simulations, making it easy to redo the simulations later if necessary.

Finally, the user is encouraged not to use too extreme values for the input parameters and not to simulate unphysical situations, as this reduces the stability of the simulations.

4.2 Performing Simple Simulations

4.2.1 Action Panel

When running the SCAPS software, the Action Panel is the first panel (or window) seen. A screenshot of this panel is shown in Figure 4.1. Several setting are controlled from here. Most relevant for the current work are the illumination and which simulations to run. The illumination can be turned off (Dark) or on (Light). Turning it on enables the choice of spectrum and incident light power among other things. Which simulations to run is determined in the section of the Action Panel called "Action". The interval of for example the voltage (for IV simulations) can be defined, as well as the voltage increment.

Once the cell is defined as explained in the following sections, the simulations are started by pressing the "Calculate: single shot"-button" (or one of the buttons below for batch, recorder, curve fitting or script simulations) in the lower left corner of the Action Panel.

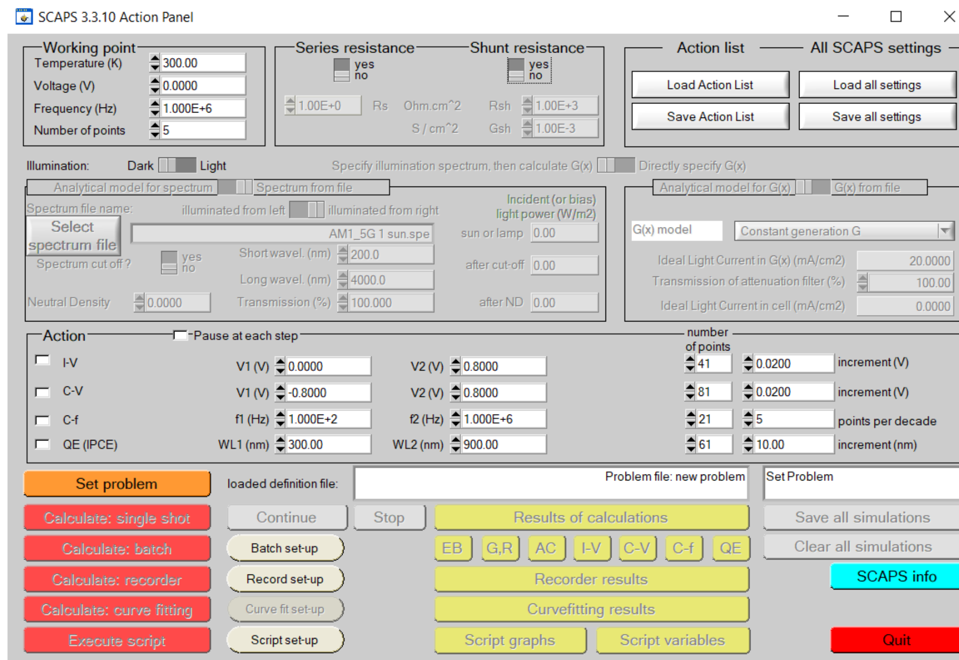

Figure 4.1: Screenshot of the Action Panel in the SCAPS software. This is the first panel encountered when running the program.

4.2.2 Solar Cell Definition Panel

Pressing the "Set problem"-button on the Action Panel opens the Solar Cell Definition Panel. A screenshot of this panel is shown in Figure 4.2. This panel allows the user to "build" a solar cell, by defining its structure. Once a structure is complete it can be saved as a definition file and loaded later. In Figure 4.2, the reference cell used in this work is loaded. Up to seven layers can be included, in addition to contacts and interfaces. Pressing one of the buttons of the layers, contacts or the interfaces opens a new panel to define the parameters of this part. The structure of the solar cell is shown in the upper right corner of the panel. Once a layer is defined by its doping concentration as p-type it appears red in this illustration. Once defined as n-type, it appears blue. Intrinsic layers appear green. Some other settings are also available from this panel, such as current and voltage references (controlling for example which quadrant the current-voltage characteristics will be plotted in) and numerical settings.

As mentioned in section 4.1, SCAPS works best with pn-structures, with the p-layer(s) to the left and the n-layer(s) to the right. Which layer is illuminated, however, is flexible. The setting controlling this is the "illuminated from:"-setting in the Solar Cell Definition Panel, where "left" and "right" are the options. That is, which layer is illuminated is not directly determined, but also depends on the structure of the cell. However, if pn-structures are used consistently, "illuminated from left" will be equivalent to the cell being illuminated on the p-layer or p-side, and "illuminated from right" will be equivalent to the cell being illuminated on the n-layer or n-side. This is illustrated by the screenshots in Figure 4.3. In Figure 4.3(a), the cell is illuminated from left (on the p-side), and in Figure 4.3(b), the cell is illuminated from the right (on the n-side). The light is indicated by the multicolored arrows. Notice also (in the left part of the figures), how the contacts alternate between being the front and back contact when the illuminated layer changes.

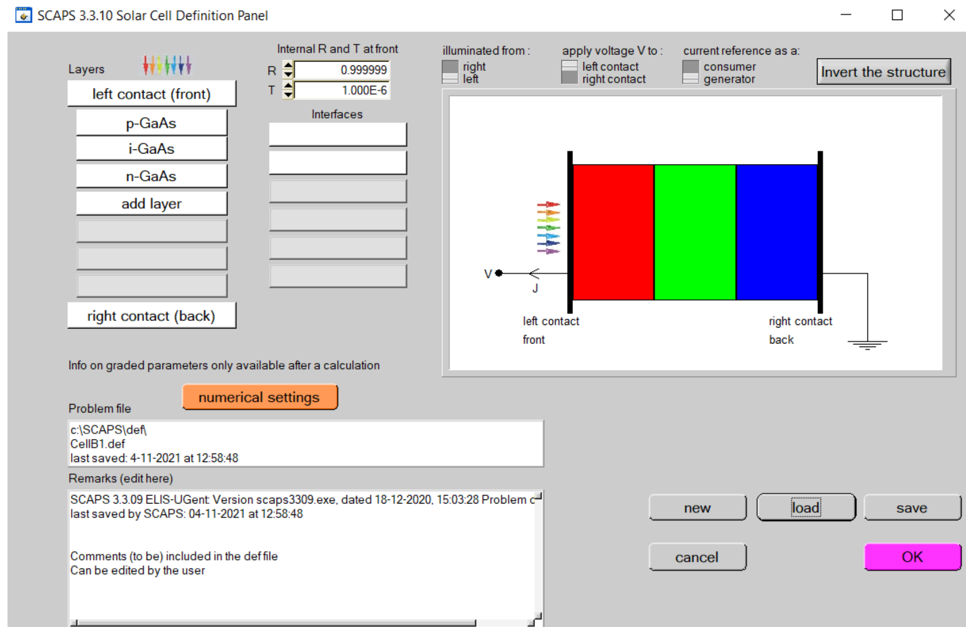

Figure 4.2: Screenshot of the Solar Cell Definition Panel in the SCAPS software. The structure of the solar cell is set here and shown in the upper right corner of the panel. The p-layer is red, the IPV-layer is green and the n-layer is blue.

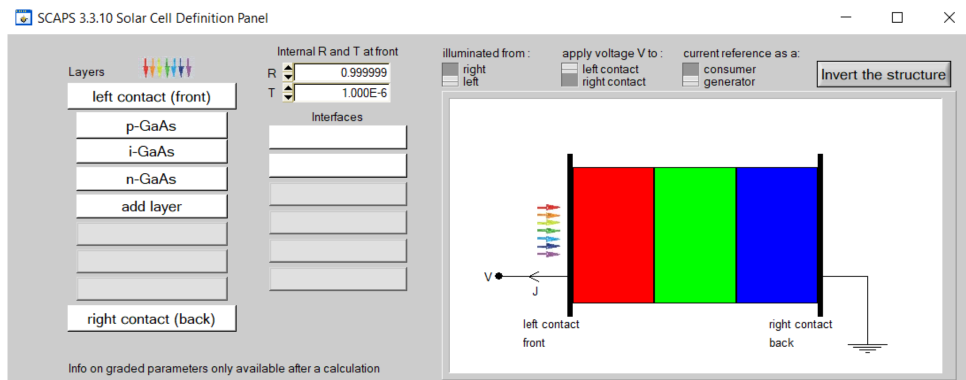

(a)

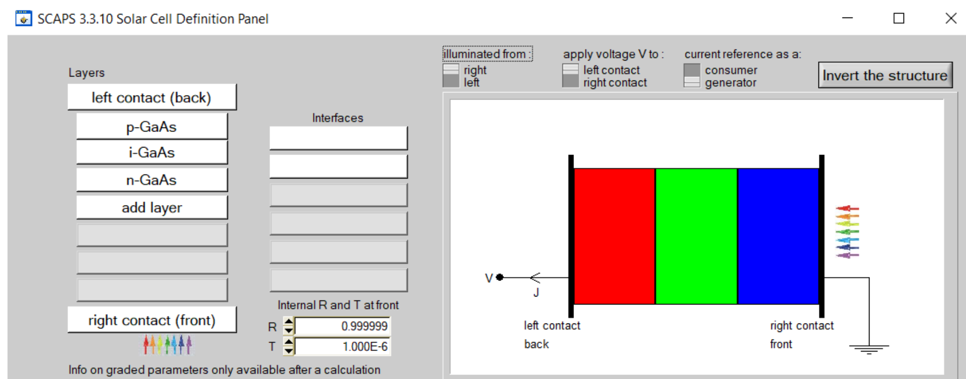

(b)

Figure 4.3: Screenshots of the upper part of the Solar Cell Definitions Panel in the SCAPS software, illustrating illumination on **(a)** the p-layer and **(b)** the n-layer. The light is indicated by the multicolored arrows.

4.2.3 Layer Properties Panel

Pressing one of the buttons of one of the layers in the Solar Cell Definition Panel opens the Layer Properties Panel of that layer. Figure 4.4 shows a screenshot of this panel for the p-layer of the reference cell used in this work. To a large degree, the settings in this panel determines the properties of the semiconductor material in the cell. Among the parameters possible to adjust from this panel are the layer thickness, the absorption coefficient and different recombination mechanisms. Defects can be added by clicking the button "Add a Defect 1". The panel that opens allows the user to enter values for the defect parameters. This will be described in more detail in section 4.4 later in this chapter.

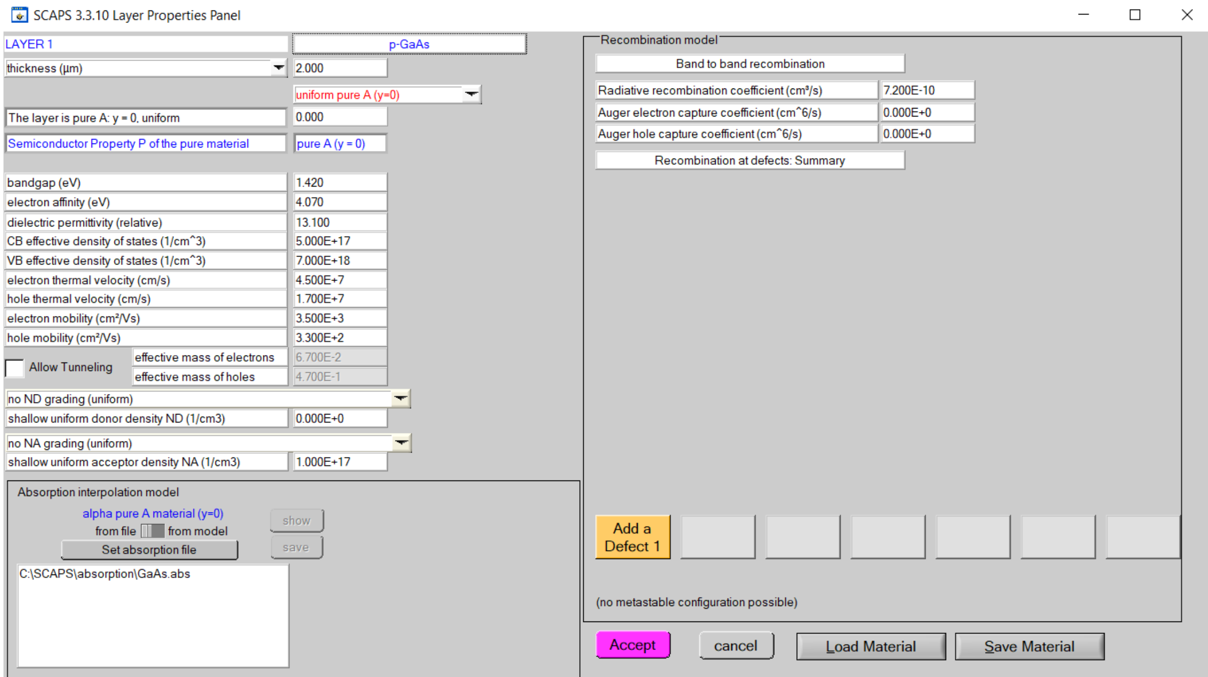

Figure 4.4: Screenshot of the Layer Properties Panel in the SCAPS software. It opens when pressing the button of one of the layers in the Solar Cell Definition Panel (Figure 4.2), in this case the layer called "p-GaAs". Most of the material parameter values are entered into this panel.

4.2.4 Contacts

After at least one layer has been defined, the properties of the front and back contacts can be set by clicking either the "left contact"- or "right contact"- button on the Solar Cell Definition Panel. A contact panel will then open. A screenshot of this panel is shown in Figure 4.5. Electrical properties, such as surface recombination velocity of electrons and holes, can be set, as well as the properties of an optical filter. When enabled, the optical filter can be defined by entering the fraction of incident radiation to be reflected or transmitted. Alternatively, the filter can be defined by a file, in which the transmission/reflection can be given for a range of wavelengths. When the optical filter of the back contact is enabled, a setting for the internal reflection/transmission at the front contact appear in the Solar Cell Definition Panel, see Figure 4.2. For the front contact, the reflected radiation is what does not enter the cell. For the back contact, the reflected radiation is what is reflected back into the cell. The internal reflection at the front contact is a measure of how much of the radiation reaching the front contact from inside the cell is reflected back into the cell.

As such, efficient light trapping is achieved with low front contact reflection and high back contact and internal front contact reflection.

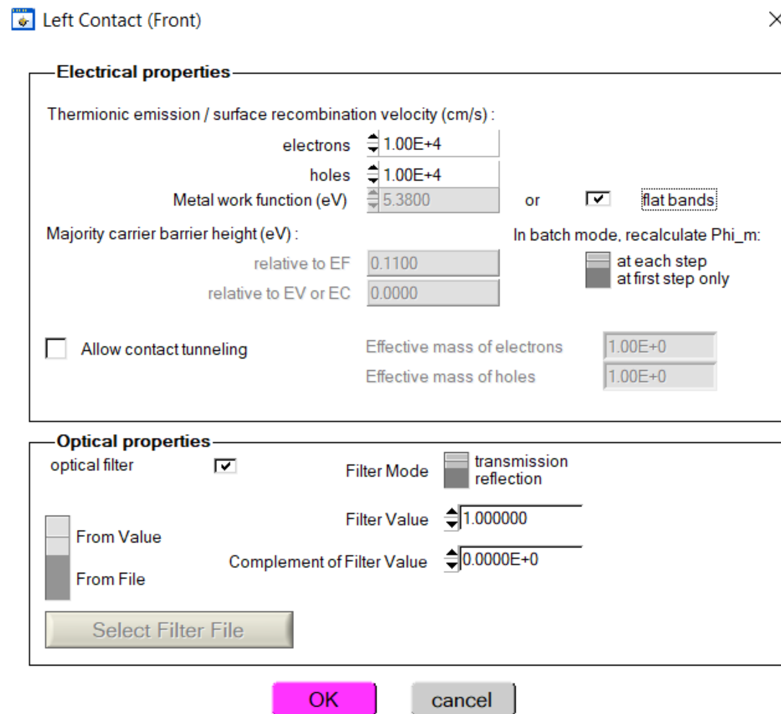

Figure 4.5: Screenshot of a contact panel (in this case the left contact) in the SCAPS software. Values for electrical and optical parameters of the contact are entered here.

4.3 Summary of the Simulation Procedure

Once a cell structure and parameter values are set and saved in a file, starting another simulation is done relatively quickly. SCAPS has a rather comprehensive functionality, but many simulations can be done with most settings kept at the SCAPS default option. Furthermore, in this work, most parameters are kept at fixed values, while one (or a few) parameter values are adjusted to see the influence this/these parameter(s) has on the cell performance.

The essence of preparing a simulation is therefore to load a definition file, adjust the relevant parameters either in the Layer Properties Panel, the Solar Cell Definition Panel or in the batch settings, turn on the illumination and select which simulation(s) to run. A summary of the procedure is given in the following list:

- Launch SCAPS.
- Turn on the illumination.
- Chose what simulation(s) to run and specify the interval(s) and increment(s). When the illumination is turned on, an option called "Stop after Voc" appears next to the voltage interval of the I-V simulation. Checking this makes the IV simulation(s) stop after the voltage reaches V_{OC}, even if the defined voltage interval exceeds V_{OC}.
- Set the problem by creating a cell structure or loading an existing definition file.
- Adjust the relevant cell parameters.

- If relevant, set the batch settings by clicking the button "Batch set-up".
- If relevant, set the recorder settings by clicking the button "Record set-up".
- To clear previous simulations, click the button "Clear all simulations".
- Press the button "Calculate: single shot" (or the buttons "Calculate: batch" or "Calculate: recorder" if relevant) to start the simulation(s).

4.4 Introducing Impurities and Defects

Impurities and defects can be introduced into each semiconductor layer of the solar cell structure. SCAPS does not differentiate between impurities and defects, but simply allows the user to enter values of a set of parameters determining the effect of the impurities/defects on the cell performance. Although the current work deals with impurities, this chapter will use the term defects, as this is also used in the SCAPS user interface.

The defect parameters are available on the Layer Properties Panel, by clicking the button "Add a Defect 1" (see Figure 4.4). The Defect Properties Panel will then open. A screenshot of this panel is shown in Figure 4.6. After specifying one defect, a button for defining a second one appears on the Layer Properties Panel. Up to seven defects can be added for each semiconductor layer.

In the Defect Properties Panel, the defect type can be set to neutral, single donor, single acceptor or multivalent (either double donor, double acceptor, amphoteric or custom defined multilevel). If one of the multivalent types are selected, the Multiple Level Defects Properties Panel opens. Here, the charge states, energy levels and other parameters of the multivalent defects can be set. Back on the Defect Properties Panel next parameter to set is the thermal capture cross section for electrons and holes, describing the probability of either charge carrier being captured by the defect. Furthermore, the energy level and density of the defect can be set.

The parameters governing the IPV effect can also be set on the Defect Properties Panel, by enabling the options that in SCAPS are called "Optical capture of electrons" and "Optical capture of holes". Note that this terminology and the one used in this thesis differ. What is called "optical capture" on the Defect Properties Panel is what in this thesis is referred to as photo-ionization. The photo-ionization can either be set by a file containing information on the photo-ionization cross section as a function of wavelength, or by use of a model implemented in SCAPS. In the latter case, the values of four parameters must be entered and SCAPS will calculate the photo-ionization cross section. How the photo-ionization cross sections are calculated is described in the next section.

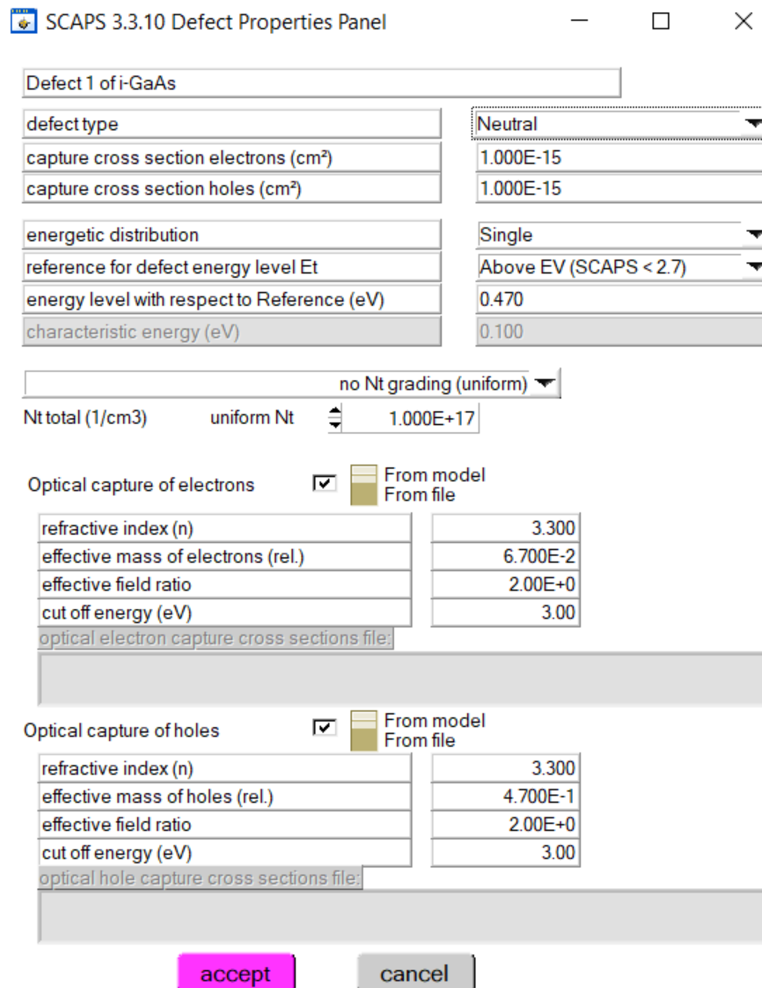

Figure 4.6: Screenshot of a Defect Properties Panel in the SCAPS software. Defect/impurity parameter are set here.

4.5 Implementation of the IPV effect in SCAPS

SCAPS uses the model of Keevers and Green [6] (section 3.2), with a few minor deviations. In SCAPS, free carrier absorption is not considered, the impurity level degeneracy factor, g_t (equation (4) in ref. [6]) is set to 1, and the factor of 2 in equations (4a) and (4b) in ref. [6] is not applied (personal communication with Marc Burgelman, e-mail, 19.08.21 and 04.11.21).

To calculate the photo-ionization cross sections, SCAPS uses the Lucovsky model [4], the way it is formulated by Güttler and Queisser [5]. That is, SCAPS calculates the photo-ionization cross sections by using equation (3.23) (personal communication with Marc Burgelman, e-mail, 24.02.21).

Only nine of the twelve theoretically possible transitions depicted in Figure 3.2 are considered by SCAPS. Optical band-to-band recombination is not applied, in the sense that all band-to-band recombination is viewed as lost. Photon recycling is not considered, meaning that the possibility for re-absorption of photons emitted by optical band-to-band recombination is not applied. Neither is optical capture of electrons and holes, again meaning that SCAPS views all the carrier capture as loss without potential for emission and re-absorption of photons. Referring to Figure 3.2 in Chapter 3, it means R^{op}_{btb}, C^{op}_n and C^{op}_p are not included

in SCAPS (personal communication with Marc Burgelman, e-mail, 19.08.21, 04.11.21 and 08.11.21). For more details on SCAPS implementation see Appendix C.2 and C.3.

4.6 Displaying and Saving Results

Once a simulation is run, SCAPS automatically opens the Energy Bands Panel (or the ac Energy Bands Panel if a capacitance-frequency simulation is run). A screenshot of the Energy Bands Panel is shown in Figure 4.7. The energy bands are shown in the top left corner of the panel. When running current-voltage or capacitance-voltage simulations, the user can see how the band diagram evolves as the voltage varies over the predefined interval. When the simulations are done, the band diagram is displayed for the last voltage value used in the calculations. For current-voltage simulations, this is the last value of the defined voltage interval. For quantum efficiency simulations, this will equal the voltage at which the quantum efficiency is calculated, defined by the working point voltage on the Action Panel. Also shown on the Energy Bands Panel are the carrier densities, the current densities and the occupation probability of deep defects (if applicable for the simulated cell), all as a function of position in the cell.

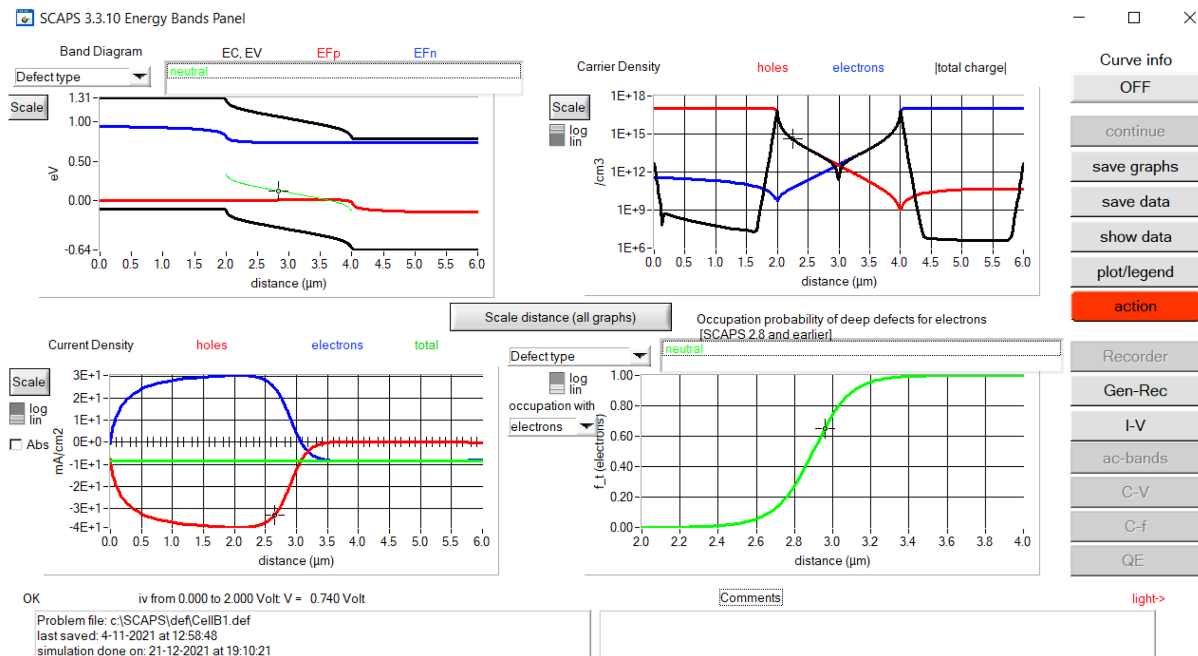

Figure 4.7: Screenshot of a Energy Bands Panel in the SCAPS software after running a simulation. Other panels can be accessed and results can be saved by clicking the appropriate buttons to the right.

When the simulations are done, the user can navigate to other result panels by clicking the appropriate button in the right part of the Energy Bands Panel. Which panels are available depends on which simulations have been performed. For example, pressing the "Gen-Rec"-button opens the Generation-Recombination Profiles Panel. This panel provides information on the generation as well as different recombination, capture and emission rates, as a function of position in the cell. Pressing the "I-V"-button opens the I-V Panel, where the current-voltage characteristics are shown. The cell efficiency, open circuit voltage, short circuit current density and fill factor are also displayed. Pressing the "QE"-button opens the QE Panel, showing the quantum efficiency as a function of either wavelength or

photon energy.

On the result panels, there are several settings to change the appearance of the graphs. Most of them are quite intuitive, the "lin/log"-switch for example changes the axis in question between linear and logarithmic. A few are less self-explanatory. Right-clicking on the button "plot/legend" in the right part of a result panel opens the Graph Legend Panel, in which the user can select which curves to show. If a batch simulation has been performed, The Graph Legend Panel also provide information about the batch parameter values for each curve, making it easier to keep track of the results when comparing several curves. An easy way to zoom in on a section of a graph is to press and hold the Ctrl-button on the keyboard while selecting the area of interest with the mouse pointer. To zoom out, hold the Ctrl-button pressed and right click on the mouse.

Results from SCAPS can be saved in different ways. Images of the various result panels can be saved as image files or pdf files, useful for quick overviews of simulations. The data of the curves can also be saved in text files, useful for further analysis and plotting by use of other software.

4.7 Scripting

There are several possible uses of the scripting facility in SCAPS. In this thesis, scripting is used to create a "recipe" of instructions for SCAPS to execute. This functionality is the topic of this section. The most relevant parts of the scripting language is also presented. Details of other uses of scripting and a complete overview of the scripting language can be found in the SCAPS manual [20].

A script can be written in a standard text file and read by SCAPS. However, it is strongly encouraged to use the script editor of the SCAPS user interface. The editor provides suggestions for commands and arguments, making the writing of the script more intuitive and reducing the chance of typing and syntax mistakes.

The script editor is accessed from the Action Panel, by clicking the button "Script set-up". This opens the Script Editor Panel, shown in Figure 4.8. The script is written in the upper field of the Script Editor Panel and suggestions appear in the bottom fields. Scripts can be saved and loaded using the appropriate buttons in the right part of the Script Editor Panel.

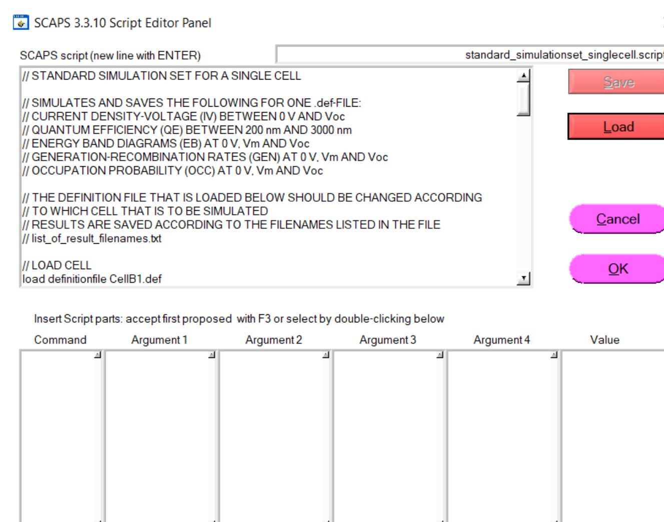

Figure 4.8: Screenshot of a Script Editor Panel in the SCAPS software. Here a script used to run a standard set of simulation for a given cell is loaded.

Each command line is constructed in the same way. First, a *command* tells SCAPS which action to perform. Second, one or several *arguments* indicate on what the action should be performed. Third, when relevant, a *value* is specified. A double slash, //, can be used to indicate the start of a comment.

An example of a script is given in Appendix A. The use of some of the commands in SCAPS scripts are given in the following.

Files are loaded with the *load* command and saved with the *save* command. Settings on the Action Panel are given with the *action* command. The *clear* command can be used for example to clear previously performed simulations. Values can be assigned to design and material parameters by use of the *set* command, and values of performance parameters can be extracted for further use in the script by the *get* command. The *show* command is used to display the internal variables in the script (if any), and is useful for debugging while writing a script. The *calculate* command is used for starting calculations. Finally, the *run* command is used to run a script within a script. By writing parts of the script in own files, the main script becomes more readable.

Chapter 5

SCAPS Simulations of GaAs IPV Solar Cells

This chapter contains information on how SCAPS has been used in the current work, as well as details of all the simulations done. First, general settings and parameters used throughout the work are presented. Next, the parameters of an impurity free cell are given. Then a reference cell (with impurities) is presented. This will serve as a staring point for the subsequent simulations. The rest of the chapter is devoted to details of the simulations done to test SCAPS as a tool for simulating IPV solar cells and to determine the influence of a set of design and impurity parameters on cell performance. The performance of the impurity free cell will be compared to the performance of those with impurities in order to determine whether the introduction of impurities has a positive or negative influence on the cell performance. In light of this, IPV cells' potential can be discussed.

The information in this chapter is intended as an overview of parameters, settings and technical aspects of the simulations. It will prepare the reader for the results presented in Chapter 6. A more thorough explanation and motivation for the various simulations are found in the beginning of each section in Chapter 6, as an introduction to the results and discussion of that section. There are many different simulations to keep track of, so this is done to make it easier to follow Chapter 6 without having to go back and fourth between this chapter and Chapter 6. When in need of specific values for a parameter in a given cell, the current chapter will be a useful place to look up such details.

5.1 General Settings and Parameters

5.1.1 Versions of the SCAPS software

In the beginning of the current work, SCAPS version 3.3.09 was used. A minor bug was discovered in this version. The bug was related the output data and plot of the hole optical emission rate, E_p^{op}. Only E_p^{op}, and thereby the net recombination from the conduction band to the impurity level, were affected. Other results of the simulations were not based on these rates and were therefore not affected by the bug. The bug was discovered when doing simulations of the SRH recombination in SCAPS (simulation details in subsection 5.4.1 of this chapter, results in subsection 6.3.1 of Chapter 6). It was reported to and corrected by SCAPS developer Honorary Professor Marc Burgelman (personal communication, e-mail, 19.08.21).

At the time the bug was discovered, the newest version of SCAPS was SCAPS 3.3.10. Therefore, I installed the latest update of SCAPS 3.3.10, dated 20.08.2021. In this update the bug was corrected.

The simulations of the SRH recombination rate were done with both SCAPS version 3.3.09, and with the latest update of version 3.3.10. This was done to compare the results generated with the two versions and to verify that the bug was corrected. It is clearly stated in subsections 5.4.1 and 6.3.1 which simulations are performed with which version. All other simulations are performed with the latest update (dated 20.08.21) of version 3.3.10.

More details and the answer from Marc Burgelman are found in section C.3 of Appendix C (the correction of the bug is treated in the end of C.3).

5.1.2 Settings Used for All Simulations

All the simulations presented in this thesis are performed under the following conditions:

- Current density-voltage (IV) simulations are run from 0 V to 2 V with the option "stop after Voc" enabled. The increment of the simulations is 0.01 V.
- Quantum efficiency (QE) simulations are run from 200 nm to 1000 nm (if the IPV effect is disabled) or from 200 nm to 3000 nm (if the IPV effect is enabled and 0.47 eV ≤ E_{imp} ≤ 0.95 eV). The increment is 5 nm. The QE simulations are run at 0 V.
- Energy band (EB) diagrams are presented at 0 V, voltage of maximum power (V_M) or at the open-circuit voltage (V_{OC}).
- Occupation probabilities (OCC) are presented at 0 V, V_M or V_{OC}. It is always occupation with electrons that is shown.
- Generation-recombination (GEN) rates are presented at 0 V, V_M or V_{OC}.

The following settings are used for all simulations presented in this thesis. The meaning of all these settings might not be intuitive, and they are not necessarily relevant for the results and discussion in the next chapter. They are included to provide complete information of the simulations and to make it easier to reproduce the results.

- The illumination is on
- Illumination spectrum is specified, then G(x) is calculated (as opposed to directly specifying G(x))
- Spectrum is defined from file (as opposed to from analytical model)
- No spectrum cut off, natural density is set to zero, the incident light power is 1000 W/m^2
- The cells are illuminated from left, voltage is applied to left contact, current reference as a generator
- The structure is always p-IPV-n, that is with the p-layer to the left, the IPV-layer in the middle and the n-layer to the right
- No interface properties are defined
- No tunneling mechanisms are enabled
- No series or shunt resistance is enabled
- No grading options (for defects or elsewhere) are applied

- Defect energetic distribution is set to single
- Reference for defect energy level is above E_V

5.1.3 Parameters kept at fixed values

Table 5.1 lists material, design and working point parameters that are fixed for all simulations. Unless stated otherwise, the parameter values apply to all layers/both contacts.

Table 5.1: Parameters kept at fixed values.

Parameter	Symbol	Value	Ref.
Material parameters			
Band gap	E_g	1.42 eV	[2]
Electron affinity	χ	4.07 eV	[2]
Relative dielectric permittivity	ϵ	13.1	[2]
Effective density of states in the conduction band	N_C	5×10^{17} cm^{-3}	[2]
Effective density of states in the valence band	N_V	7×10^{18} cm^{-3}	[2]
Thermal velocity of electrons[2]	v_n^{th}	4.5×10^7 cm/s	[2][12]
Thermal velocity of holes[2]	v_p^{th}	1.7×10^7 cm/s	[2][12]
Effective mass of electrons	m_n^*/m_0	0.067	[2]
Effective mass of holes	m_p^*/m_0	0.47	[2]
Radiative recombination coefficient	K_{rad}	7.2×10^{-10} cm^3/s	[20]
Electron surface recombination velocity	S_n	10^4 cm/s	[26][3]
Hole surface recombination velocity	S_p	10^4 cm/s	[26][3]
Electron mobility, n-layer and IPV-layer	μ_n	5000 cm^2/(V s)	[27]
Electron mobility, p-layer	μ_n	3500 cm^2/(V s)	[27]
Hole mobility, p-layer and IPV-layer	μ_p	330 cm^2/(V s)	[27]
Hole mobility, n-layer	μ_p	120 cm^2/(V s)	[27]
Front contact reflection	R_f	0 %	
Design parameters			
n-Layer thickness	d_n	2 µm	
p-Layer thickness	d_p	2 µm	
Shallow donor density, n-layer	N_D	10^{17} cm^{-3}	
Shallow acceptor density, p-layer	N_A	10^{17} cm^{-3}	
Working point parameters			
Temperature	T	300 K	
Voltage[4]	V	0 V	
Frequency	f	10^6 Hz	
Number of points		5	

[2] Calculated using equation (2.8) [12, p. 44] with values for the relevant constants taken from ref. [2, pp. 263-264].

[3] And references therein.

[4] For IV and QE simulations a working point voltage of 0 V is used. EB, GEN and OCC simulations are run at 0 V, V_M or V_{OC}.

The solar spectrum and band-to-band absorption coefficient used in the simulations are plotted in Figure 5.1 and Figure 5.2, respectively. Both are included as files in the SCAPS installation ("AM1_5G 1 sun.spe" and "GaAs.abs"). The absorption coefficient is used in all layers.

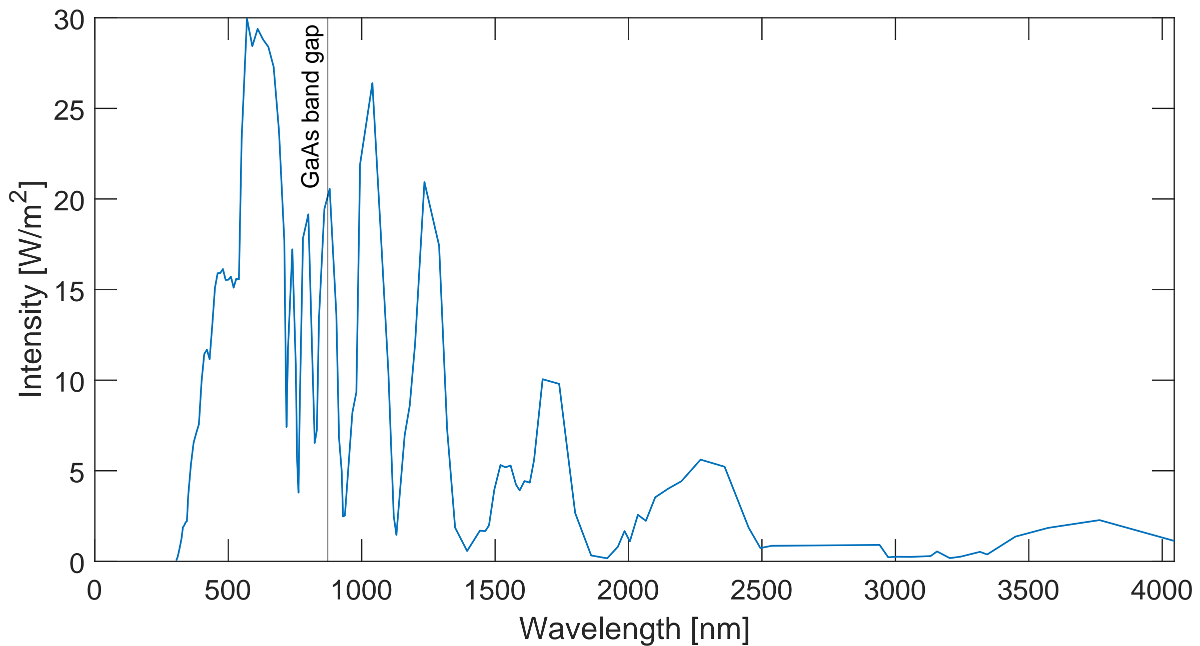

Figure 5.1: The solar spectrum used in the simulations (found in the file "AM1_5G 1 sun.spe" in the SCAPS installation). The spectrum is a one-sun AM1.5 spectrum normalized to an intensity of 1000 W/m^2. The wavelength corresponding to the GaAs band gap is indicated with a vertical line. Note that the y-axis is in units of W/m^2, and not the perhaps more commonly used unit W/(m^2 nm).

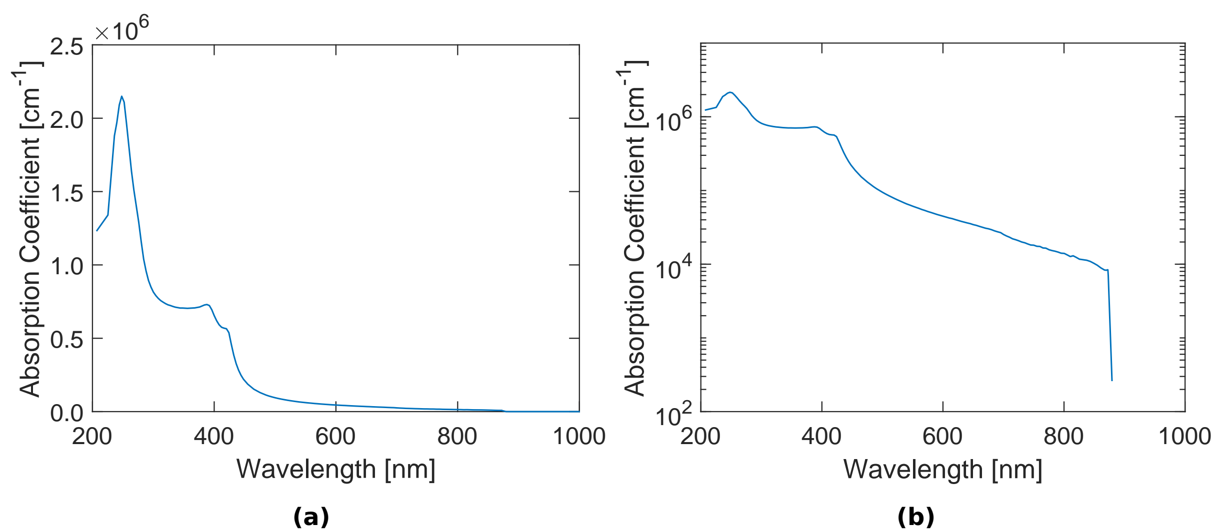

Figure 5.2: (a) Linear and **(b)** logarithmic plot of the GaAs band to band absorption coefficient (α_{btb}) used in the simulations (found in the file "GaAs.abs" in the SCAPS installation).

5.1.4 Numerical Settings

For almost all simulations the SCAPS default numerical settings are used. In some cases, when convergence failures were encountered, these were somewhat adjusted before the simulations were rerun. Adjustments that can be made include increasing the maximum number of iteration steps, increasing the termination criterion thresholds and decreasing the clamping factor. More information on the numerical settings, parameters and limitations, see the SCAPS manual [20].

The numerical settings were changed in the following cases:

- QE simulation of Cell B1: Clamping factors (for electrostaic potential, electron Fermi level and hole Fermi level) were set to 0.1.
- QE simulation for Cell C1: Done in the samme manner as for B1 in order to make the two simulations as comparable as possible.
- IV simulations of Cells E27 and E44 resulted in convergence errors when simulating as a batch. When repeated as single simulations, no error occured, so there was no need to change the numerical settings.
- IV simulations of Cells F2 and F5. I was unable to avoid convergence failure. The results of the simulations up until the convergence failure are included in Chapter 6. The simulations of these results were run with clamping factors set to 0.1 and maximum number of iterations set to 3000.

5.1.5 Overview of Cells and Simulations

The simulated cells are organized in groups according to what they are used to study. Each group is assigned a letter. Within the groups the individual cells are distinguished by a number following the letter. A description of the groups of cells are given in Table 5.2.

Table 5.2: Overview of the groups of simulated cells.

Group of cells	Description
A (Cells A1 and A2)	Impurity free cells. Used for comparison with the other cells to determine the potential for IPV cells.
B (Cells B1 and B2)	Cell B1 is chosen as the reference cell. Impurities are included in the IPV-layer of this cell and all following cells. Parameters of Cell B1 are partly taken from literature, partly chosen. It is used as a starting point for the following cells. Cell B2 is used for studying the implementation of SRH recombination in SCAPS.
C (Cell C1)	Only one cell. Used to study the implementation of the Lucovsky model for photo-ionization cross section in SCAPS.
D (Cells D1-D7)	Used to study the influence of the parameters in the Lucovsky model on cell performance.
E (Cells E1-E67)	Used to study the influence of thermal capture cross sections on cell performance.
F (Cells F1-F8)	Used to study the influence of the type of impurity (donor or acceptor) and the influence of shallow donor background doping.
G (Cells G1-G5)	Used to study the influence light trapping (by adjusting the internal front contact reflection).

The parameters that are not already given in subsection 5.1.3 are provided for the individual cells in the following sections. First the parameters of the impurity free cells are given. Then, a reference cell (Cell B1) is created, and its parameters are listed. To describe the cells following this reference cell, only the parameters with values deviating from those of the reference cell are listed. This is done in order to avoid extensive repetition.

5.2 Parameters of the Impurity Free Cells

There are two impurity free cells, Cells A1 and A2. The values of the parameters not already given in subsection 5.1.3 are listed in Table 5.3. As there are no impurities, there are few relevant parameters to list. The only difference between Cell A1 and A2 is that in Cell A1 there is no light trapping, whereas in Cell A2 the light trapping is set as high as possible (SCAPS will, quite understandably, not run simulations with $R_b = R_{fi} = 100\,\%$).

Table 5.3: Parameters of Cells A1 and A2 (impurity free cells).

Parameter	Symbol	Value
Cell A1		
IPV-Layer thickness	d_{IPV}	2 µm
Back contact reflection	R_b	0 %
Internal front contact reflection	R_{fi}	0 %
Impurities		None
Cell A2		
IPV-Layer thickness	d_{IPV}	2 µm
Back contact reflection	R_b	100 %
Internal front contact reflection	R_{fi}	99.9999 %
Impurities		None

5.3 Parameters of the Reference Cell

The parameters of Cell B1 (chosen as reference cell) are listed in Table 5.4. In Cell B2 the IPV effect is disabled. This means that the bottom six parameters of Table 5.4 are not used for Cell B2. All the other parameters Cell B2 are equal to those of Cell B1.

The effective field ratio is discussed in ref. [28]. See also the answers from Marc Bugelman in Appendix C.1 (personal communication, e-mail, 22.09.20). By use of a simple model, E_{eff/E_0} is calculated to be approximately 4 for GaAs. However, there seems to be some uncertainty regarding this model, and to the best of my understanding ref. [28] argues that this model overestimates the effective field ratio. The value of 2 is therefore to some extent based on theory, but also to some extent merely chosen. As we will see later in this thesis, minor differences in this parameter has minimal influence on cell performance.

The cut-off energies for electrons and holes are the maximum photon energies at which optical emission of charge carrier from the impurity to the appropriate band occurs. In other words, the cut-off energies are where the photo-ionization cross sections are cut off.

Table 5.4: Parameters of Cell B1 (reference cell).

Parameter	Symbol	Value	Ref.
IPV-Layer thickness	d_{IPV}	2 μm	
Shallow donor density, IPV-layer	$N_{D,IPV}$	0 cm^{-3}	
Shallow acceptor density, IPV-layer	$N_{A,IPV}$	0 cm^{-3}	
Back contact reflection	R_b	100 %	
Internal front contact reflection	R_{fi}	99.9999 %	
Impurities		1 in IPV-layer	
Impurity type		Neutral	
Impurity energy level above E_V	E_{imp}	0.47	
Impurity density	N_{imp}	10^{17} cm^{-3}	
Electron thermal capture cross section	σ_n^{th}	10^{-15} cm^2	
Hole thermal capture cross section	σ_p^{th}	10^{-15} cm^2	
Refractive index	n_r	3.3	[12]
Effective field ratio	E_{eff/E_0}	2	[28]
Effective mass of electrons	m_n^*/m_0	0.067	[2]
Effective mass of holes	m_p^*/m_0	0.47	[2]
Cut-off energy electrons	E_n^{cut}	3 eV	
Cut-off energy holes	E_p^{cut}	3 eV	

5.4 Testing of SCAPS as a Tool for Simulating IPV Solar Cells

5.4.1 SRH Recombination in SCAPS

For testing how the SRH recombination rate is calculated in SCAPS, Cells B1 and B2 were used. Both cells were simulated with both SCAPS 3.3.09 and the latest update of SCAPS 3.3.10. This was done to compare the calculation of the SRH recombination rate in SCAPS in the two versions for a cell with (Cell B1) and without (Cell B2) the IPV effect enabled.

5.4.2 Implementation of the Lucovsky Model for Photo-Ionization Cross Section

To test the implementation of the Lucovsky model in SCAPS, the results of simulations with Cell B1 were compared to those of Cell C1. The only difference between the cells is the implementation of the Lucovsky model. In Cell B1, the internal model in SCAPS is used to calculate the photo-ionization cross sections, whereas in Cell C1 a MATLAB function is used to calculate the photo-ionization cross sections. Both cells use the same model and parameter values. The MATLAB function is given in Appendix B.

5.5 Varying Design and Impurity Parameters

5.5.1 Photo-Ionization Cross Section Parameters

Cells D1-D7 are used to test the influence of varying the parameters governing the photo-ionization cross sections. Table 5.5 lists the parameters of Cell D1-D7 that deviate from those of the reference cell.

Table 5.5: Parameters of Cells D1-D7 that deviate from the reference cell. All other parameters have the same values as in the reference cell (see section 5.3).

Cell	n_r	E_{eff}/E_0	m_n^*/m_0	m_p^*/m_0	E_n^{cut} **[eV]**	E_p^{cut} **[eV]**
Cell D1	1	10	6.7×10^{-3}	4.7×10^{-2}	3	3
Cell D2	3.3	2	6.7×10^{-2}	4.7×10^{-1}	1.42	1.42
Cell D3	3.3	2	6.7×10^{-2}	4.7×10^{-1}	3	0.95
Cell D4	3.3	2	6.7×10^{-2}	4.7×10^{-1}	1.42	0.95
Cell D5	1	10	6.7×10^{-3}	4.7×10^{-2}	1.42	0.95
Cell D6	3.3	2	6.7×10^{-6}	4.7×10^{-2}	1.42	1.42
Cell D7	3.3	2	6.7×10^{-9}	4.7×10^{-2}	1.42	1.42

Some of the parameter values given in Table 5.5, especially the effective masses are clearly unrealistic. The parameters are set too such extreme values in order to vary the photo-ionization cross sections over several orders of magnitude. This is, in turn, done to test the influence of the magnitude of the photo-ionization cross sections of cell performance.

5.5.2 Thermal Capture Cross Section

In Cells E1-E66, the thermal capture cross sections of electrons and holes were varied between $10^{-22}\,\mathrm{cm}^2$ and $10^{-12}\,\mathrm{cm}^2$ using the batch and recorder functionality in SCAPS. The variation was logarithmic, with steps of a factor 100 for electrons and 10 for holes. The cross sections were varied in a nested way, covering all combinations of σ_n^{th} and σ_p^{th}. Table 5.6 the parameters of the individual cells.

Based on values of σ_n^{th} and σ_p^{th} from literature [29][30], Cell E67 was created and simulated. The parameter values of Cell E67 are found in the bottom of Table 5.6.

Table 5.6: Parameters of Cells E1-E66 that deviate from the reference cell. All other parameters have the same values as in the reference cell (see section 5.3).

Cell	σ_n^{th} [cm^2]	σ_p^{th} [cm^2]	Cell	σ_n^{th} [cm^2]	σ_p^{th} [cm^2]
Cell E1		10^{-22}	Cell E34		10^{-22}
Cell E2		10^{-21}	Cell E35		10^{-21}
Cell E3		10^{-20}	Cell E36		10^{-20}
Cell E4		10^{-19}	Cell E37		10^{-19}
Cell E5		10^{-18}	Cell E38		10^{-18}
Cell E6	10^{-22}	10^{-17}	Cell E39	10^{-16}	10^{-17}
Cell E7		10^{-16}	Cell E40		10^{-16}
Cell E8		10^{-15}	Cell E41		10^{-15}
Cell E9		10^{-14}	Cell E42		10^{-14}
Cell E10		10^{-13}	Cell E43		10^{-13}
Cell E11		10^{-12}	Cell E44		10^{-12}
Cell E12		10^{-22}	Cell E45		10^{-22}
Cell E13		10^{-21}	Cell E46		10^{-21}
Cell E14		10^{-20}	Cell E47		10^{-20}
Cell E15		10^{-19}	Cell E48		10^{-19}
Cell E16		10^{-18}	Cell E49		10^{-18}
Cell E17	10^{-20}	10^{-17}	Cell E50	10^{-14}	10^{-17}
Cell E18		10^{-16}	Cell E51		10^{-16}
Cell E19		10^{-15}	Cell E52		10^{-15}
Cell E20		10^{-14}	Cell E53		10^{-14}
Cell E21		10^{-13}	Cell E54		10^{-13}
Cell E22		10^{-12}	Cell E55		10^{-12}
Cell E23		10^{-22}	Cell E56		10^{-22}
Cell E24		10^{-21}	Cell E57		10^{-21}
Cell E25		10^{-20}	Cell E58		10^{-20}
Cell E26		10^{-19}	Cell E59		10^{-19}
Cell E27		10^{-18}	Cell E60		10^{-18}
Cell E28	10^{-18}	10^{-17}	Cell E61	10^{-12}	10^{-17}
Cell E29		10^{-16}	Cell E62		10^{-16}
Cell E30		10^{-15}	Cell E63		10^{-15}
Cell E31		10^{-14}	Cell E64		10^{-14}
Cell E32		10^{-13}	Cell E65		10^{-13}
Cell E33		10^{-12}	Cell E66		10^{-12}
Cell E67	10^{-19}	10^{-16}			

5.5.3 Impurity Type and Shallow Background Doping

Cells F1-F8 use Cell E67 as a staring point, so $\sigma_n^{th} = 10^{-19}\,\text{cm}^2$ and $\sigma_p^{th} = 10^{-16}\,\text{cm}^2$. Cells F1 and F2 were used to test the influence of the impurity type, that is, whether the impurity is a single donor (don.) or acceptor (acc.). In cells F3-F7 the type of the deep level impurity was single acceptor. These cells were used to test the influence of varying shallow donor densities in the IPV-layer. Finally, based on the results of simulations of Cells F3-F7 and theory [2, p. 205], Cell F8 has a shallow donor density of $5 \times 10^{16}\,\text{cm}^{-3}$. The parameter of the individual cells are listed in Table 5.7.

Table 5.7: Parameters of Cells F1-F8 that deviate from the reference cell. All other parameters have the same values as in the reference cell (see section 5.3).

Cell	σ_n^{th} [cm^2]	σ_p^{th} [cm^2]	Type	$N_{D,IPV}$ [cm^{-3}]
Cell F1	10^{-19}	10^{-16}	Single acc.	0
Cell F2	10^{-19}	10^{-16}	Single don.	0
Cell F3	10^{-19}	10^{-16}	Single acc.	10^{15}
Cell F4	10^{-19}	10^{-16}	Single acc.	10^{16}
Cell F5	10^{-19}	10^{-16}	Single acc.	10^{17}
Cell F6	10^{-19}	10^{-16}	Single acc.	10^{18}
Cell F7	10^{-19}	10^{-16}	Single acc.	10^{19}
Cell F8	10^{-19}	10^{-16}	Single acc.	5×10^{16}

5.5.4 Internal Front Contact Reflection and IPV-Layer Thickness

Cells G1-G5 use Cell F8 as a starting point, meaning $\sigma_n^{th} = 10^{-19}\,\text{cm}^2$, $\sigma_p^{th} = 10^{-16}\,\text{cm}^2$, the type is single acceptor and $N_{D,IPV} = 5 \times 10^{16}\,\text{cm}^{-3}$. Up until now, all cells (with the exception of Cell A2) have had maximum light trapping, that is, with $R_b = 100\,\%$ and $R_{fi} = 99.9999\,\%$. This has been done to make the IPV effect more pronounced. As it is probably unrealistic, Cells G1-G5 are used to test how much the performance deteriorates when R_{fi} is reduced. The parameters of the individual cells are listed in Table 5.8.

Table 5.8: Parameters of Cells G1-G5 that deviate from the reference cell. All other parameters have the same values as in the reference cell (see section 5.3).

Cell	σ_n^{th} [cm^2]	σ_p^{th} [cm^2]	Type	$N_{D,IPV}$ [cm^{-3}]	R_{fi} [%]
Cell G1	10^{-19}	10^{-16}	Single acc.	5×10^{16}	99.999
Cell G2	10^{-19}	10^{-16}	Single acc.	5×10^{16}	99.99
Cell G3	10^{-19}	10^{-16}	Single acc.	5×10^{16}	99.9
Cell G4	10^{-19}	10^{-16}	Single acc.	5×10^{16}	99
Cell G5	10^{-19}	10^{-16}	Single acc.	5×10^{16}	90

Chapter 6

Results and Discussion

This chapter contains the results obtained from all the simulations done in this work, along with discussions of these results.

The sections of this chapter provide results of the simulations presented in corresponding sections of Chapter 5. Sections 6.1 and 6.2 present the performance of the impurity free cell and the reference cell of sections 5.2 and 5.3, respectively. Section 6.3 evaluate the possibilities and limitation of SCAPS as a tool for IPV solar cell simulations, in light of the results of the simulations listed in section 5.4. Finally, section 6.4 deals with the influence of design and impurity parameters on cell performance, that is, the results of the simulations listed in section 5.5.

Each (sub)section opens with a description of the simulations behind the results of that (sub)section. This serves as a motivation for the simulations as well as making it easier to read the current chapter without having to go back to Chapter 5, where the details of the simulations are listed. When needed, the values of the parameters of all the cells discussed in this chapter are found in the appropriate section of Chapter 5. After the introduction in each (sub)section, the results of that (sub)section are presented, followed by a discussion of these results.

The results are presented in various forms. Values of the performance parameters cell efficiency (η), open circuit voltage (V_{OC}), short circuit current density (J_{SC}) and fill factor (FF) are presented in tables, or graphically as a function of design or impurity parameters. The rest of the results are presented graphically, in the form of current density-voltage characteristics (IV curves), quantum efficiency (QE) curves, energy band diagrams, generation and recombination rates and probabilities of impurities to be occupied by electrons (occupation probability).

6.1 Performance of the Impurity Free Cells

The purpose of the impurity free cells (Cells A1 and A2) defined in section 5.2 of Chapter 5 is to compare them to subsequent cells, in order to evaluate whether the introduction of impurities can have a positive influence on cell performance. The most suitable results for such a comparison are IV curves, QE curves and performance parameters.

Cells A1 and A2 are in this section also compared to the the world record single-junction (WR SJ) solar cell. Comparing the simulated cells to an actual one makes it possible to evaluate how realistic the simulated cells are.

Results

Figure 6.1 shows IV curves and QE curves of the impurity free cells (Cells A1 and A2). The solar cell performance parameters of Cell A1 and A2 are listed in Table 6.1. Listed in this table are also the performance parameters of the WR SJ GaAs cell, measured under a one-sun AM1.5 spectrum with an intensity of 1000 W/m^2 at 25 °C [31]. In ref. [31], Green et al. provides an overview of the state of the art solar cells in various categories. The cell included here was made by Alta Devices, and is presented by Kayes et al.in ref. [32]. Specific details of the structure of the PV device is not given in ref. [32], but since both the WR SJ cell and the cells in this theses are single junction, it is assumed to be a good cell to use for comparison.

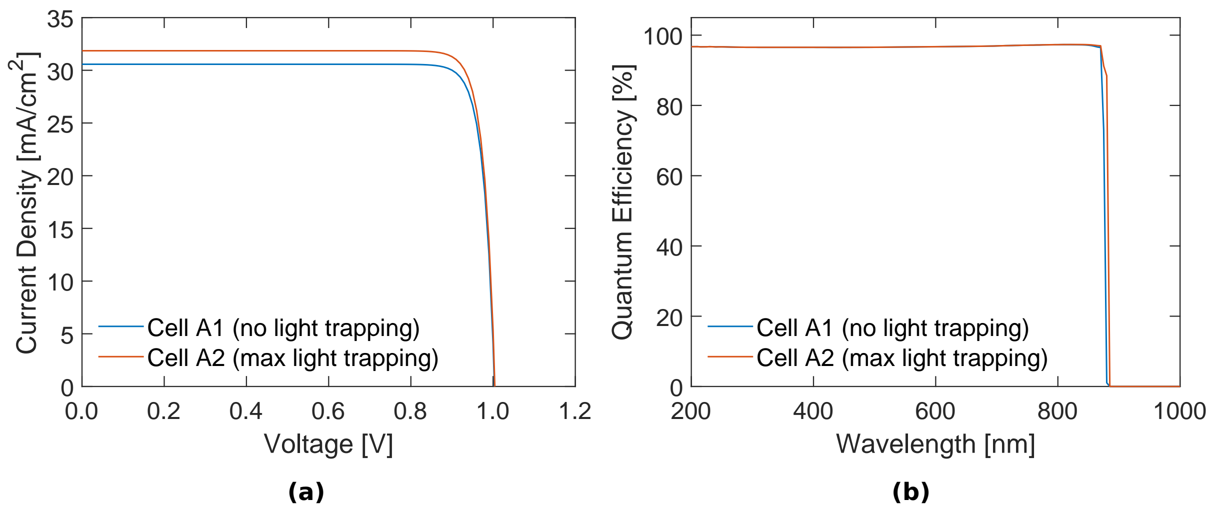

Figure 6.1: (a) IV curves and **(b)** QE curves of Cells A1 and A2.

Table 6.1: Solar cell performance parameters of Cell A1 and A2 as well as of the world record single-junction GaAs cell [31] and the attempt to imitate the world record single-junction cell, namely Cell A3.

Cell	η [%]	V_{OC} [V]	J_{SC} [mA/cm^2]	FF [%]
Cell A1	27.1	1.00	30.6	88.2
Cell A2	28.2	1.00	31.9	88.2
WR SJ GaAs cell [31]	29.1 ± 0.6	1.13	29.8	86.7

From the IV curves in Figure 6.1(a), Cell A2 is seen to have a higher current density than Cell A1 over the entire voltage interval. Besides that, the IV curves are similar. This is confirmed by the performance parameters in Table 6.1, where J_{SC} is 1.3 mA/cm^2 higher for Cell A2 than for Cell A1, while V_{OC} and FF are equal for both cells. The efficiency is therefore higher for Cell A2 than for A1.

The WR SJ cell has a somewhat lower J_{SC} than Cells A1 and A2, but a higher V_{OC}, and thereby a higher efficiency than Cells A1 and A2.

The QE curves in Figure 6.1(b) are rather similar. They both have a steady quantum efficiency of around 97 % from 200 nm to around the band gap of 1.42 eV (873 nm), where they drop to zero. Over a very short wavelength interval around the band gap, Cell A2 has a significantly higher quantum efficiency than Cell A1.

Discussion

The light trapping in Cell A2 allows the incoming light to travel back and forth between the front and back contacts, instead of passing through the cell just once. From Figure 5.2 in Chapter 5 it is seen that that the absorption coefficient is higher for the shorter wavelengths and lower for the longer ones. Thus, for the short wavelength photons, the cell thickness of 6 μm is enough to absorb virtually all of the photons, and the light trapping makes little difference. The long wavelength photons, on the other hand, benefit from the extended path length offered by the light trapping. If therefore makes sense that the longest of the absorbed wavelengths have a higher QE in a cell with light trapping.

Cell A2's high QE around the band gap can explain an increase in J_{SC} when including light trapping, as more of the incoming photons give rise to an electron in the external circuit. Still, the increase of 1.3 mA/cm^2 is maybe larger than expected from the narrow interval in which the QE curves differ. The contribution to the current from the photons with wavelengths corresponding to the band gap to the current is, however, significant. From Figure 5.1 in Chapter 5, it is seen that the intensity of the incoming light is rather high at around the band gap of GaAs. Dividing the high intensity with the low energy of the photons around the band gap results in a high number of photons incident on the cell in this wavelength interval. This means that the difference in QE at these wavelengths yields a big difference in the current density.

The parameters of Cell A1 and A2 are partly chosen to keep the cells simple, and thereby ease the understanding of the influence of parameter variation in later simulations. It is still useful to know something about how valid these simplifications are in order to evaluate the potential for efficient IPV cells.

Regarding the open circuit voltage of the WR SJ cell, Kayes et al. state that the "high V_{OC} results from a device with very low dark current [. . .]" [32, p. 5]. This is in agreement with solar cell theory [11, pp. 93-95], from which we know that lower recombination rates increases V_{OC}. The only recombination mechanisms present in Cells A1 and A2 are radiative recombination ($K_{rad} = 7.2 \times 10^{-10}$ cm^3/s) and recombination at the contacts/surfaces ($S_n = S_p = 1 \times 10^4$ cm/s for both contacts). Thus, these rates in Cells A1 and A2 are not unrealistic, and might even be somewhat exaggerated compared to what is achievable for actual cells. As discussed by Kayes et al. [32], photon recycling is an efficient way of reducing recombination, as electron-hole pairs that recombine radiatively emit photons that can be reabsorbed in the semiconductor material. Since photon recycling is not included in SCAPS, one could argue that the bulk recombination is overestimated by SCAPS.

The higher J_{SC} of Cells A1 and A2 compared to the WR SJ cell might be due to different reflection at the front contact (Cell A2's J_{SC} is additionally increased by the light trapping, as previously discussed). Cells A1 and A2 have 100 % transmission at the front surface, giving a QE close to unity over the entire wavelength interval up until the band gap (Figure 6.1(b)). The reflection of the WR SJ cell is not known, but its QE curve (not shown here) starts at zero at around 300 nm and increases rapidly up to 500 nm [32, p. 6]. This is what one would expect if short wavelength photons are reflected at the front surface. The reflection at the front surface would naturally lead to a lower J_{SC} .

The fact that the fill factor is lower for the WR SJ cell than for Cells A1 and A2 could be due to the lack of series resistance in Cells A1 and A2. From theory, an increase in series resistance is expected to reduce *FF* [11, pp. 96-98]. This is also pointed out by Kayes et al. [32].

In the big picture, the performance of the WR SJ cell is not too different from that of Cells A1 and A2. The similarity means that Cell A1 and A2 can act as reasonable cells for comparison with the other cells simulated in the current work. The high V_{OC} of the WR SJ

cell implies that the recombination rates of Cells A1 and A2 are not unrealistic, and that even lower rates are possible to obtain for actual cells. The lack of series resistance in Cell A1, on the other hand, seems somewhat unrealistic. So does the 100 % transmission of the front contact in Cell A1. Although not tested here, it seems a reasonable assumption that the ideal light trapping of Cell A2 is unrealistic. It is idealized to act as an upper limit to what efficient light trapping can achieve.

6.2 Performance of the Reference Cell

The results of the simulations of the reference cell, Cell B1, is in this section presented and discussed. This is done to obtain an understanding of the cell that acts as a starting point for subsequent cells. Part of the purpose is also to present the range of different results types relevant for the following sections.

Results

Figure 6.2 shows the IV and QE curves of Cell B1 (reference cell). The QE curve is at 0 V. The performance parameters of Cell B1 are given in Table 6.2. Cell B1 has a relatively high J_{SC} , but a much lower V_{OC} , *FF* and η than Cell A1. The QE of Cell B1 is high up until around the main band gap of GaAs at 1.42 eV (873 nm). From this point the QE decreases in steps at wavelengths corresponding quite well with the two sub band gaps of 0.95 eV (1305 nm) and 0.47 eV (2638 nm) created by the impurity level.

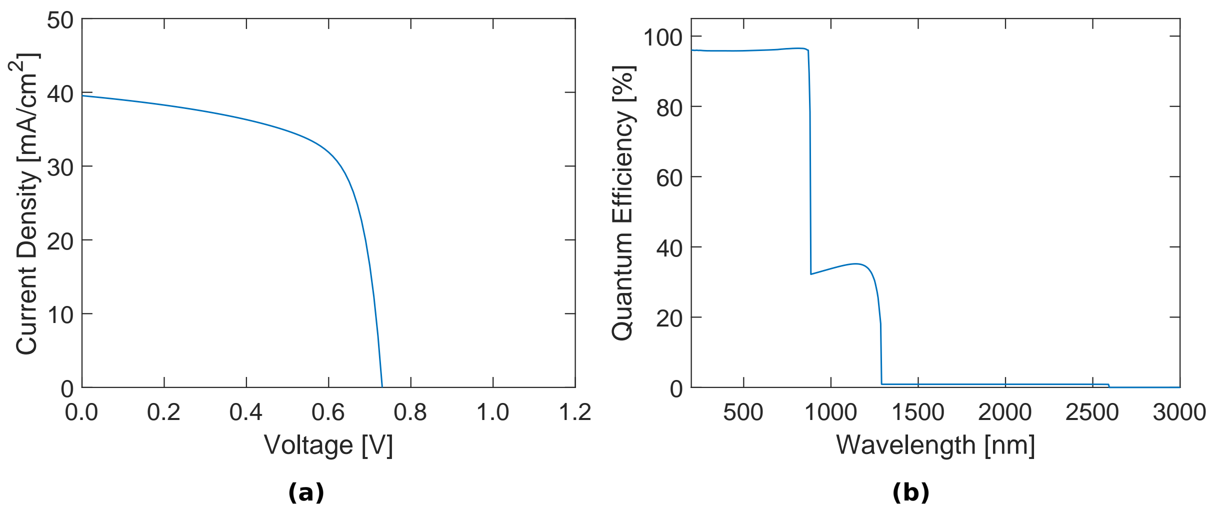

Figure 6.2: (a) IV curve and **(b)** QE curve at 0 V for Cell B1 (reference cell).

Table 6.2: Performance parameters of Cell B1 (reference cell).

Cell	η [%]	V_{OC} [V]	J_{SC} [mA/cm^2]	*FF* [%]
Cell B1	19.1	0.73	39.5	66.2

Figure 6.3(a) shows a screenshot of the structure of Cell B1 taken from the SCAPS user interface. The p-layer is red and the n-layer is blue. The green layer is the IPV-layer. This is the layer in which the deep level impurities are introduced. It contains no shallow dopant atoms, and is therefore shown as green in SCAPS. Figures 6.3(b), 6.3(c) and 6.3(d) show energy band diagrams for Cell B1 at 0 V, V_M and V_{OC}, respectively.

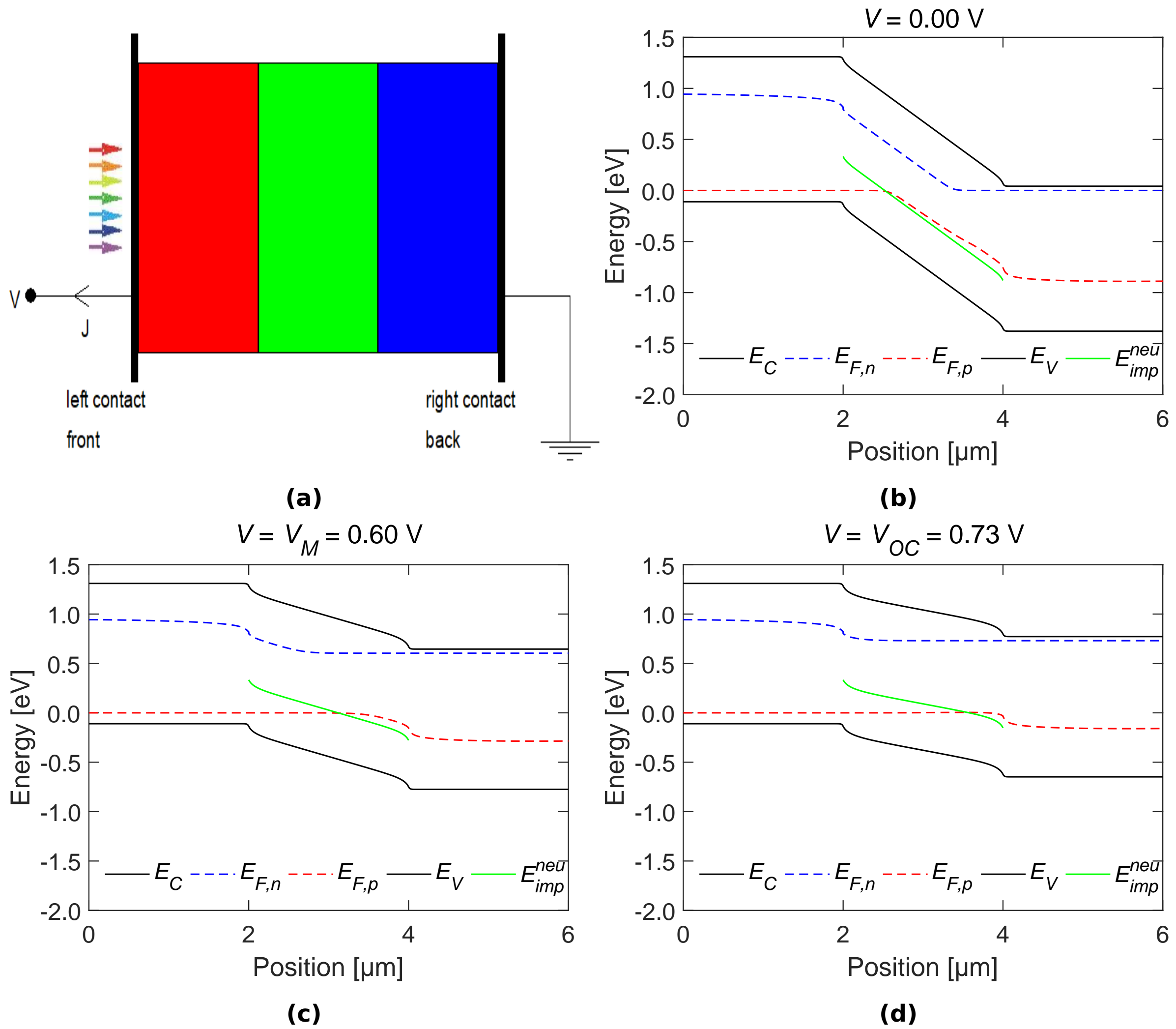

Figure 6.3: (a) Screenshot of the structure of Cell B1 (reference cell), taken from the SCAPS user interface. The p-layer is red, the n-layer blue and the IPV-layer is green. The multi-coloured arrows illustrate the incoming light. Energy band diagrams for Cell B1 at **(b)** 0 V, **(c)** V_M and **(d)** V_{OC} .

Figure 6.4 shows the impurity level's probability of occupation with electrons at 0 V, V_M and V_{OC}.

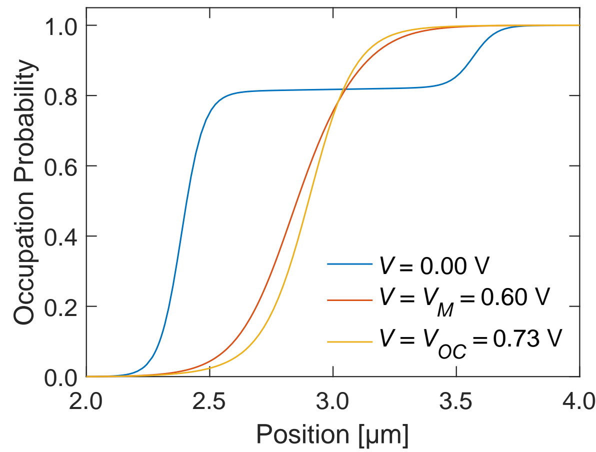

Figure 6.4: Probability of occupation with electron for the impurity level in the IPV-layer in Cell B1 (reference cell) at 0 V, V_M and V_{OC} .

Figures 6.5 – 6.10 show different generation, recombination, emission and capture rates of Cell B1 as a function of position in the cell. Only the part of the cell in which the displayed rates are present and non-zero is shown. For example, as the SRH recombination rate is only present in the IPV-layer, this rate is only plotted between 2 µm and 4 µm.

The optical generation rate, G^{op}, is in Figure 6.5 seen to gradually decline further into the cell. In the same figure, the radiative recombination rate, R^{op}, is seen to be drastically lower in the IPV-layer (between 2 µm and 4 µm) than in the rest of the cell.

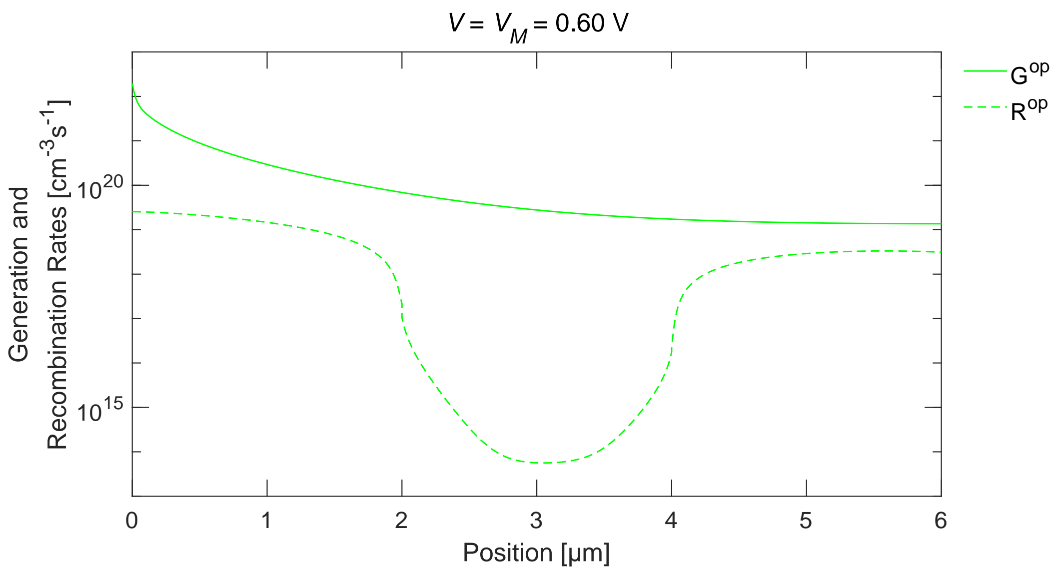

Figure 6.5: Optical generation and recombination of Cell B1 (reference cell) at V_M.

The SRH recombination rate at 0 V, U_{SRH}^{ipv1}, is plotted on a linear scale in Figure 6.6(a). The same rate is plotted logarithmically in Figure 6.6(b). Since U_{SRH}^{ipv1} is negative in some cases (meaning that the IPV effect is greater than the recombination associated with the impurities), is was challenging to plot this rate on a logaritmic scale. In order to include both positive and negatvie values of the U_{SRH}^{ipv1}-curve in the same logarithmic plot, the absolute

value was plotted. Then, two vertical dashed lines were included to indicate the interval in which U_{SRH}^{ipv1} was negative before taking the absolute value. That is, U_{SRH}^{ipv1} is negative between the dashed vertical lines. In the rest of the thesis, only logarithmic plots are presented for U_{SRH}^{ipv1}. Whenever part of the U_{SRH}^{ipv1}-curve is negative, the absolute value is plotted and the dashed vertical lines are included in the same manner as described here.

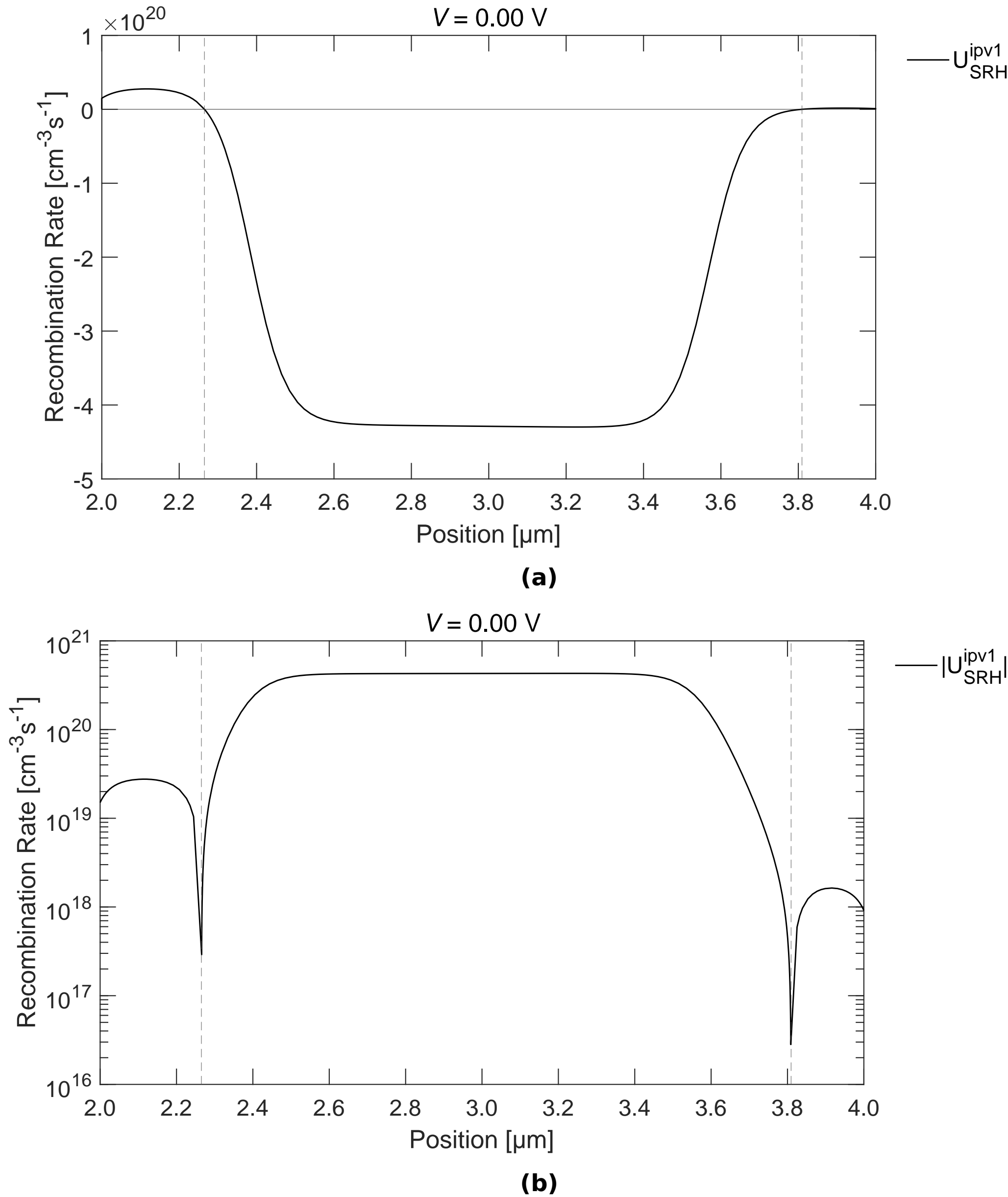

Figure 6.6: Two ways of plotting the SRH recombination rate of Cell B1 (reference cell) at 0 V. **(a)** Linear plot of the SRH recombination rate and **(b)** logarithmic plot of the absolute value of the SRH recombination rate. In order to plot both positive and negative values in the same logarithmic plot, the absolute value is plotted. Between the dashed vertical lines, the SRH recombination rate is negative.

The SRH recombination rate is plotted at V_M and V_{OC} in Figures 6.7 and 6.8, respectively. As the voltage increases from 0 V (in Figure 6.6) to V_M, the region in which U_{SRH}^{ipv1} is negative gets more narrow. At V_{OC}, U_{SRH}^{ipv1} is positive at all positions in the cell.

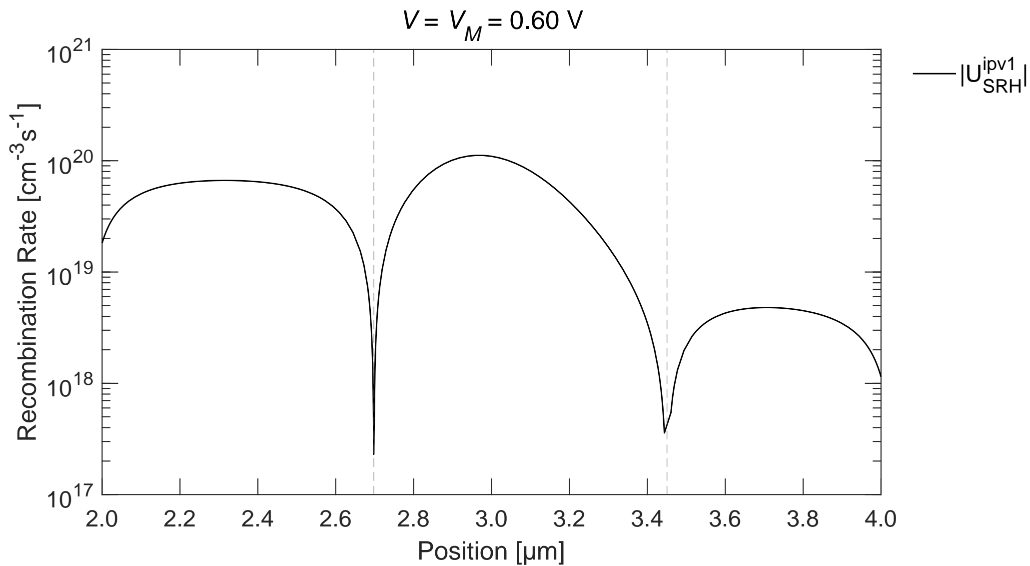

Figure 6.7: Absolute value of the SRH recombination rate of Cell B1 at V_M.

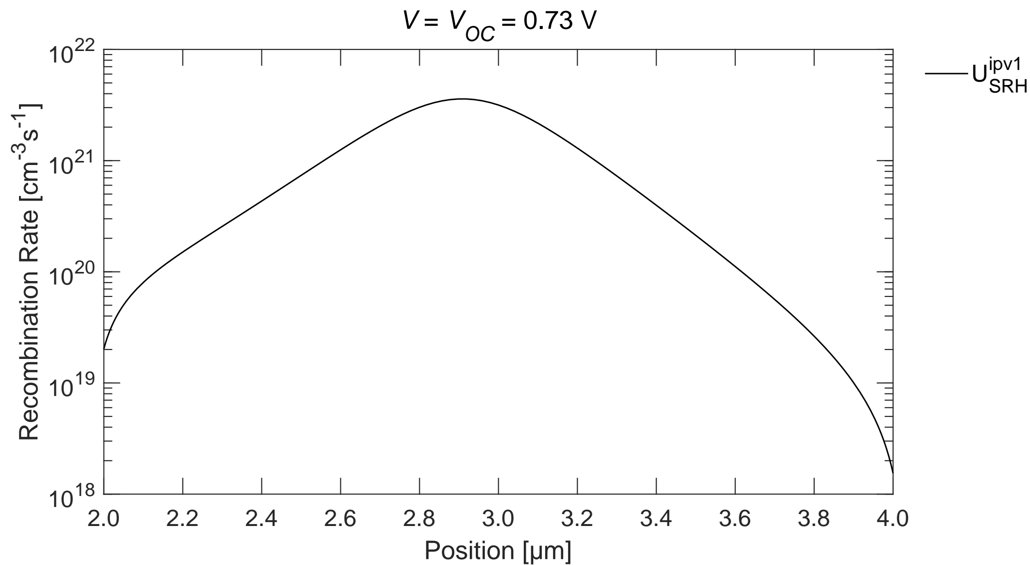

Figure 6.8: The SRH recombination rate of Cell B1 at V_{OC} .

Figure 6.9 shows thermal and optical capture and emission rates for electrons and holes at V_M. The thermal capture rates and the optical emission rates are plotted again in Figure 6.10, along with the SRH recombination rate.

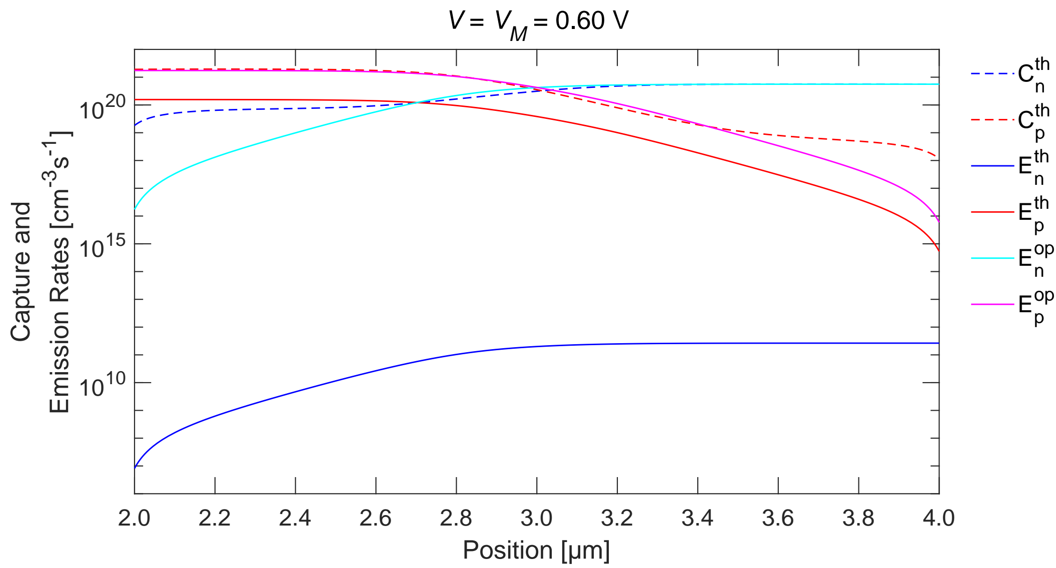

Figure 6.9: Thermal and optical capture and emission rates for electrons and holes in Cell B1 at V_M.

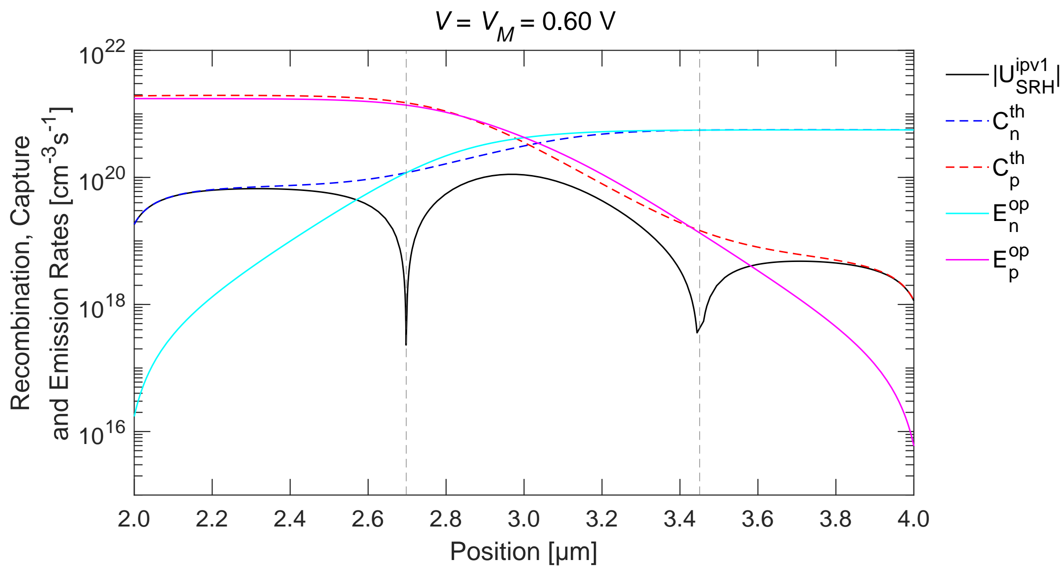

Figure 6.10: Absolute value of SRH recombination rate as well as thermal capture rates and optical emission rates for electrons and holes in Cell B1 at V_M.

Discussion

The bending of the energy band diagrams in Figure 6.3 decrease as the applied voltage increases. This is as expected from the theory in Chapter 2. The bending of the quasi-Fermi levels also decrease with increasing applied voltage. From equations (2.20) and (2.21) in Chapter 2 we know that the current density contribution from either charge carrier is the product of its concentration, mobility and the gradient of the appropriate quasi-Fermi level. Combined with the fact that the current density through the cell decreases when the applied voltage increases, it therefore makes sense that the quasi-Fermi levels vary less across the cell thickness at V_M and V_{OC} than at 0 V.

The sum of the current density contributions from electrons and holes must be constant throughout the cell thickness. In the p- and n-layers, the gradient of the majority carrier quasi-Fermi levels is small, but the majority carrier density is of course high. For the minority carriers, the quasi-Fermi levels have a larger gradient, but the carrier concentration is low. In the depletion region, the gradients of both quasi-Fermi levels have their maximum value, but the concentrations of both carriers are low. All in all, it seems reasonable that the total current density is constant.

Although not shown here, the electron current density accounts for nearly all of the current density in the n-layer. This might not be surprising, as the concentration of electrons is much higher than that of holes in this region. However, for all voltages shown in Figure 6.3, $E_{F,n}$ is seemingly completely flat in the n-layer, which would mean that J_n is zero. Due to the high concentration of electrons, only a very small gradient in $E_{F,n}$ is required to account for the current density. Using the band diagram at V_M (Figure 6.3(c) as an example, $E_{F,n}$ decreases quite linearly by an amount of 8×10^{-8} eV between 4 µm and 6 µm. This means that the gradient of $E_{F,n}$ is -4×10^{-8} eV/µm = -4×10^{-4} eV/cm = 6.408×10^{-23} J/cm. By using equation (2.20), multiplying this by the electron mobility and the electron concentration gives an electron current density of -32 mA/cm^2. The coincides well with the actual total current density of 31.7 mA/cm^2. The difference in sign is due to the convention chosen for the IV curve and the performance parameters.

The occupation of the impurity level (Figure 6.4) is strongly related the to $E_{F,p}$. By comparing the occupation probabilities with the appropriate energy band diagram in Figure 6.3, it is seen that the lower $E_{F,p}$ is compared to the impurity level, the smaller the occupation probability of the impurity is.

The high J_{SC} of Cell B1 (Figure 6.2(a) and Table 6.2) must be due to the IPV effect. The downside of introducing deep level impurities is the SRH recombination they enable. From the low V_{OC} and η, it can be concluded that the benefit of the IPV effect does not outweigh the effect of increased recombination for this cell. The SRH recombination rate of Cell B1 at V_M (Figure 6.7), is positive only in a narrow region of the cell, thus not generation enough extra charge carriers to make up for the voltage loss associated with the introduction of the impurities. At V_{OC} (Figure 6.8), there is no net positive contribution from the impurities at any position in the cell.

The QE curve in Figure 6.2(b) shows how photons with energies lower than the main band gap are absorbed due to the IPV effect. QE curves will be discussed more in subsequent sections.

The gradual decrease of the optical generation rate in Figure 6.5 is expected, as most of the incident radiation is absorbed near the surface. The radiative recombination rate in Figure 6.5 requires more discussion. In SCAPS, the radiative recombination is calculated at $R^{op} = K_{rad}\left(np - n_i^2\right)$ [20, p. 33], where K_{rad} is the radiative recombination coefficient. Since K_{rad} has the same value throughout the cell, the large difference between R^{op} in the IPV-layer and the n- and p-layers must be due to a large difference in excess carrier

concentration. This makes sense as we know that the charge carrier concentration is lower in the depletion region than outside of it.

It is interesting to note that this large variation in R^{op} does not occur at V_M for Cell A2 (not shown). In Cell A2, there are no impurities in the middle layer, and thereby no SRH recombination. At V_M, the SRH recombination rate in the IPV-layer of Cell B1 efficiently reduces the charge carrier concentrations, leading to a lower radiative recombination rate. The lack of SRH recombination in the middle layer of Cell A2 means higher charge carrier concentrations than in Cell B1 and therefore a higher radiative recombination rate.

In Figure 6.9 it is seen that the thermal emission of either charge carrier is significantly lower than the optical emission of the same charge carrier. Especially the E_n^{th} is of insignificant magnitude. It is not surprising that few charge carriers can overcome the sub band gaps of 0.47 eV and 0.95 eV by means of the thermal energy at room temperature. The much higher optical emission rates can indicate a potential for the IPV effect. These rates must of course be greater than the thermal capture rates in order to achieve a net negative SRH recombination rate. Disregarding the thermal emission rates, Figure 6.10 shows that the limits to the region of negative net SRH recombination rate (shown by the vertical dashed curves) occur at the intersection of E_n^{op} and C_n^{th} and at the intersection of E_p^{op} and C_p^{th}. Finally, it is worth noting the similar shapes of the optical and thermal emission rate of either charge carrier (Figure 6.9). This might be a result of both emission rate depending on quantities such as the occupation proability. In fact, on a linear scale (not shown), the shape of the electron emission rate curves is similar to the shape of the occupation probability curve in Figure 6.4. The shape of the hole emission rate curves resembles the shape of one minus the occupation probability curve. This is as it should be, since a high occupation of the impurity level is beneficial for electron emission, but disadvantageous to hole emission.

6.3 Evaluation of SCAPS as a Tool for Simulating IPV Solar Cells

6.3.1 SRH Recombination in SCAPS

In order to understand how the SRH recombination rate is calculated in SCAPS, simulations of generation and recombination rates were done on Cell B1 and cell B2. From the results, three different rates were plotted: The net rate of electrons going from the conduction band to the impurity (U_{ci}), the net rate of electrons going from the impurity to the valence band (U_{iv}) and the SHR recombination rate (U_{SRH} (or U_{SRH}^{ipv1} when the IPV effect is included)).

The simulations described in the previous paragraph were performed using SCAPS version 3.3.09. As evident in the following, these simulations yielded unexpected results that turned out to be caused by a minor bug in the SCAPS software. The bug was reported to and corrected by SCAPS developer Honorary Professor Marc Burgelman (personal communication, e-mail, 19.08.21). After installing the newest update of SCAPS 3.3.10, the simulations described in the previous paragraph were repeated. All other simulations in this thesis (both those preceding this section and those following it) were also performed using the latest update of SCAPS 3.3.10. More details and the answer from Marc Burgelman are found in subsection 5.1.1 of Chapter 5 and in section C.3 of Appendix C (the correction of the bug is treated in the end of C.3).

Results

Figure 6.11 shows the absolute value of U_{ci}, U_{iv} and U_{SRH}^{ipv1} for Cell B1 (reference cell) at 0 V, calculated using SCAPS version 3.3.09. The rates U_{ci} and U_{SRH}^{ipv1} overlap. The rate U_{iv}, however, does not overlap with the two others, as it is expected to.

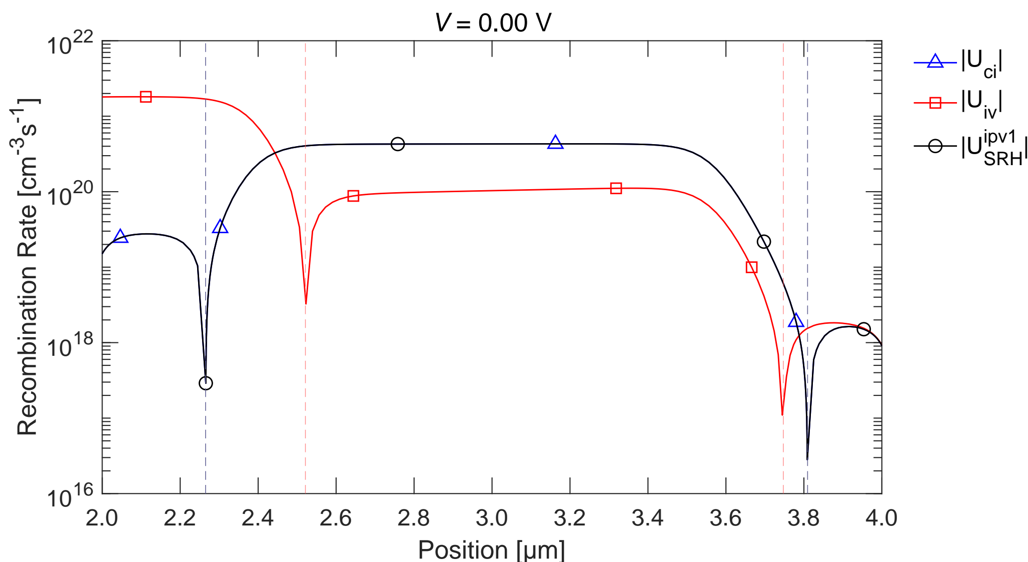

Figure 6.11: The absolute value of U_{ci}, U_{iv} and U_{SRH}^{ipv1} for Cell B1 (reference cell) at 0 V, calculated using SCAPS version 3.3.09.

In Figure 6.12, U_{ci}, U_{iv} and U_{SRH} are shown for Cell B2 at 0 V. This cell is identical to the reference cell, but with the IPV effect disabled. The rates in Figure 6.12 are also calculated using SCAPS version 3.3.09, but for this cell all three curves overlap.

Figure 6.13 shows the absolute value of U_{ci}, U_{iv} and U_{SRH}^{ipv1} for Cell B1 (reference cell) at 0 V, calculated using the latest update of SCAPS version 3.3.10. The curves for U_{ci} and U_{SRH}^{ipv1}

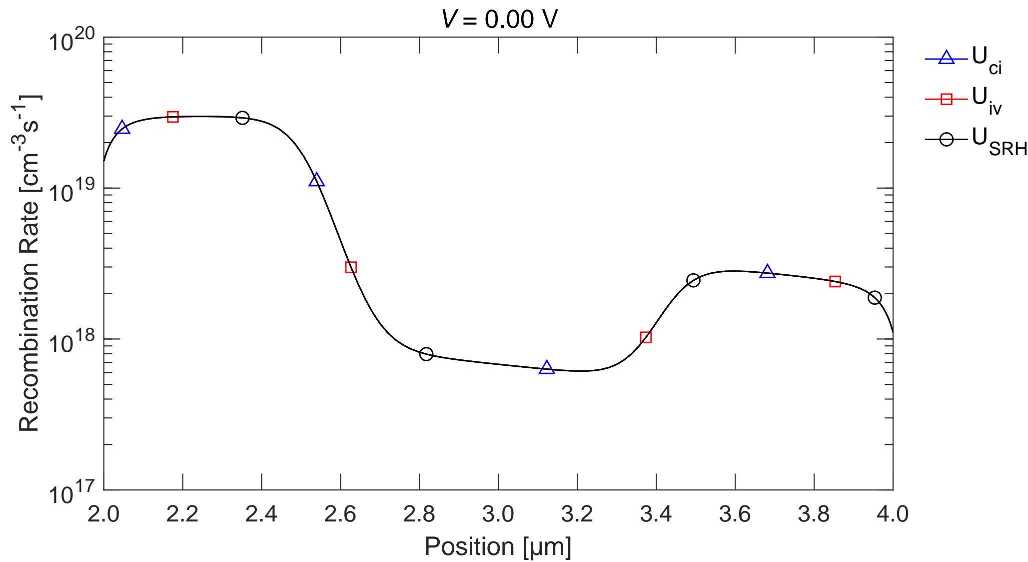

Figure 6.12: U_{ci}, U_{iv} and U_{SRH} for Cell B2 (identical to the reference cell, but with the IPV effect disabled) at 0 V, calculated using SCAPS version 3.3.09.

are identical to the corresponding curves in Figure 6.11. Now, also the curve for U_{iv} overlap with the two others.

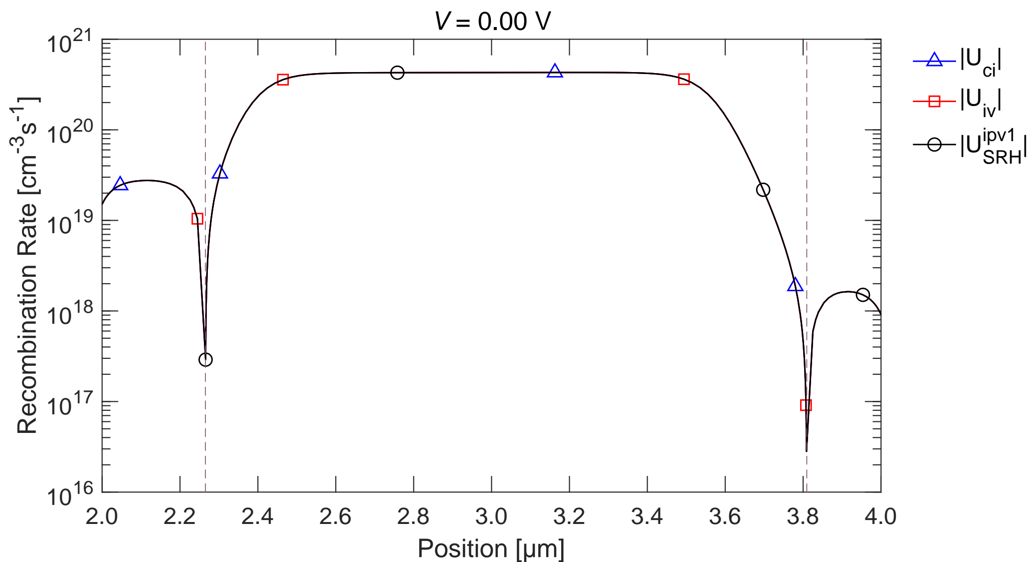

Figure 6.13: The absolute value of U_{ci}, U_{iv} and U_{SRH}^{ipv1} for Cell B1 (reference cell) at 0 V, calculated using the latest update of SCAPS version 3.3.10.

U_{ci}, U_{iv} and U_{SRH} for Cell B2, calculated using the latest update of SCAPS 3.3.10 were identical to those calculated using SCAPS 3.3.09 (shown in Figure 6.12).

Discussion

From equations (3.17) in Chapter 3, U_{ci}, U_{iv} and U_{SRH} (or U_{SRH}^{ipv1}) are expected to be equal. This is also true when the IPV effect is enabled. When using SCAPS 3.3.09, this is not the case for Cell B1 (Figure 6.11). This led to the suspicion that there was a bug in the SCAPS

software. With Cell B2, when the IPV effect is disabled, the curves overlap as expected. The bug would therefore likely have something to do with the implementation of the IPV effect in SCAPS.

The bug turned out to be associated with the presentation of the hole optical emission rate, E_p^{op}. The bug did not cause any errors in other calculations in SCAPS; it only affected E_p^{op} (and therefore also U_{iv}). See section C.3 in Appendix C for more details.

After the bug was corrected, U_{ci}, U_{iv} and U_{SRH} (or U_{SRH}^{ipv1}) overlap for both Cell B1 and Cell B2, as expected.

6.3.2 *Implementation of the Lucovsky Model for Photo-Ionization Cross Section*

The photo-ionization cross section of electrons (σ_n^{op}) and holes (σ_p^{op}) can in SCAPS be calculated internally in SCAPS or by the input of a files containing σ_n^{op} and σ_p^{op} as a function of wavelength. The internal calculation uses the Lucovsky model [4] in the formulation of Güttler and Queisser [5] (see section 4.5 of Chapter 4 and section C.2 of Appendix C for more information). To test my understanding of the implementation of the Lucovsky model in SCAPS, IV and QE simulations were run on Cell B1 (where the internal Lucovsky model in SCAPS is used) and on Cell C1, a cell identical to Cell B1, except with the photo-ionization cross sections calculated externally and input as files. In Cell C1, σ_n^{op} and σ_p^{op} were calculated using the same model and parameter values as in Cell B1, but implemented with a MATLAB function that generates files to input in SCAPS. The photo-ionization cross sections of Cell C1 are shown in Figure 6.14. The cut-off at 3 eV for both electrons and holes gives the non-zero onset at 413 nm. The MATLAB function used to calculate the photo-ionization cross sections of Cell C1 is given in Appendix B.

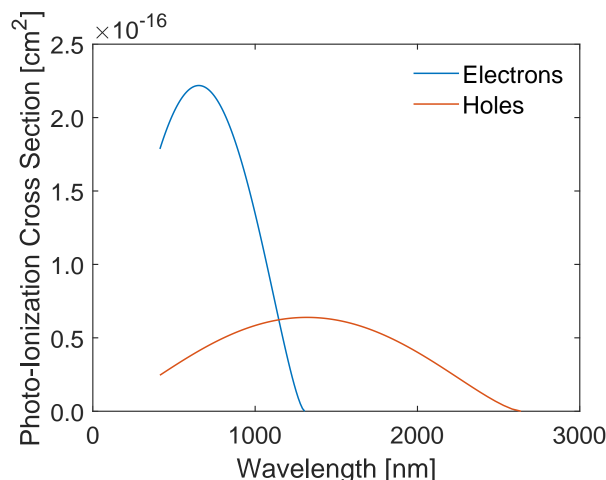

Figure 6.14: Photo-ionization cross section for electrons and holes externally calculated by use of the Lucovsky model [4] for Cell C1. The non-zero onset is due to the cut-off energy at 3 eV (413 nm) for both electrons and holes.

Results

Figure 6.15 shows the IV and QE curves of Cell B1 (with the photo-ionization cross sections calculated internally in SCAPS) and Cell C1 (with the photo-ionization cross sections calculated externally). The IV curves overlap more or less completely. The QE curves overlap well, but on a logarithmic plot (not shown) there is some difference in QE for wavelengths longer than about 1300 nm.

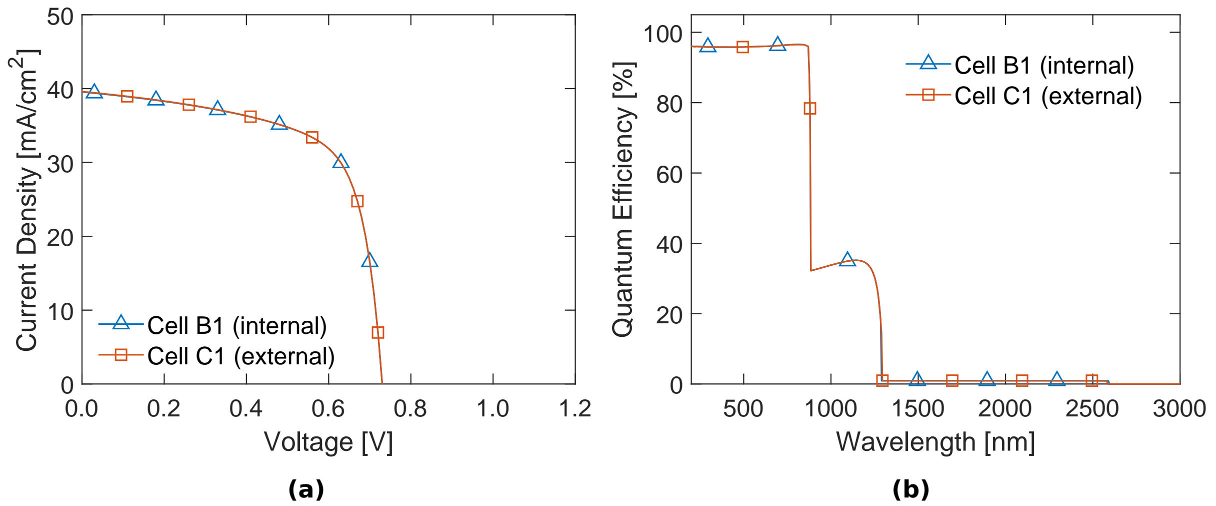

Figure 6.15: (a) IV curves and **(b)** QE curves of Cells B1 (internally calculated photo-ionization cross section) and C1 (externally calculated photo-ionization cross section).

Discussion

The most important finding of the simulations investigating the implementation of the Lucovsky model in SCAPS is that the differences between the IV and QE curves resulting from the two implementations are small. It is difficult to say what is causing the minor difference in QE, but the difference is too small to carry any relevance for the current work. For practical reasons, the internal Lucovsky model will be used in further simulations. Nevertheless, the plots of the photo-ionization cross sections provided by the external approach will be used to visualize how the cross sections vary when the parameters of the Lucovsky model are varied.

6.3.3 Evaluation

Through correspondence with Marc Burgelman (see Appendix C), the details of how the IPV effect is implemented in SCAPS are explained. The results in subsections 6.3.1 and 6.3.2 have increased the understanding of how SCAPS calculates the SRH recombination rate and implements the Lucovsky model. By using the software for the other simulations in this project, it is found to be a suitable tool for simulation of IPV solar cells. SCAPS does, however, not include the mechanism of photon recycling, neither of photons re-emitted band-to-band nor photons emitted when charge carriers are captured by the impurity. That is, R_{btb}^{op}, C_n^{op} and C_p^{op} are not included in SCAPS. The energy given off through band-to-band recombination capture by the impurity is simply view as lost in SCAPS. Had it been included, some of this energy might have been reabsorbed. This means that SCAPS might underestimate the performance of the cells it simulates. It could also be that the effect of including photon recycling is small. Quantifying the amount of recombination and capture processes that are optical is an interesting task, but beyond the scope of this thesis.

Besides that, I have experienced a few cases in which SCAPS behaves unexpectedly. For example, in special cases the software might be closed without warning, potentially leaving unsaved results behind. It is, however, possible to avoid these cases, so they are not a big problem. Moreover, (except for the bug treated in subsection 6.3.1), I have not encountered situations where I suspect that the calculations are wrong. All in all, I find SCAPS to be a useful software suitable for simulations of IPV solar cells.

6.4 Influence of Design and Material Parameters on Cell Performance

The influence on cell performance of varying the following parameters is studied in this section: The photo-ionization cross sections of the impurities (subsection 6.4.1), thermal capture cross sections of the impurities (subsection 6.4.2), type of the impurities and shallow background doping (subsection 6.4.3) and the design parameters internal front contact/surface reflection (subsection 6.4.4).

Although simulation allows one to freely vary all these parameters, one should keep in mind which parameters are easily varied also in actual cells and which are not. The impurity density is for instance possible to control for real cells, whereas the refractive index is perhaps not so easily adjusted. It is still interesting to study the influence of all these parameters on the cell performance. The motivation for studying the different parameters depend on the nature of the parameter. Some might provide suggestions for efficient cell design, some can help evaluate the suitability of GaAs as an IPV cell material and some might say something about which elements could work well as impurities. In addition, the study of all the parameters will increase the understanding of IPV cells and which parameters are the most influential and thus the most important to control when making actual cells.

Cell B1 (reference cell) is used for comparison throughout this section. Its function is as a starting point from which one parameter at a time is varied. Any improvement over the reference cell performance brings us one step closer to creating IPV cells that are more efficient than the impurity free cells. So although many cells in this section perform worse that the impurity free cells, it is interesting to study how to adjust each parameter to improve IPV cell performance. Then as a final conclusion, it is possible to say if any combination of parameter values can outperform the impurity free cells.

6.4.1 Photo-Ionization Cross Section Parameters

Six parameters determine the photo-ionization cross sections: The impurity energy level (E_{imp}), the band gap of the host material (E_g), the refractive index (n_r), the effective field ratio (E_{eff}/E_0), the effective charge carrier mass (m^*) and the cut-off energies (E^{cut}). The band gap and the impurity level affect the photo-ionization cross sections by determining the ionization energy of the impurity. They are not varied in this thesis, but remain at E_g = 1.42 eV and E_{imp} = 0.47 eV for all cells.

The the influence of n_r, E_{eff}/E_0 and m^* on the photo-ionization cross section is readily seen in the Lucovsky equation (equation (3.23)). The photo-ionization cross section increases with low n_r and m^* and with high E_{eff}/E_0. To study the influence of these parameters, they were in Cell D1 set to $n_r = 1$, $E_{eff}/E_0 = 10$, $m_n^*/m_0 = 6.7 \times 10^{-3}$ and $m_p^*/m_0 = 4.7 \times 10^{-2}$. This causes σ_n^{op} and σ_p^{op} in Cell D1 to increase for all wavelengths by a factor of 825 compared to σ_n^{op} and σ_p^{op} in Cell B1. The shapes of the curves for σ_n^{op} and σ_p^{op} are equal for both cells. The photo-ionization cross sections of Cell D1 are shown in Figure 6.16(a) (calculated in MATLAB). Although the values in Cell D1 for these parameters are unrealistic, Cell D1 is useful for the discussion of the influence of the magnitude of σ_n^{op} and σ_p^{op} on cell performance.

In Cells D2, D3 and D4, the E^{cut} of electrons (E_n^{cut}) and holes (E_p^{cut}) were varied to test their influence on cell performance. The photo-ionization cross sections of these cells are shown in Figure 6.16, calculated according to the Lucovsky model using MATLAB. The cut-off energies are indicated by the vertical lines. For Cell D2 (Figure 6.16(b)), E_n^{cut} and E_p^{cut}

are reduced to 1.42 eV, so that σ_n^{op} and σ_p^{op} are not in competition with the band to band absorption. For Cell D3, only the E_p^{cut} is changed from the reference cell value. It is set to 0.95 eV, avoiding competition between σ_n^{op} and σ_p^{op}. Finally, in Cell D4 E_n^{cut} and E_p^{cut} are set so 1.42 eV and 0.95 eV, respectively, thus avoiding all competition between the three absorption mechanisms.

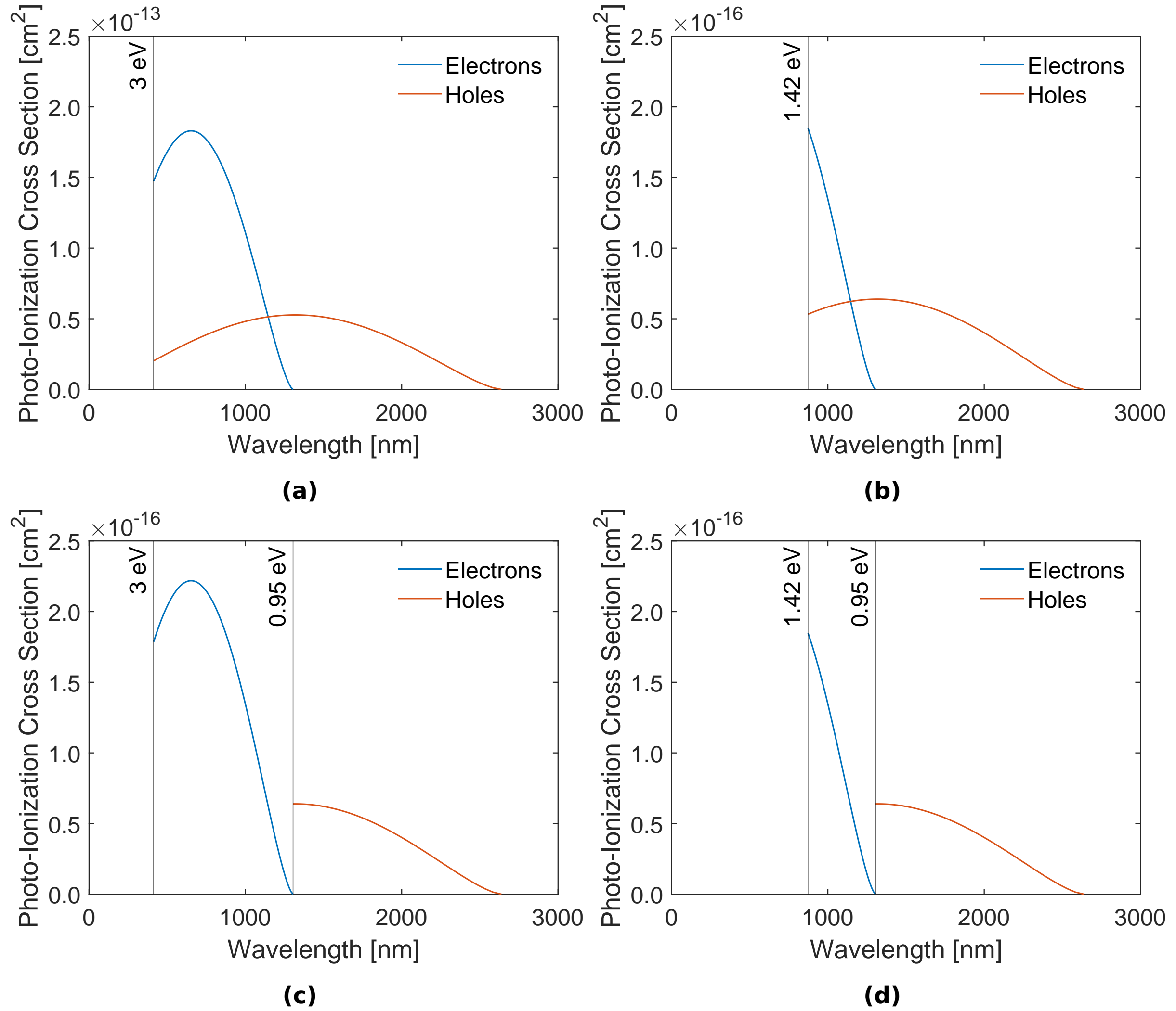

Figure 6.16: Photo-ionization cross sections calculated according to the Lucovsky model for **(a)** Cell D1, **(b)** Cell D2, **(c)** Cell D3 and **(d)** Cell D4. The vertical lines indicate the cut-off energies. Calculated by use of an MATLAB function. Note the different order of magnitude on the y-axis in **(a)**.

To test the impact of both the magnitude of the photo-ionization cross sections (varied by varying n_r, E_{eff}/E_0 and $m*$) and cut-off energies on cell performance, Cell D5 has the same magnitude as Cell D1 and the same cut-off energies as Cell D4.

Following the work of Yuan et al. [33] Cells D6 and D7 were simulated. These cells have the same cut-off energies as Cell D2 (as these cut-off energies are equivalent to the ones used in ref. [33]), but σ_n^{op} was increased by a factor of 10^4 (Cell D6) and 10^7 (Cell D7) from the level of Cell D2. This was achieved by reducing the effective electron mass. σ_p^{op} was kept at the same level as in D2.

Results

Table 6.3 lists the performance parameters of Cells D1-D7, along with those of B1 (included for comparison). The differences between the performance of Cells D1-D5 is small. The open-circuit voltage is equal for all these cells and the small variation in efficiency is due to the differences in J_{SC} and FF. Cells D6 and D7 both have significantly higher efficiencies and current densities than the other cells. The fill factor is also much higher in Cell D7 than in the rest of the cells. Although these results are impressive and interesting, we shall later see that they are probably very unrealistic to achieve in reality.

Table 6.3: Performance parameters of Cells D1-D7. The performance parameters of Cell B1 (reference cell) is included for comparison.

Cell	η [%]	V_{OC} [V]	J_{SC} [mA/cm^2]	FF [%]
Cell B1	19.1	0.73	39.5	66.2
Cell D1	18.7	0.73	39.2	65.4
Cell D2	19.1	0.73	39.6	66.2
Cell D3	19.3	0.73	41.0	64.5
Cell D4	19.5	0.73	41.7	63.9
Cell D5	19.2	0.73	41.5	63.4
Cell D6	22.1	0.74	45.1	66.5
Cell D7	29.1	0.75	49.7	78.1

Figure 6.17 shows the IV and QE curves of Cell D1, compared with the corresponding curves for Cell B1 (reference cell). The differences between the cells is not large, but it is seen that Cell B1 has a slightly higher current density than Cell D1. The QE curves differ around the main band gap: The QE of Cell B1 is slightly higher than Cell D1 before the main band gap drop, whereas the opposite is true just after the drop.

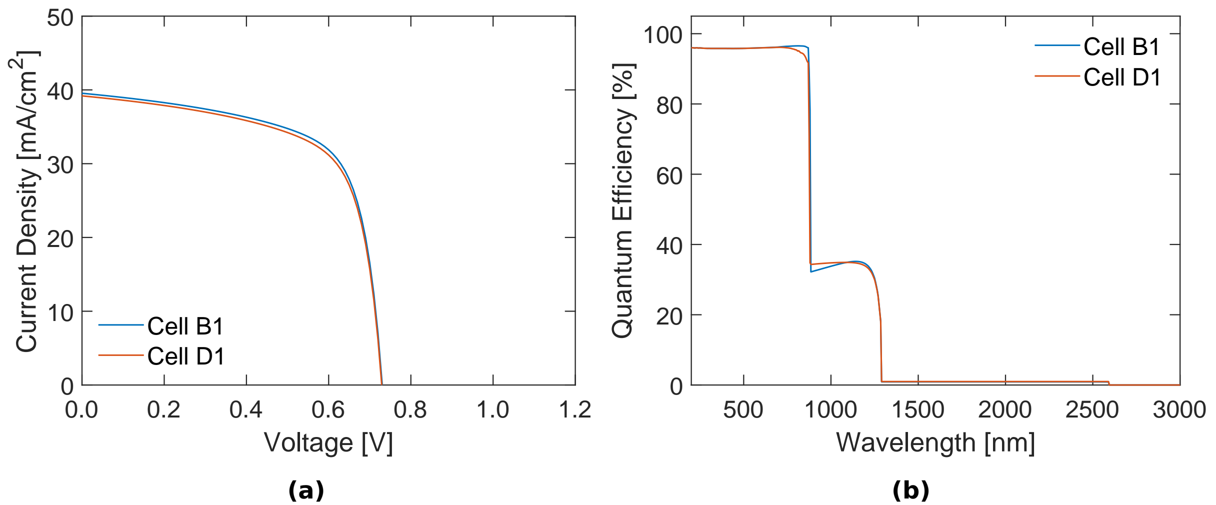

Figure 6.17: (a) IV curve and **(b)** QE curves for Cell D1, compared with those of Cell B1.

Figure 6.18 shows the IV and QE curves of Cells D2, D3 and D4, compared with those of Cell B1. The values in eV of E_n^{cut} and E_p^{cut} for each cell is given in parenthesis in the legends. The only visible difference between the IV curves is in current density and Cell D4 is the cell with the highest J_{SC}. The difference between the QE curves is greatest in the wavelength interval corresponding to the largest of the two sub band gaps. Although not to easy to see

due to the overlap of the curves, Cell B1 and D2 have a QE in excess of 30 % in this interval, whereas the QE of Cell D3 and D4 are close to zero. Around 1300 nm a small dip in the QE curves is also seen.

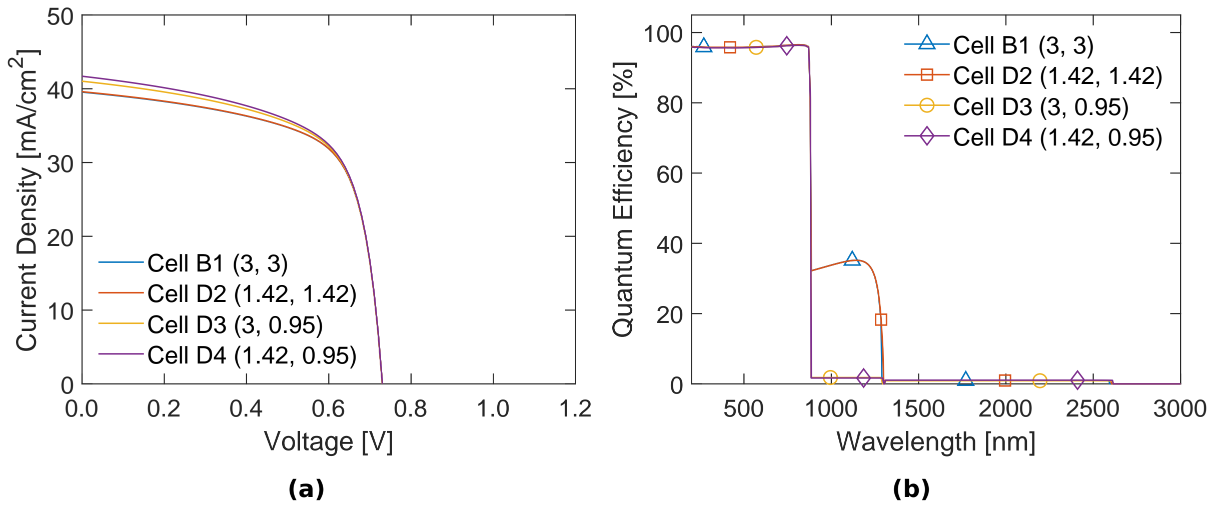

Figure 6.18: (a) IV curves and **(b)** QE curves of Cells D2, D3 and D4, as well as Cell B1 (reference cell). The numbers in the legends are the values in eV of E_n^{cut} and E_p^{cut} for each cell.

In order to better see this dip, as well as the small differences between the QE curves, Figure 6.19(a) zooms in on the same QE curves in the wavelength interval between 1270 nm and 1340 nm and the QE interval between 0 % and 5 %. The dip appears for Cells D3 and D4. Furthermore, at wavelengths longer than 1310 nm (also for the wavelengths exceeding the interval in Figure 6.19(a)), Cell D4 has the highest QE. The occupation probability in the IPV-layer of Cell B1, D2, D3 and D4 are shown in Figure 6.19(b). The occupation is plotted at 0 V, because the difference in both occupation probability and current density (Figure 6.18(a)) is greatest at this voltage. In the middle part of the IPV-layer, there is a significant difference in occupation probability and Cell D4 has the lowest occupation probability.

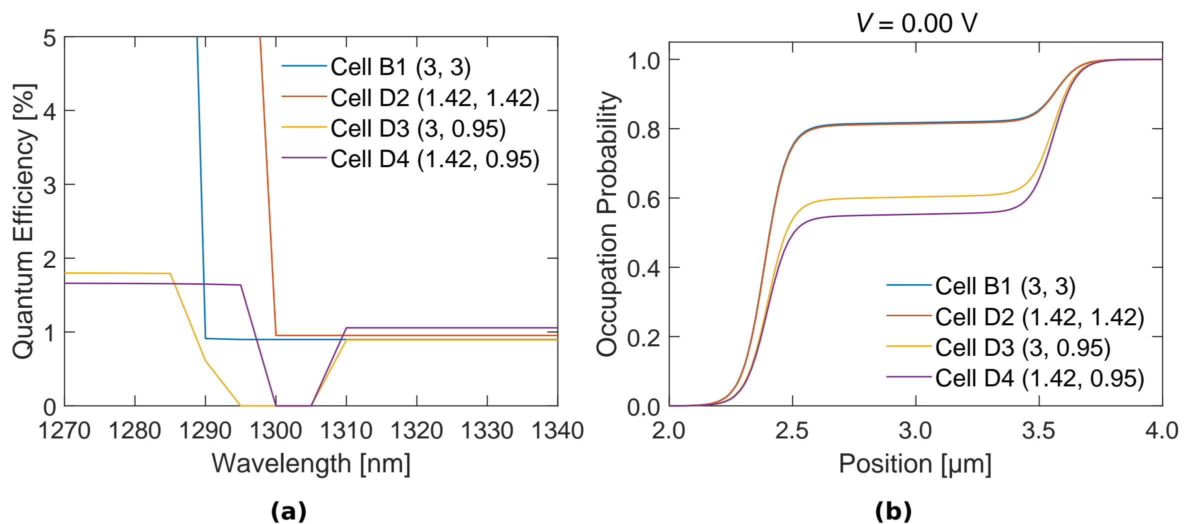

Figure 6.19: (a) Zoomed plot of the QE curves in Figure 6.18(b) and **(b)** occupation probability of Cells B1, D2, D3 and D4 at 0 V. The numbers in the legends are the values in eV of E_n^{cut} and E_p^{cut} for each cell.

Discussion

The difference between the performance of Cell B1 and D1 is small. Furthermore, it is surprising that Cell D1 has a lower current density than Cell B1; one would assume than an increase in photo-ionization cross section should lead to an increase in current density. The reason for this might be related to the cut-off energies of electrons and holes.

Due to the high cut-off energies of Cells B1 and D1, the absorption over the sub band gaps competes with the band-to-band absorption. From equations (3.20) and (3.21), we know that the absorption coefficient for the sub band gaps are proportional to the appropriate photo-ionization cross-section. Given the impurity concentration of $10^{17}\,\text{cm}^{-3}$, and for simplicity assuming $f_{imp} = 1$ for α_n and $f_{imp} = 0$ for α_p, the absorption coefficient for the sub band gaps in Cell B1 is in the order of $\alpha_n = 2 \times 10^1\,\text{cm}^{-1}$ and $\alpha_p = 5\,\text{cm}^{-1}$. For Cell D1 (with about 1000 times higher photo-ionization cross sections), we get absorption coefficients in the order of $\alpha_n = 2 \times 10^4\,\text{cm}^{-1}$ and $\alpha_p = 5 \times 10^3\,\text{cm}^{-1}$. From Figure 5.2, the band to band absorption coefficient (α_{btb}) is overall larger that this, but around the main band gap α_n and α_p of Cell D1 are comparable to α_{btb}.

The magnitude of the photo-ionization cross sections of Cell D1 makes the competition between α_n and αbtb more pronounced. The effect of the competition is best seen when comparing the QE curves of Cells B1 and D1 (Figure 6.17(b)). It should be noted that when the light reaches the IPV-layer (in which the two absorption coefficients are both non-zero), part of the photons have already been absorbed in the p-layer, contributing to the band-to-band generation. This reduces the impact of the competition between the two absorption mechanisms. Anyway, the high σ_n^{op} of Cell D1 gives a higher QE in the wavelength interval corresponding to the largest of the two sub band gaps. At the same time, the high absorption over this sub band gap reduces the QE for the wavelengths that are suitable for band to band absorption, thus "wasting" high energy photons on a smaller band gap.

How the difference between the QE curves influences the current density might be explained by looking at Figure 5.1. The intensity (and the photon flux) of the incident radiation is higher at wavelengths just shorter than the band gap than for wavelengths just longer than the band gap. Thus, part of the explanation as to why the current density is lower in Cell D1 than in Cell B1 could be that the loss of electrons generated at wavelengths just shorter than the band gap is greater than the gain of electrons at wavelengths just longer than the band gap.

To study the impact of varying the cut-off energies, simulations of Cells D2, D3 and D4 were done. The fact that Cell D4 has the highest current density and the highest efficiency, might indicate that the best configuration is for the three different absorption coefficients not to be in competition with each other. Still, Cells D2, D3 and D4 perform rather similarly, and only a small selection of cut-off energies were tested, so it is hard to draw any conclusions.

The QE curves (Figure 6.18(b)) of Cells D3 and D4 differ significantly from those of Cells B1 and D2 in the interval corresponding to the largest of the sub band gaps (873 nm to 1305 nm). Cells D3 and D4 both have a hole cut-off energy of 0.95 eV, meaning σ_p^{op} is zero for wavelengths shorter than 1305 nm. In this interval, the monochromatic light source of the QE simulation is unable to excite electrons from the valence band to the impurity. The impurity is now filled with electrons only by means of the AM1.5 spectrum and thermal excitation. An explanation to the low QE could thus by that it is limited by a low rate of excitation from the valence band to the impurity. By the same logic, it makes sense that the QE of wavelengths corresponding to the smallest of the sub band gaps is low, as σ_n^{op} is zero in this interval.

It is still not obvious why Cell D4 has a higher current density than Cell B1, D2 and D3.

The explanation could simply be that the cut-off energies of Cell D4 makes sure all the photons are utilized efficiently. At first glance at the QE curves in Figure 6.18(b), however, Cell D4 does not seem to be the most efficient of the cells. The zoomed in plot in Figure 6.19(a) holds a possible explanation. Although only part of wavelength interval is shown, the QE of Cell D4 is the highest over the wide wavelength interval from 1310 nm to 2610 nm. The dip in QE for Cells D3 and D4 at around 1300 nm is suspected to be due to the interval between the points at which the photo-ionization cross sections are calculated. Since σ_n^{op} and σ_p^{op} are non-overlapping, a too coarse spacing around 1300 nm could make SCAPS assume the photo-ionization cross sections are zero.

The occupation probabilities in Figure 6.19(b) is partly in agreement with the discussion so far. A lower α_p leads to a lower hole optical emission rate, which in turn leads to a reduction in the occupation at the impurity level. It therefore makes sense that the occupation probability of Cell D3 and D4 are lower than that of B1 and D2. When reducing α_n from Cell D3 to D4, I would expect an increase in occupation probability, because a more narrow range of photons could contribute to exciting electrons from the impurity level to the conduction band. It is therefore difficult to explain why the occupation probability of Cell D4 is lower than that of Cell D3.

Above, it was suggested that the reason Cell D1 (with increased magnitude of the photo-ionization cross sections) performed worse than Cell B1 was due to the cut-off energies. It is therefore expected that when increasing the magnitude of the photo-ionization cross sections in a cell where σ_n^{op} and σ_p^{op} are non-overlapping, the performance will improve. In other words, Cell D5 is expected to perform better than Cell D4. The fact that is does not (see Table 6.3), weakens the discussion above, and it is unclear what the reasons for this behaviour is.

Another possibility is to vary the magnitude of σ_n^{op} and σ_p^{op} independently. In 2017, Yuan et al. published a numerical study of the influence of photo-emission cross sections on solar cell performance, also using SCAPS [33]. They looked at an indium impurity (0.157 eV above E_V) in silicon (band gap of 1.12 eV). They assumed the photo-ionization cross sections to be wavelength independent and to be zero for wavelengths shorter than that of the band gap. By varying σ_n^{op} and σ_p^{op} independently over approximately ten orders of magnitude, they concluded that high σ_n^{op} and low σ_p^{op} were beneficial for cell performance. They argued that a high σ_n^{op} would increase the current density, but since the impurity was close to the valence band, the excitation from the valence band to the impurity level had a high enough rate by means of only thermal excitation. A high σ_p^{op} would, according to Yuan et al., instead "[. . .] facilitate the absorption of the sub-bandgap photons and thus reduce the photon flux available for the electron photoemssion process" [33, p. 3].

Since the impurity in the current work is also closer to the valence band than it is to the conduction band, an equivalent argument can be made here. By decreasing the effective mass of electrons, an increase in the magnitude of only σ_n^{op} can be achieved. This is done for Cells D6 and D7. The great improvement in performance for these cells compared to that of Cells D1-D5 looks promising. However, the magnitude of σ_n^{op} has to be increased by a factor of 10^4 for a significant increase of efficiency, and is for the case of Cell D7 increased by a factor 10^7. As the increase by a factor of 825 for σ_n^{op} and σ_p^{op} in Cell D1 compared to Cell B1 is already unrealistic, it is hard to imagine being able to vary the photo-ionization cross sections by several additional orders of magnitude. It is confirmed that a σ_n^{op} much higher than σ_p^{op} is beneficial for the cells studied here, but the results of Cell D6 and D7 are not discussed further and are not viewed as realistic IPV solar cells.

As a final comment on the influence of the photo-ionization cross sections it should be said that the results are discussed under significant uncertainty. There are many factors

at play, and trying to make sense of the behaviour of the cells is a comprehensive task. The fact that some results contradict the discussion made for others indicate a that there is more to the results than have been discussed here. As such, although the results and discussion in this subsection sheds light on the mechanisms involved, one should be careful to draw conclusions based on the results and discussion.

6.4.2 Thermal Capture Cross Section

To test the influence of the thermal capture cross sections of electrons (σ_n^{th}) and holes (σ_p^{th}), these parameters were in Cells E1-E66 varied from 10^{-22} cm^2 to 10^{-12} cm^2. Other than that, Cells E1-E66 are identical to Cell B1 (reference cell). This is done much in the same way as was done for indium doped silicon by Yuan et. al. in 2011 [9]. They also used SCAPS to simulate the effect of thermal capture cross section on cell performance. Based on values of σ_n^{th} and σ_p^{th} found in literature[29][30], the performance of Cell E67, with σ_n^{th} = 10^{-19} cm^2 and σ_p^{th} = 10^{-16} cm^2, is viewed more carefully. Besides the thermal capture cross sections, also Cell E67 is equal to Cell B1.

Results

The performance parameters of Cells E1-E66 as a function of σ_n^{th} and σ_p^{th} are shown in Figure 6.20. For comparison, horizontal lines indicating the values of the performance parameters for Cells A2 (impurity free cell with light trapping) and Cell B1 (reference cell) are included as well.

The values of all four performance parameters decrease both with increasing σ_n^{th} and with increasing σ_p^{th}.

For the efficiency (Figure 6.20(a)), varying σ_n^{th} between 10^{-22} cm^2 and 10^{-18} cm^2 results in small changes. In fact, the curves for σ_n^{th} = 10^{-22} cm^2 and σ_n^{th} = 10^{-20} cm^2 more or less overlap. When σ_n^{th} is increased above 10^{-18} cm^2, the efficiency is greatly decreased. The influence of varying σ_p^{th} is most pronounced in the interval between 10^{-19} cm^2 and 10^{-13} cm^2. Decreasing σ_p^{th} below 10^{-19} cm^2 or increasing it above 10^{-13} cm^2 has little effect on the efficiency.

When σ_p^{th} is smaller than 10^{-19} cm^2, V_{OC} (Figure 6.20(b)) is around the level of Cell A2 and more or less constant for all values of σ_n^{th}. When σ_p^{th} is increased above 10^{-19} cm^2, V_{OC} deteriorates rapidly. The greater σ_n^{th} is, the greater is the deterioration.

For most of the simulations, J_{SC} (Figure 6.20(c)) seem to have a similar dependence on σ_n^{th} and σ_p^{th} as the efficiency. The magnitude of the variation, however, is smaller for J_{SC} than for the efficiency. The curve of σ_n^{th} = 10^{-12} cm^2 displays a tremendous decrease in JSC as σ_p^{th} increases.

The curves of the fill factor are somewhat less smooth than the other curves, making it harder to identify the fill factor's dependence on σ_n^{th} and σ_p^{th}. With the exception of the curve of σ_n^{th} = 10^{-12} cm^2, the *FF* seem to vary in a similar manner as η and J_{SC}.

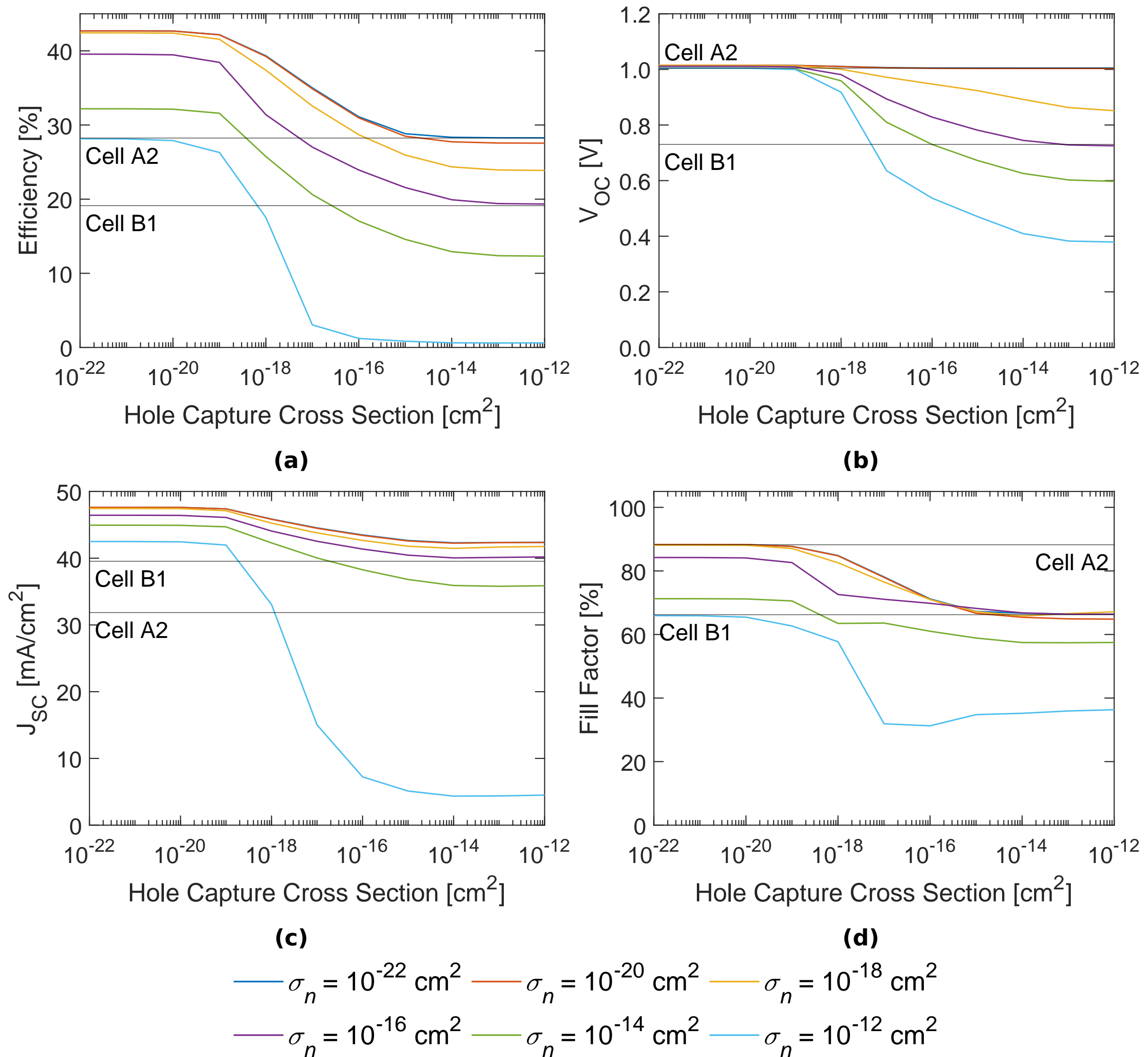

Figure 6.20: (a) Efficiency, **(b)** open-circuit voltage, **(c)** short-circuit current density and **(d)** fill factor of Cells E1-E66, as a function of thermal capture cross sections of electrons (σ_n^{th}) and holes (σ_p^{th}). The horizontal lines indicate the values of the four performance parameters for Cells A2 (impurity free cell with light trapping) and B1 (reference cell). The legends apply to all four subfigures.

The performance parameters of Cell E67 is shown in Table 6.4. The performance parameters of Cells B1 and A2 are included for comparison. The IV and QE curves of Cells E67, A2 and B1 are shown in Figure 6.21. Cell E67 has a higher efficiency than Cells A2 and B1, because it benefits from a high current density without significant loss of open-circuit voltage. The fill factor is, however, much lower for Cell D67 than for Cell A2. Cell E67 also displays an increase in QE in the interval between 873 nm and 1305 nm.

Table 6.4: Performance parameters of Cell E67. The performance parameters of Cell A2 (impurity free cell with light trapping) and B1 (reference cell) is included for comparison.

Cell	η [%]	V_{OC} [V]	J_{SC} [mA/cm^2]	FF [%]
Cell A2	28.2	1.00	31.9	88.2
Cell B1	19.1	0.73	39.5	66.2
Cell E67	30.3	1.00	43.2	70.5

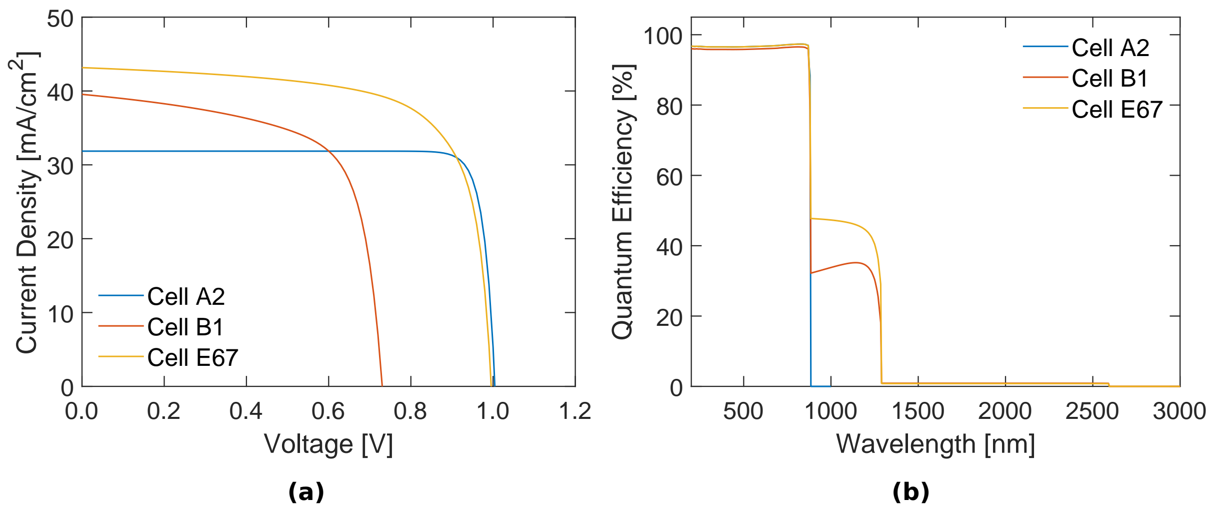

Figure 6.21: (a) IV curves and **(b)** QE curves of Cells A2, B1 and E67.

Discussion

The most obvious conclusion from the results of Figure 6.20 is that the thermal capture cross sections have a great influence on cell performance, and are thus important to control when making IPV solar cells. By varying σ_n^{th} and σ_p^{th} cells with efficiencies higher than both Cells A2 and B1 were achieved. An important question is of course how realistic the values of σ_n^{th} and σ_p^{th} are.

For iron doped GaAs with an impurity level comparable to the one of Cells E1-E66, thermal capture cross sections in the order of 10^{-19} cm^2 for electrons and 10^{-16} cm^2 for holes have been reported [29][30]. With these thermal capture cross sections, Cell E67 outperform Cell B1 by a large margin, and performs better even than Cell A2. This is a promising result with respect to realizing efficient IPV solar cells.

Two things should kept in mind, however. First, Cell E67 (and all the cells presented up to this point, except Cell A1) are simulated with the assumption of maximum light trapping (R_b = 100 % and R_{fi} = 99.9999 %). The influence of the surface reflection will be studied briefly later in this chapter. At this point, we can point out that the maximum light trapping used to study the IPV effect is probably unrealistic to achieve in reality. Second, in ref.

[30], σ_n^{th} is presented for n-type GaAs and σ_p^{th} for p-type GaAs. Up to this point in this thesis, the impurities have been assumed to neutral, and the IPV-layer to be without shallow background doping. How σ_n^{th} and σ_p^{th} are affected by doping is not investigated in this thesis. It is merely stated that this is another element increasing the uncertainty of the results.

The IV curves in Figure 6.21(a) shows exactly what we want to achieve for IPV solar cells. An increase in current density without a minimal reduction in V_{OC}. The fact that J_{SC} is even higher for Cell E67 than for B1 might be explained by the increase in QE for the wavelengths corresponding to the largest of the sub band gaps. The fill factor leads to a lower efficiency than could be expected from looking at only V_{OC} and J_{SC}.

6.4.3 Impurity Type and Shallow Background Doping

Using Cell E67 as a starting point, Cells F1 (single acceptor) and F2 (single donor) were were used to test the influence of the impurity type. Cells F3-F7 used single acceptor as impurity type, but additionally contain a shallow donor density in the IPV-layer, varied from $10^{15}\,\text{cm}^{-3}$ to $10^{19}\,\text{cm}^{-3}$. The values for the shallow donor density of Cell F8 is based on the claim by Würfel and Würfel that optimal absorption can be acheieved through compensating half of the deep level impurities by shallow ones of opposite type (in the example of Cell F8, deep acceptors halfway compensated by shallow donors) [2, p. 205].

Results

The performance parameters of Cells F1-F8 are listed in Table 6.5, along with those of Cells A2 and B1. In the cases of Cells F2 ad F5, I was unable to avoid convergence failure in the IV simulation. The simulations were stopped at 0.92 V. The values for V_{OC} and FF are therefore extrapolated by SCAPS.

Table 6.5: Performance parameters of Cells F1-F8. For IV the simulation of Cell F2, I was unable to avoid convergence failure, and the simulation was stopped at 0.92 V. The values of V_{OC} and FF are therefore extrapolated by SCAPS. The performance parameters of Cells A2 (impurity free cell with light trapping) and B1 (reference cell) are included for comparison.

Cell	**η [%]**	**V_{OC} [V]**	**J_{SC} [mA/cm^2]**	**FF [%]**
Cell A2	28.2	1.00	31.9	88.2
Cell B1	19.1	0.73	39.5	66.2
Cell F1	28.2	1.00	32.8	86.0
Cell F2	36.8	1.11 (extrapolated)	45.7	72.9 (extrapolated)
Cell F3	28.3	1.00	33.0	85.9
Cell F4	29.3	0.98	34.8	85.4
Cell F5	36.8	1.11 (extrapolated)	45.7	72.9 (extrapolated)
Cell F6	31.4	1.02	34.9	88.1
Cell F7	28.0	1.02	31.1	88.3
Cell F8	33.5	0.97	41.1	84.3

The IV curve of Cell F8 is in Figure 6.22(a) compared to those of Cells A2, B1 and E67. The occupation probability of Cell F8 is shown in Figure 6.22(b), for 0 V, V_M and V_{OC}.

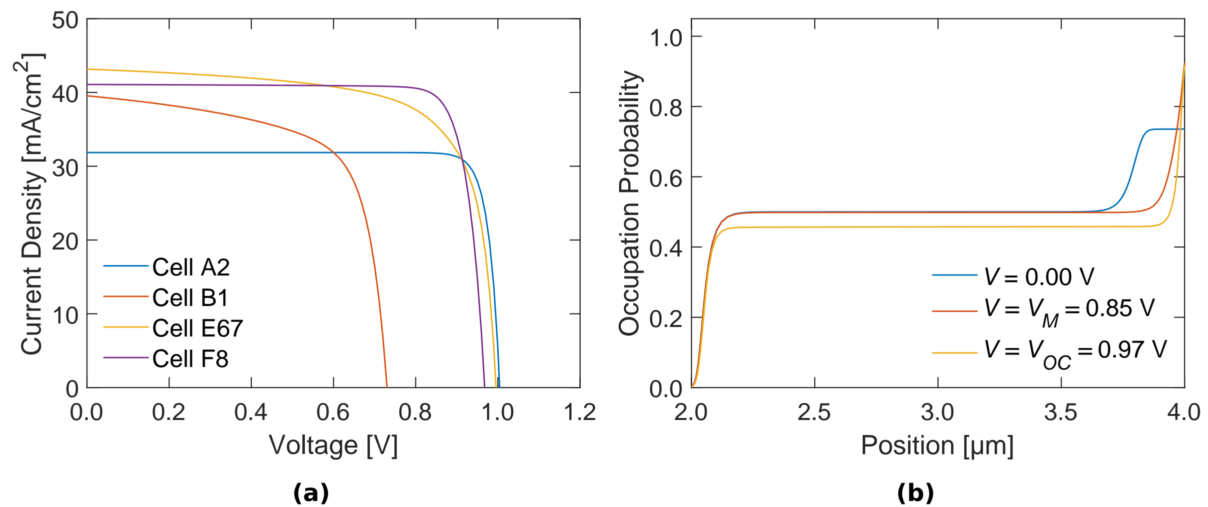

Figure 6.22: (a) IV curve of Cell F8, compared with those of Cells A2, B1 and E67 and **(b)** occupation probability of Cell F8 at 0 V, V_M and V_{OC}.

Discussion

The neutral impurities used so far are not really realistic, but provided by SCAPS as an idealized case. From the SCAPS manual: “[...] a neutral defect does not exist in reality, it is an idealization to help you create a model step by step” [20, p. 30]. Most impurities with energy levels in the bottom half of the band gap of GaAs are acceptor type, with oxygen and selenium as exceptions [34]. Cell F1 is therefore more realistic than Cell F2, which is unfortunate given the high efficiency of Cell F2 and F5. The fact that Cells F2 and F5 perform equally is not surprising; it might very well be that SCAPS does not differentiate between a donor-type deep level impurity and a neutral impurity plus a shallow donor doping of the same density.

The problem with convergence in Cells F2 and F5 increases the uncertainty of the results of these cells. Nevertheless, the simulation were seemingly stopped after V_M (SCAPS suggests a V_M of 0.87 V), suggesting that the values of η and J_{SC} might be trustworthy after all. Should this be the case, Cell F2 represent a great improvement over the impurity free cells. The extrapolated values of V_{OC} and *FF*, are probably too uncertain to be discussed.

The results of Cell F8 are perhaps more trustworthy that Cells F2 and F5. The high efficiency bears with it a optimism on behalf of IPV cells. Apart from the maximum light trapping, Cell F8 is not an unrealistic cell. In Figure 6.22(a), it is seen to manage what Cell E67 could not: To increase J_{SC} from the level of the impurity free cells, without a large reduction in neither V_{OC} or *FF*. This can be related to the half filled impurity, demonstrated in Figure 6.22(b). Electrons and holes populate the impurity in roughly equal amounts, meaning both charge carriers are "ready" for emission to their respective bands.

6.4.4 Internal Front Contact Reflection and IPV-Layer Thickness

Cells G1-G5 were used to test the influence of light trapping, by varying the internal front contact reflection from 99.999 % in Cell G1 to 90 % in Cell G5.

Results

The performance parameters of Cells G1-G5 are listed in Table 6.6. The performance parameters of Cells A2 (impurity free cell with light trapping), B1 (reference cell) and F8 are included for comparison.

Table 6.6: Performance parameters of Cells G1-G5. The performance parameters of Cells A2 (impurity free cell with light trapping), B1 (reference cell) and F8 are included for comparison.

Cell	η [%]	V_{OC} [V]	J_{SC} [mA/cm^2]	FF [%]
Cell A2	28.2	1.00	31.9	88.2
Cell B1	19.1	0.73	39.5	66.2
Cell F8	33.5	0.97	41.1	84.3
Cell G1	33.5	0.97	41.1	84.3
Cell G2	33.2	0.97	40.8	84.1
Cell G3	31.0	0.96	38.8	82.8
Cell G4	26.0	0.95	33.8	80.6
Cell G5	23.8	0.95	31.2	80.3

It is seen that the efficiency is drastically reduced with decreasing internal front contact reflection. In order to perform better than the impurity free cells, the internal front contact reflection needs to be at least 99.9 %. This might not be achievable for real solar cells. Finding out if it is or not and optimizing light trapping in solar cells will be an important task in the development of IPV solar cells.

Chapter 7

Conclusions and Further Work

GaAs IPV solar cells have been studied through numerical simulations using the software SCAPS. It is concluded that SCAPS is well suited for IPV solar cell simulation. Still, the fact that photon recycling is not considered could mean that SCAPS underestimates the performance of the simulated cells.

In this work, it has been studied to what extent a set of material and design parameters affect the solar cell performance. All the parameters considered have an impact on the performance. Nevertheless, as not all of them are easy to control for real solar cells, and because the impact of various parameters differs, some parameters are regarded as more relevant to focus on if real cells are to be made. It is found to be crucial to optimize the light trapping in the cells. Furthermore, reasonably low thermal cross sections are necessary for the benefit of the IPV effect to be greater than the disadvantage of non-radiative recombination. With sufficient light trapping, the IPV effect increase the short-circuit voltage of the cells, but the recombination associated with the impurities reduce the open-circuit voltage.

The best performing cell in this work had an efficiency of 33.5 %. This is a clear improvement over the efficiency of a similar impurity free cell of 28.2 %. These cells had maximum light trapping, meaning a back contact reflection of 100 % and internal front surface reflection of 99.9999 %. When reducing the internal front surface reflection to 90 %, the efficiency dropped to 23.8 %. For the IPV cell to outperform the impurity free cell the internal front contact reflection had to be at least 99.9 %.

It is hard to conclude whether or not IPV solar cells could be an improvement over the commercially available cells of today. They obviously have a potential for efficiency increase. At the same time, the requirements on certain material parameters are high. If suitable semiconductor and impurity materials can be found, IPV solar cells may have a place in the world of tomorrow. It was seen that adjusting design parameters such as impurity type and background doping could improve cell performance. This is also an optimistic result, as it indicates further improvement by changing parameters that are possible to control in real cells.

As further work, it is suggested to search for materials with the desired properties and to optimize the cell design. Simulation can be a useful tool in this regard, and SCAPS can be a good starting point. The effect of photon recycling could be modelled to find out if the results generated by SCAPS underestimates the potential of IPV cells. Experimental work will of course be vital, to test how the predicted results hold up in reality. It is highly relevant to work to optimize light trapping. Other suggestions for further work include evaluating other models than the Lucovsky model for the photo-ionization cross section and to test the influence of varying several of the parameters studied in this work simultaneously.

Bibliography

[1] "Statistical Review of World Energy: 70th edition," BP, Tech. Rep., 2021, [Online]. Available: https://www.bp.com/en/global/corporate/energy-economics/statistical-review-of-world-energy.html, Accessed: 21.12.21.

[2] P. Würfel and U. Würfel, *Physics of Solar Cells: From Basic Principles to Advanced Concepts*, 3rd ed. Weinheim: Wiley-VCH, 2016.

[3] M. Wolf, "Limitations and Possibilities for Improvement of Photovoltaic Solar Energy Converters: Part I: Considerations for Earth's Surface Operation," *Proceedings of the IRE*, vol. 48, pp. 1246–1263, 1960.

[4] G. Lucovsky, "On the photoionization of deep impurity centers in semiconductors," *Solid State Communications*, vol. 3, pp. 299–302, 1965.

[5] G. Güttler and H. J. Queisser, "Impurity photovoltaic effect in silicon," *Energy Conversion*, vol. 10, pp. 51–55, 1970.

[6] M. J. Keevers and M. A. Green, "Efficiency improvements of silicon solar cells by the impurity photovoltaic effect," *Journal of Applied Physics*, vol. 75, pp. 4022–4031, 1994.

[7] M. Burgelman, P. Nollet, and S. Degrave, "Modelling polycrystalline semiconductor solar cells," *Thin Solid Films*, vol. 361-362, pp. 527–532, 2000.

[8] S. Khelifi, J. Verschraegen, M. Burgelman, and A. Belghachi, "Numerical simulation of the impurity photovoltaic effect in silicon solar cells," *Renewable Energy*, vol. 33, pp. 293–298, 2008.

[9] J. Yuan, H. Shen, H. Huang, and X. Deng, "Positive or negative gain: Role of thermal capture cross sections in impurity photovoltaic effect," *Journal of Applied Physics*, vol. 110, 104508, 2011.

[10] T. S. Bysting, "Numerical Simulation of Single Junction GaAs Solar Cell Performance Using SCAPS," Unpublished Specialization Project Report (NTNU course code: TFY4520), Norwegian University of Science and Technology, Norway, 2020.

[11] M. A. Green, *Solar Cells: Operating Principles, Technology and System Applications*. Kensington: The University of New South Wales, 1998, First published by Prentice-Hall, Inc., 1982, reprinted by The Univerisity of New South Wales.

[12] S. M. Sze and M. K. Lee, *Semiconductor Devices: Physics and Technology*, 3rd ed. New York: John Wiley & Sons, Inc., 2012.

[13] B. G. Streetman and S. K. Banerjee, *Solid State Electronic Devices*, 7th ed. Harlow: Pearson Education Limited, 2016.

[14] J. Nelson, *The Physics of Solar Cells*. London: Imperial College Press, 2003.

[15] W. Shockley and W. T. Read, “Statistics of the Recombinations of Holes and Electrons,” *Phys. Rev.*, vol. 87, pp. 835–842, Sep. 1952.

[16] R. N. Hall, “Electron-Hole Recombination in Germanium,” *Phys. Rev.*, vol. 87, p. 387, Jul. 1952.

[17] G. Beaucarne, A. S. Brown, M. J. Keevers, R. Corkish, and M. A. Green, “The impurity photovoltaic (IPV) effect in wide-bandgap semiconductors: an opportunity for very-high-efficiency solar cells?” *Progress in Photovoltaics: Research and Applications*, vol. 10, pp. 345–353, 2002.

[18] H. G. Grimmeiss and L. .-A. Ledebo, “Photo-ionization of deep impurity levels in semiconductors with non-parabolic bands,” *Journal of Physics C: Solid State Physics*, vol. 8, pp. 2615–2626, Aug. 1975.

[19] A. H. Edwards and W. B. Fowler, “Photoionization of group-III acceptors in silicon,” *Phys. Rev. B*, vol. 16, pp. 3613–3617, 1977.

[20] M. Burgelman, K. Decock, A. Niemegeers, J. Verschraegen, and S. Degrave, *SCAPS manual*, Department of Electronics and Information Systems, University of Gent, Belgium, 2020, [Online]. SCAPS installation website, available on request (Marc.Burgelman@ugent.be), Accessed: 26.01.21.

[21] K. Decock and M. Burgelman, *Getting started with SCAPS*, Department of Electronics and Information Systems, University of Gent, Belgium, 2011, [Online]. SCAPS installation website, available on request (Marc.Burgelman@ugent.be), Accessed: 26.01.21.

[22] K. Decock, S. Khelifi, and M. Burgelman, “Modelling multivalent defects in thin film solar cells,” *Thin Solid Films*, vol. 519, pp. 7481–7484, 2011.

[23] M. Burgelman, K. Decock, S. Khelifi, and A. Abass, “Advanced electrical simulation of thin film solar cells,” *Thin Solid Films*, vol. 535, pp. 296–301, 2013.

[24] J. Verschraegen and M. Burgelman, “Numerical modeling of intra-band tunneling for heterojunction solar cells in scaps,” *Thin Solid Films*, vol. 515, pp. 6276–6279, 2007.

[25] K. Decock, P. Zabierowski, and M. Burgelman, “Modeling metastabilities in chalcopyrite-based thin film solar cells,” *Journal of Applied Physics*, vol. 111, 043703, 2012.

[26] S. Khelifi, M. Burgelman, J. Verschraegen, and A. Belghachi, “Impurity photovoltaic effect in GaAs solar cell with two deep impurity levels,” *Solar Energy Materials and Solar Cells*, vol. 92, pp. 1559–1565, 2008.

[27] J. R. Lowney and H. S. Bennett, “Majority and minority electron and hole mobilities in heavily doped GaAs,” *Journal of Applied Physics*, vol. 69, pp. 7102–7110, 1991.

[28] D. L. Dexter, “Theory of the Optical Properties of Imperfections in Nonmetals,” in *Advances in Research and Applications*, ser. Solid State Physics, F. Seitz and D. Turnbull, Eds., vol. 6, Academic Press, 1958, pp. 353–411.

[29] M. Kleverman, P. Omling, L.-Å. Ledebo, and H. G. Grimmeiss, “Electrical properties of Fe in GaAs,” *Journal of Applied Physics*, vol. 54, pp. 814–819, 1983.

[30] D. V. Lang and R. A. Logan, “A study of deep levels in GaAs by capacitance spectroscopy,” *Journal of Electronic Materials*, vol. 4, pp. 1053–1066, 1975.

[31] M. A. Green, E. D. Dunlop, J. Hohl-Ebinger, M. Yoshita, N. Kopidakis, and X. Hao, “Solar cell efficiency tables (Version 58),” *Progress in Photovoltaics: Research and Applications*, vol. 29, pp. 657–667, 2021.

[32] B. M. Kayes, H. Nie, R. Twist, S. G. Spruytte, F. Reinhardt, I. C. Kizilyalli, and G. S. Higashi, “27.6% Conversion efficiency, a new record for single-junction solar cells under 1 sun illumination,” in *2011 37th IEEE Photovoltaic Specialists Conference*, 2011, pp. 4–8.

[33] J. Yuan, H. Huang, X. Deng, Z. Yue, Y. He, N. Zhou, and L. Zhou, “Photoemission cross section: A critical parameter in the impurity photovoltaic effect,” *Chinese Physics B*, vol. 26, 018503, Jan. 2017.

[34] S. M. Sze and J. C. Irvin, “Resistivity, mobility and impurity levels in GaAs, Ge, and Si at 300°K,” *Solid-State Electronics*, vol. 11, pp. 599–602, 1968.

Appendix A

SCAPS Script Example

```
// STANDARD SIMULATION SET FOR A SINGLE CELL

// SIMULATES AND SAVES THE FOLLOWING FOR ONE .def-FILE:
// CURRENT DENSITY-VOLTAGE (IV) BETWEEN 0 V AND Voc
// QUANTUM EFFICIENCY (QE) BETWEEN 200 nm AND 3000 nm
// ENERGY BAND DIAGRAMS (EB) AT 0 V, Vm AND Voc
// GENERATION-RECOMBINATION RATES (GEN) AT 0 V, Vm AND Voc
// OCCUPATION PROBABILITY (OCC) AT 0 V, Vm AND Voc

// THE DEFINITION FILE THAT IS LOADED BELOW SHOULD BE CHANGED ACCORDING
// TO WHICH CELL THAT IS TO BE SIMULATED
// RESULTS ARE SAVED ACCORDING TO THE FILENAMES LISTED IN THE FILE
// list_of_result_filenames.txt

// LOAD CELL
load definitionfile CellB1.def

// ACTION PANEL SETTINGS FOR IV AND QE SIMULATIONS
action light
action iv.checkaction 1
action iv.startv 0
action iv.stopv 2
action iv.stopaftervoc
action iv.increment 0.01
action qe.checkaction 1
action qe.startlambda 200
action qe.stoplambda 3000
action qe.increment 5

// PERFORM IV AND QE SIMULATIONS
calculate singleshot

// ASSIGN Vm AND Voc TO THE SCRIPT VARIABLES avalue AND bvalue
get characteristics.vmpp avalue
get characteristics.voc bvalue

// CHECK SCRIPT VARIABLES
show scriptvariables
```

```
39
40 // SAVE IV AND QE RESULTS
41 save results.iv.filenamelist script\list_of_result_filenames.txt[0]
42 save results.qe.filenamelist script\list_of_result_filenames.txt[1]
43
44 // CLEAR ACTION PANEL SETTINGS
45 clear actions
46
47 // PERFORM AND SAVE EB, GR AND OP SIMULATIONS AT 0 V
48 action workingpoint.voltage 0
49 load singleshotbatch
50 load recordersettingsfile eb.srf
51 calculate recorder
52 save results.recorder.filenamelist script\list_of_result_filenames.txt[2]
53 load recordersettingsfile gen_defectinlayer2.srf
54 calculate recorder
55 save results.recorder.filenamelist script\list_of_result_filenames.txt[3]
56 load recordersettingsfile occ_defectinlayer2.srf
57 calculate recorder
58 save results.recorder.filenamelist script\list_of_result_filenames.txt[4]
59
60 // PERFORM AND SAVE EB, GR AND OP SIMULATIONS AT Vm
61 action workingpoint.voltage avalue
62 load singleshotbatch
63 load recordersettingsfile eb.srf
64 calculate recorder
65 save results.recorder.filenamelist script\list_of_result_filenames.txt[5]
66 load recordersettingsfile gen_defectinlayer2.srf
67 calculate recorder
68 save results.recorder.filenamelist script\list_of_result_filenames.txt[6]
69 load recordersettingsfile occ_defectinlayer2.srf
70 calculate recorder
71 save results.recorder.filenamelist script\list_of_result_filenames.txt[7]
72
73 // PERFORM AND SAVE EB, GR AND OP SIMULATIONS AT Voc
74 action workingpoint.voltage bvalue
75 load singleshotbatch
76 load recordersettingsfile eb.srf
77 calculate recorder
78 save results.recorder.filenamelist script\list_of_result_filenames.txt[8]
79 load recordersettingsfile gen_defectinlayer2.srf
80 calculate recorder
81 save results.recorder.filenamelist script\list_of_result_filenames.txt[9]
82 load recordersettingsfile occ_defectinlayer2.srf
83 calculate recorder
84 save results.recorder.filenamelist script\list_of_result_filenames.txt[10]
85
86 // CLEAR SCRIPTVARIABLES AND ACTION PANEL SETTINGS
87 clear scriptvariables.all
88 clear actions
```

Appendix B

MATLAB Implementation of the Lucovsky Model

```
function lucovsky(Eg, Eimp, n, EffFieldRatio, m_e, m_h, CutOff_e, CutOff_h)
% Writes optical capture cross section for electrons and holes in SQUARE
% METERS as a function of wavelength in nanometers to file for use in SCAPS
% Plots optical capture cross section for electrons and holes in SQUARE
% CENTIMETERS as a function of wavelength in nanometers

% INPUT ARGUMENTS
% Eg: Band gap [eV]
% Eimp: Impurity energy level above valence band edge [eV]
% n: Refractive index [dimensionless]
% EffFieldRatio: Effective field ratio [dimensionless]
% m_e: Effective mass of electrons [dimensionless]
% m_h: Effective mass of holes [dimensionless]
% CutOff_e: Highest energy with non-zero sigma_e [eV]
% CutOff_h: Highest energy with non-zero sigma_h [eV]

% CHECK IF ENERGY INPUT ARGUMENTS ARE VALID
r = false;
if (Eg - Eimp) > CutOff_e
    fprintf('The electron ionization energy is larger than the electron ');
    fprintf('cutoff energy.\n');
    r = true;
end
if Eimp > CutOff_h
    fprintf('The hole ionization energy is larger than the hole ');
    fprintf('cutoff energy.\n');
    r = true;
end
if r == true
    fprintf('Please try with other input parameters.\n');
    return;
end

% CONSTANTS
q = 1.602e-19; % [A*s]
```

```
36 h = 4.136e-15; % [eV*s]
37 hbar = 6.582e-16; % [eV*s]
38 m_0 = 9.109e-31; % [kg]
39 c = 2.998e8; % [m/s]
40 eps_0 = 8.85e-12; % [(A*s)/(V*m)]
41
42 % PHOTON ENERGY AND WAVELENGTH
43 Ei_e = Eg - Eimp;
44 Ei_h = Eimp;
45 Eph_e = Ei_e:0.01:CutOff_e;
46 Eph_h = Ei_h:0.01:CutOff_h;
47 lambda_e = flip((h*c*1e9)./Eph_e);
48 lambda_h = flip((h*c*1e9)./Eph_h);
49
50 % CALCULATE SIGMA IN SQUARE METERS
51 % Prefactor
52 PreFactor_e = (4*EffFieldRatio^2*q^2*hbar)/(3*n*c*eps_0*m_0*m_e);
53 PreFactor_h = (4*EffFieldRatio^2*q^2*hbar)/(3*n*c*eps_0*m_0*m_h);
54
55 % Calculate sigma
56 SigmaForEph_e = PreFactor_e*(((Ei_e^0.5)*((Eph_e-Ei_e).^1.5))./(Eph_e.^3));
57 SigmaForEph_h = PreFactor_h*(((Ei_h^0.5)*((Eph_h-Ei_h).^1.5))./(Eph_h.^3));
58
59 % Flip to match with values of wavelength in lambda_e and lambda_h
60 SigmaForLambda_e = flip(SigmaForEph_e);
61 SigmaForLambda_h = flip(SigmaForEph_h);
62
63 % WRITE SIGMA TO FILE IN SQUARE METERS
64 fid_e = fopen('C:\SCAPS\optcapt\lucovsky_e.opt','w');
65 fprintf(fid_e,'%10.4f   %10.4e\n',[lambda_e; SigmaForLambda_e]);
66 fclose(fid_e);
67
68 fid_h = fopen('C:\SCAPS\optcapt\lucovsky_h.opt','w');
69 fprintf(fid_h,'%10.4f   %10.4e\n',[lambda_h; SigmaForLambda_h]);
70 fclose(fid_h);
71
72 % PLOT SIGMA IN SQUARE CENITMETERS
73 hold on
74 plot(lambda_e, 1e4*SigmaForLambda_e, 'linewidth', 1);
75 plot(lambda_h, 1e4*SigmaForLambda_h, 'linewidth', 1);
76
77 % FORMAT PLOT
78 ax = gca;
79 ax.XLabel.String = 'Wavelength [nm]';
80 ax.YLabel.String = 'Photo-Ionization Cross Section [cm^2]';
81 ax.FontSize = 16;
82 ax.LineWidth = 0.75;
83 ax.Box = 'on';
84 ax.XAxis.TickLabelFormat = '%.0f';
85 ax.YAxis.TickLabelFormat = '%.1f';
86
87 % LEGENDS
88 leg = legend('Electrons', 'Holes');
89 leg.FontSize = 16;
```

```
90  leg.Box = 'off';
91  leg.Location = 'northeast';
92
93  end
```

Appendix C

Personal Communication

This appendix contains personal communication between SCAPS developer Honorary Professor Marc Burgelman and me. More specifically, it contains three documents in which Burgelman answers my questions regarding the effective field ratio in the Lucovsky model (section C.1), the implementation of the Lucovsky model in SCAPS (section C.2) and the implementation of the IPV effect in SCAPS (section C.3). The documents are included to serve as a reference for my description of the mentioned topics and as supplementary reading material. They are included with permission from Burgelman.

C.1 On the Effective Field Ratio in the Lucovsky Model

Received via e-mail from Marc Burgelman on the 22nd of September, 2020.

This document was originally an answer from Burgelman to another SCAPS user having a question similar to mine. Since I have not spoken with this user, I concealed the name.

SCAPS and the meaning of the parameter $E_{eff}E_0$ in the Lucovsky calculation of the IPV optical cross section of an impurity

Questions by

Answers by Marc Burgelman, ELIS, University of Gent, April 21, 2016

Question:

(20-4-2016) In the SCAPS defect properties panel, for the IPV optical capture properties, would you please indicate, if possible, the way to evaluate the effective field ratio. We are trying with Lucovsky model (1965), but it is not really evident. A formulae found in the attached paper of G. Güttler et al. (1970) is indicative but for silicon material.

(20-4-2016) The 2nd issue related to the SCAPS panel 'defect properties' where the parameter "Field Effective Ratio" appears. As it is relatively new domain and SCAPS is pioneer for IPV effect study, the SCAPS manual does not mention any indication and the idea was just to contact you to have (if possible) information available.

Answer

The SCAPS manual says, at page 26 (latest version):

SCAPS is able to simulate the IPV-effect. Its parameters can be set on the defect density panel. The algorithms and an example is given in [8, 9]. More examples are found in articles referring to this article, e.g. [10]. An example '*.def'-file is provided with the SCAPS installation with ample comments.

[8] J. Verschraegen, S. Khelifi, M. Burgelman, A. Belgachi, 21st European Photovoltaic Solar Energy Conference, Dresden, Germany, Sept. 2006, 2006.
[9] S. Khelifi, M. Burgelman, J. Verschraegen, A. Belghachi, *Impurity photovoltaic effect in GaAs solar cell with two deep impurity levels*, Solar Energy Materials and Solar Cells, 92 (2008) 1559-1565.
[10] S. Khelifi, J. Verschraegen, M. Burgelman, A. Belgachi, *Numerical simulation of the impurity photovoltaic effect in silicon solar cells*, Renewable Energy, 33 (2008) 293-298.

… thus not much direct information: indeed, IPV is an sophisticated phenomenon, and using it is intended for specialist users, not so much for the common SCAPS user; therefore the IPV-interessees are referred to the literature for further explanation of the phenomenon.

So, look-up ref. [9] of our SCAPS manual, and find the text fragment of Fig. 1. So the meaning is clear already, without having further to look up Lucovsky's 1965 paper, or Dexter's 1958 paper that is cited for this issue by Lucovsky. From this short text fragment, together with basic knowledge on electrostatics (any elementary course), we can understand that:

- the electric fields E_{eff} and E_0 are optical electric fields, thus electric fields of the light waves at the wavelengths λ at which the IPV effect is studied.
- the field E_0 is the (optical) electric field of a plane wave (at wavelength λ) incident on a homogeneous, defect free medium.
- however, at the position of the impurity, not the external (optical) field E_0 is felt, but the 'internal', or 'local', or (in the terminology here) 'effective' field E_{eff}.
- to find the relation between E_{eff} and E_0, follow the treatment of 'local electric field' from standard text book chapters on electrostatics.
- in such standard treatment, they suppose that the material, even if it contains (some) impurities, is still homogeneous with its original dielectric constant ε_{out}

- … but that an impurity is excluded by a cavity with internal dielectric constant ε_{in}.
- since the cavity contains only one atom (the impurity), it makes not much sense to speak of a ε_{in}. Thus usually, one assumes that the cavity is empty (vacuum), and assumes $\varepsilon_{in} = 1$.
- usually (and here we also) one assumes that the cavity is spherical. If your crystal structure and/or impurity 'geometry' is something special, you could easily (in extreme simplification) assume that your cavity is needle shaped, or a flat disk; when you like mathematics, you can more generally work with ellipsoids.
- the problem is thus a basic electrostatic problem: inside an infinite material of dielectric constant ε_{out}, there is a spherical cavity with dielectric constant ε_{in}; the whole is immersed in a uniform electric field E_0; what is the electric field E_{eff} inside the cavity?
- this is a standard electrostatic problem. The solution is:
- $\frac{E_{eff}}{E_0} = \frac{3\varepsilon_{out}}{2\varepsilon_{out} + \varepsilon_{in}} \quad = \frac{3\varepsilon_{out}}{2\varepsilon_{out} + 1}$ when $\varepsilon_{in} = 1$
- (meaning also that the electric field inside the cavity uniform, and that it does not depend on the radius of the cavity)
- … so, this is what you could use for your material as Lucovsky parameter E_{eff}/E_0.
- mind that it is about optical electric fields, not static electric field. Hence, do not use the static dielectric constant ε_s, but the optical dielectric constant (at wavelength λ) ε_∞, that can usually be approximated by the square of the refractive index n.
- in our article cited above, we simply took $E_{eff}/E_0 = 1$ (… a bit lazy… ☺)
- mind that this E_{eff}/E_0 ratio is squared and then enters as a pre-factor in the calculation of σ_{opt}. Since such capture cross section is a property of 'logarithmic nature' (it can vary over many orders of magnitude), a small variation is not suspected to influence e.g. solar cell parameters substantially at all (but you can check that with SCAPS).
- … and for a typical (but already fairly large) $\varepsilon_\infty = 10$, the ratio under study is $30/21 \approx 1.5$, thus $(E_{eff}/E_0)^2 \approx 2.25$, nothing to be worried about.

The parameters used in the simulation are given in Table 1. We used the model of Lucovsky to calculate the optical cross sections for electrons and holes, which needs the input of the four parameters: refractive index n of the semiconductor, the effective mass m_n^* and m_p^* of the carriers, and the effective field ratio E_{eff}/E_0 which represents the ratio between the electric field at the impurity and the electric field of the incident wave [8].

Fig. 1 The text fragment on the Lucovsky parameters from ref. [9] in the SCAPS manual: S. Khelifi, M. Burgelman, J. Verschraegen, A. Belghachi, "Impurity photovoltaic effect in GaAs solar cell with two deep impurity levels", *Solar Energy Materials and Solar Cells*, **92** (2008) 1559-1565.

Masouri, Kalymnos, April 21, 2016

Marc Burgelman, Honorary Professor of the University of Gent

Correspondence address:

University of Gent, Electronics and Information Systems (ELIS),

Pietersnieuwstraat 41, B-9000 Gent, "Belgium".

Marc.Burgelman@elis.ugent.be

About the local ("effective") electric field

($\rightarrow$ parameter E_{eff}/E_0 in the Lucovsky calculation of σ_{opt})

Questions by

Answers by Marc Burgelman, ELIS, University of Gent, April 21, 2016

Introduction

This document corrects and supersedes the document entitled "SCAPS and the meaning of the parameter E_{eff}/E_0 in the Lucovsky calculation of the IPV optical cross section of an impurity", dated 21 April, 2016, by Marc Burgelman. This document was correct until the sentence (4th item in the list) "to find the relation between E_{eff} and E_0, follow the treatment of 'local electric field' from standard text book chapters on electrostatics".

[My problem with that document was that I have no text books nor courses at my disposal here in my holiday apartment in Kalymnos, Greece; also, a day of cycling, walking and rock climbing does not seem to bring a person in the right condition to reconstruct some theory that he has known tens of years before… As a result, I correctly described one component of the local field (the 'cavity field'), but I totally forgot about the other component (the 'reaction field'). This is corrected in the rest of this document. MB.]

The local electric field

The electric field felt by a particular atom at its position in a material is called the local electric field E_l. Some people, e.g. Lucovsky, prefer the name 'effective electric field', and use the notation E_{eff}. Since this document is intended for SCAPS users, who want to apply Lucovsky's equation to calculate the optical capture cross section σ_{opt} of an impurity in a host semiconductor, we will also use here Lucovsky's notation E_{eff}. This field E_{eff} differs from the 'macroscopic' or 'applied' or 'external' electric field E_0 in the material because of the dielectric properties of the material. In its most simple form (uniform, linear, isotropic material), these are described by one single scalar parameter, the (relative) dielectric constant ε.

Consider one individual (IPV) impurity atom in a host material with dielectric constant ε. This impurity is subjected to the local field E_{eff} and will get a dipole moment $\boldsymbol{p}_0$.

Now, make a cavity of radius a around our impurity. Inside the cavity there is nothing (vacuum) but the single dipole $\boldsymbol{p}_0$. Hence the cavity has dielectric constant $\varepsilon = 1$. Also, chose the cavity radius a such that

$$a = a_0 \quad \text{with} \quad \frac{4\pi a_0^3}{3} = \frac{1}{N} \tag{1}$$

where N is the number of host atoms per unit volume (the density of the impurities is assumed to be much lower than N). The radius a_0 is called the Onsager radius.

Apply a uniform electric field $\boldsymbol{E}_0$ over the material.

Applying superposition:

There are two causes of the electric field E_{eff} at the position of our impurity:

1. The external field E_0. This causes a field $\boldsymbol{E}_c$ in the cavity (where our impurity atom is); that field is called the cavity field.

2. The dipole $\boldsymbol{p_0}$. Of course we do not mean here directly the field of that dipole (that is infinite at the position of the dipole!): a dipole does not feel the field caused by itself. But the dipole $\boldsymbol{p_0}$ causes a field, that polarises the (assumed) homogeneous material ε surrounding the cavity, and this polarised material causes a field at the position of the dipole; the dipole 'feels' this field. This field is called the 'reaction field' $\boldsymbol{E_r}$.

This superposition of cavity field and reaction field is shown in Fig. 1.

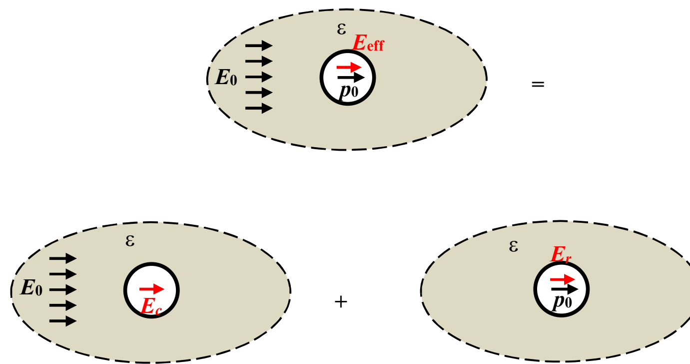

Fig. 1 The local field E_{eff} is a superposition of the cavity field E_c and the reaction field E_r. Note that the homogeneous host material with dielectric constant ε is infinitely large compared to the single-atom sized cavity.

<u>Superposition part 1: the cavity field E_c</u>

This is really a standard electrostatic problem: it has been countless times an examination question for bachelor students! The electric field inside the cavity uniform, and it does not depend on the radius of the cavity. It is given by:

$$\boldsymbol{E_c} = \boldsymbol{E_0} \cdot \frac{3\varepsilon}{2\varepsilon+1} \tag{2}$$

<u>Superposition part 2: the reaction field E_r</u>

This is still a standard electrostatic problem, but maybe a little more advanced than the previous problem. The result is that the field inside the cavity is uniform and given by E_r; the field outside the cavity is a dipole field, as caused by a dipole p that is proportional to $\boldsymbol{p_0}$ (not further relevant here). The reaction field E_r is given by:

$$\boldsymbol{E_r} = \frac{\boldsymbol{p_0}}{4\pi a^3 \varepsilon_0} \frac{2(\varepsilon-1)}{2\varepsilon+1} \tag{3}$$

<u>Result of the superposition : the local or effective field E_{eff}</u>

Thus, we find for the local field E_{eff}:

$$\boldsymbol{E_{eff}} = \boldsymbol{E_c} + \boldsymbol{E_r} = \boldsymbol{E_0} \cdot \frac{3\varepsilon}{2\varepsilon+1} + \frac{\boldsymbol{p_0}}{4\pi a^3 \varepsilon_0} \frac{2(\varepsilon-1)}{2\varepsilon+1} \quad (4)$$

And when a was chosen as the Onsager radius a_0, applying Eq. (1), we find:

$$\boldsymbol{E_{eff}} = \boldsymbol{E_0} \cdot \frac{3\varepsilon}{2\varepsilon+1} + \frac{N\boldsymbol{p_0}}{3\varepsilon_0} \frac{2(\varepsilon-1)}{2\varepsilon+1} \quad (5)$$

Now it remains to assign a value to $\boldsymbol{p_0}$. If our impurity atom were (dielectrically spoken) just like a host atom, then the individual atomic dipole moment $\boldsymbol{p_0}$ is linked to the macroscopic polarization $\boldsymbol{P}$ simply by $\boldsymbol{P} = N\boldsymbol{p_0}$. But our impurity atom can be different: it can have a polarizability α_{impurity} that is different from the polarizability of the host material atoms, α_{host}. (Polarizability is the proportionality between individual dipole moment and local electric field, in a linear material). We then get:

$$p_0 = p_{\text{impurity}} = \alpha_{\text{impurity}} \cdot E_{eff} = \frac{\alpha_{\text{impurity}}}{\alpha_{\text{host}}} \cdot \alpha_{\text{host}} \cdot E_{eff} = \frac{\alpha_{\text{impurity}}}{\alpha_{\text{host}}} \cdot p_{\text{host}} = \frac{\alpha_{\text{impurity}}}{\alpha_{\text{host}}} \frac{P}{N} \quad (6)$$

For simplicity we just take $\alpha_{\text{impurity}} = \alpha_{\text{host}}$ here, thus simply

$$N\boldsymbol{p_0} = \boldsymbol{P} \quad (7)$$

We thus finally get:

$$\boldsymbol{E_{eff}} = \boldsymbol{E_0} \cdot \frac{3\varepsilon}{2\varepsilon+1} + \frac{\boldsymbol{P}}{3\varepsilon_0} \frac{2(\varepsilon-1)}{2\varepsilon+1} \quad (8)$$

Here, the macroscopic polarization $\boldsymbol{P}$ is related to the macroscopic electric field $\boldsymbol{E_0}$ by the simple relation (linear, isotropic, uniform)

$$P = (\varepsilon-1)\varepsilon_0 E_0 \quad (9)$$

and thus:

$$\begin{aligned}
\boldsymbol{E_{eff}} &= \boldsymbol{E_0} \cdot \frac{3\varepsilon}{2\varepsilon+1} + \frac{(\varepsilon-1)\varepsilon_0 \boldsymbol{E_0}}{3\varepsilon_0} \frac{2(\varepsilon-1)}{2\varepsilon+1} \\
&= \boldsymbol{E_0} \cdot \frac{1}{3(2\varepsilon+1)} \left[9\varepsilon + 2(\varepsilon-1)^2 \right] \\
&= \boldsymbol{E_0} \cdot \frac{2\varepsilon^2 + 5\varepsilon + 2}{3(2\varepsilon+1)} = \boldsymbol{E_0} \cdot \frac{2\varepsilon^2 + \varepsilon + 4\varepsilon + 2}{3(2\varepsilon+1)} \\
&= \boldsymbol{E_0} \cdot \frac{\varepsilon(2\varepsilon+1) + 2(2\varepsilon+1)}{3(2\varepsilon+1)} = \boldsymbol{E_0} \cdot \frac{(\varepsilon+2)(2\varepsilon+1)}{3(2\varepsilon+1)} \\
&= \boldsymbol{E_0} \cdot \frac{\varepsilon+2}{3}
\end{aligned} \quad (10)$$

You could arrive faster at this equation when you remember the Lorentz equation for the local field

$$E_{\text{local}} = E_0 + \frac{P}{3\varepsilon_0} \text{ (Lorentz equation)} \quad (11)$$

and then apply (9).

Conclusion

The ratio r between the local or effective field, and the applied field E_0 in the Lucovsky equation is thus:

$$r = \frac{E_{eff}}{E_0} = \frac{\varepsilon + 2}{3} \quad (12)$$

This expression should replace the erroneous result in my previous document (based on the cavity field alone).

The other remarks remain in order:

- mind that it is about optical electric fields, not static electric fields. Hence, do not use the static dielectric constant ε_s, but the optical dielectric constant (at wavelength λ) ε_∞, that can usually be approximated by the square of the refractive index n.
- in our own IPV/SCAPS articles, we simply took $E_{eff}/E_0 = 1$ (… a bit lazy, though… ☺)
- mind that in the Lucovsky equation, this $r = E_{eff}/E_0$ ratio is squared and then enters as a pre-factor in the calculation of σ_{opt}. Since such capture cross section is a property of 'logarithmic nature' (it can vary over many orders of magnitude), a small variation is not suspected to influence e.g. solar cell parameters substantially at all (but you can check that easily with SCAPS).
- when $\varepsilon = 1$ (the material has no dielectric properties), $r = 1$, as expected.
- when $\varepsilon \to \infty$, also $r \to \infty$.
- … and for a typical (but already fairly large) $\varepsilon_\infty = 10$, the ratio under study is $12/3 \approx 4$, thus $(E_{eff}/E_0)^2 = 16$. Whether this has some influence, or is nothing to be worried about, should further be checked for your SCAPS problem, by you.

Masouri, Kalymnos, April 23, 2016

Marc Burgelman, Honorary Professor of the University of Gent

Correspondence address:

University of Gent, Electronics and Information Systems (ELIS),

Pietersnieuwstraat 41, B-9000 Gent, "Belgium".

Marc.Burgelman@elis.ugent.be

C.2 On the Implemetation of the Lucovsky Model in SCAPS

Received via e-mail from Marc Burgelman on the 24th of February, 2021.

SCAPS and the implementation of the Lucovsky equation for σ_{IPV}

Question by Tore Skauge Bysting, Norwegian University of Science and Technology, Trondheim, Norge, 24-2-2021

Answer by Marc Burgelman, formerly ELIS, UGent, "Belgium", 24-2-2021

1. Summary of the question

In the simulation of the impurity photovoltaic effect (IPV) one needs to know the optical capture cross sections of the IPV impurity for electrons and holes, $\sigma_{opt,n}$ and $\sigma_{opt,p}$. The SCAPS Manual, and also our publications, state that $\sigma_{opt,n}$ and $\sigma_{opt,p}$ are calculated using the model of Lucovsky [1]. However, Tore S. B. pointed out that Eq. [3] of [1] has not the correct dimension of m^2 for σ_{opt}: it gets the correct dimension of m^2 only when a dielectric permittivity is added to the denominator of the equation [3]. Now several questions are risen by Tore:

- which permittivity? The vacuum permittivity ε_0 only, or the material permittivity $\varepsilon_r\varepsilon_0$?
- if it should be the material permittivity, which ε_r-value is to be taken?
- and what exactly is SCAPS using?

2. The IPV capture cross section according to Lucovsky

The Lucovsky equation (Eq. (3) of [1]) is:

$$\sigma_{opt} = \frac{1}{n}\left(\frac{E_{eff}}{E_0}\right)^2 \frac{16\pi q^2\hbar}{3m^* c} \frac{E_i^{1/2}\left(\hbar\omega - E_i\right)^{3/2}}{\left(\hbar\omega\right)^3} \tag{1}$$

SCAPS uses this equation, but in the formulation of Güttler and Queisser [2].

3. The IPV capture cross section according to Güttler and Queisser

The formulation by Güttler is given in Eq. (2) and Eqs. (3a to 3c) of [2].

$$\sigma_{opt} = \sigma_0 \cdot M \cdot Y \cdot \left(X-1\right)^{3/2} \cdot X^{-3} \tag{2}$$

with:

$$\sigma_0 = \frac{4q^2\hbar}{3\varepsilon_0 m_0 c} \cdot \frac{1}{1\ \text{eV}} = 0.93\times10^{-16}\ \text{cm}^2 \tag{3}$$

$$M = \frac{1}{n}\left(\frac{E_{eff}}{E_0}\right)^2 \frac{m_0}{m^*} \frac{1\ \text{eV}}{E_g} \tag{4}$$

$$X = \frac{\hbar\omega}{E_i} \quad \text{and} \quad Y = \frac{E_g}{E_i} \tag{5}$$

Here, M, X and Y are dimensionless, and σ_0 has the correct dimension of m^2 (or cm^2 when you like). SCAPS takes the numerical value given by Güttler (Eq. (3) here), and gets the other parameters n, m^*/m_0, E_{eff}/E_0, E_i and E_g from its input panels, and $\hbar\omega$ from the wavelength λ:

$$\hbar\omega = h\nu = \frac{hc}{\lambda} = \frac{1240\ \text{nm}\times\text{eV}}{\lambda} \tag{6}$$

4. The correspondence between Lucovsky and Güttler

After inserting the parameters σ_0, M, X and Y (Eq. (3) to (5)) in Eq. (2), one gets the Güttler equation

$$\sigma_{\text{opt, Guettler}} = \frac{4q^2}{3\varepsilon_0 c}\frac{1}{m^*}\frac{1}{n}\left(\frac{E_{\text{eff}}}{E_0}\right)^2 \hbar \frac{E_i^{1/2}\left(\hbar\omega - E_i\right)^{3/2}}{\left(\hbar\omega\right)^3} \quad (7)$$

Now we can compare

$$\sigma_{\text{opt, Guettler}} = \frac{1}{\varepsilon_0} \times \text{Residue} \quad (8)$$

with

$$\sigma_{\text{opt, Lucovsky}} = 4\pi \times \text{Residue} \quad (9)$$

or with a little rewriting (4πResidue = residue):

$$\sigma_{\text{opt, Guettler}} = \frac{1}{4\pi\varepsilon_0} \times \text{residue and } \sigma_{\text{opt, Lucovsky}} = 1 \times \text{residue} \quad (10)$$

Now the difference/correspondence is clear: Güttler uses 'normal' SI units, and Lucovsky uses an old and now obsolete unit system (I think without looking up, cgs system, but do not take me on this. The "Güttler unit system" (it is SI) is 'rationalised', meaning that a factor $1/4\pi\varepsilon_0$ appears in Coulomb's law, but that Maxwell/Gauß equation looks simplier, without a 4π intervening (e.g. $\varepsilon_0 \nabla \cdot E = \rho$). The older "Lucovsky unit system" (non-rationalised; cgs?) has a simpler Coulomb equation ($F = q_1 q_2 / r^2$) but then gets a 4π in Gauß' equation.
By now, these older unit systems, and the motivations/ways to 'rationalise' them has more or less disappeared in the mist of times (fortunately!), and nowadays students (you?) have been only confronted with SI. In my first university year (1970…), we learned about non-rationalised MKSA (for curiosity) and SI (to use), and CGS was already folklore…
And now a happy (?) circumstance for you: The difference between Lucovsky and the SI version of it by Güttler is, after inserting a factor ε_0 in the denominator, as you guessed) exactly a factor 4π… and $4\pi = 12.57$… not too far away from the relative ε_r =13.1 value of GaAs that you used in your numerical experiments… clear now why working with this ε_r was the best of your try-outs? ☺.

5. The actual implementation in SCAPS

And now a glimpse of the sacrosanct, top-secret (☺) SCAPS source code (well, some20lines out of the 120.000 lines program…).
The affix _us to variables (Eg_us, Ei_us) means 'unscaled' (for use in the user interface and input/output), thus in this case in units of eV, and not made dimensionless by scaling to kT (for use in all other calculations). The variable LAMBDA_1_eV_PHOTON = 1240 nm×eV is used in Eq. (6) here (SCAPS uses 1239.977 instead of 1240…). Also, we use the numerical factor from Güttler (Eq. (3)), for m^2 instead of cm^2. And as you can guess, the fields n, m, E and Ei of the data structure optCaptProps stand for our parameters n, m^*/m_0, E_{eff}/E_0 and E_i above.

```
/******** begin function ReadOpticalCaptureParametersFromModel ******************/
void ReadOpticalCaptureParametersFromModel(double Eg_us, double Ei_us, opticalCaptureProperties *optCaptProps)
{
 // in this f=unction, Ei is (should be) the impurity level measured "above EV"
 // grading: when Eg is graded, should optCaptProps->sigmas also become a function of grading?
 // still to implement MB 5-3-2009
 // this is the equation of Lucovsky
 double lambdaMin, lambdaMax;
 double X, Y;
 int i;

 lambdaMin = LAMBDA_1eV_PHOTON/optCaptProps->Emax;
 lambdaMax = LAMBDA_1eV_PHOTON/Ei_us;

 if(lambdaMin > lambdaMax)
   optCaptProps->nWavelengths = 0;
 else
   optCaptProps->nWavelengths = 50;

 optCaptProps->sigmas      = (double *)realloc (optCaptProps->sigmas     , optCaptProps->nWavelengths * sizeof (double));
 optCaptProps->wavelengths = (double *)realloc (optCaptProps->wavelengths, optCaptProps->nWavelengths * sizeof (double));
 if (optCaptProps->nWavelengths != 0)
   {
   Y=Eg_us/Ei_us;
   assert (optCaptProps->sigmas      != NULL);
   assert (optCaptProps->wavelengths != NULL);
   for(i=0; i<optCaptProps->nWavelengths; i++)
     {
     optCaptProps->wavelengths[i] = (lambdaMin*(double)(optCaptProps->nWavelengths-i-1)+lambdaMax*(double)i)/
                                    (double)(optCaptProps->nWavelengths-1);
     X = LAMBDA_1eV_PHOTON/optCaptProps->wavelengths[i]/Ei_us;
     if (X < 1.0)
       X = 1.0;   // avoid trouble in the square-root of (X-1) below
     optCaptProps->sigmas[i] = 0.93e-20 * optCaptProps->E * optCaptProps->E / (optCaptProps->n*optCaptProps->m * Eg_us) *
                               Y * sqrt(pow (X-1.0, 3.0)) * pow (X, -3.0);
     }
   }
}
/******** begin function ReadOpticalCaptureParametersFromModel ******************/
/********************************************************************************/
```

6. References

[1] G. Lucovsky, “On the photoionization of deep impurity centers in semiconductors”, *Solid State Communications*, **3-9**, pp. 299–302, 1965.

[2] G. Güttler and H. Queisser, “Impurity photovoltaic effect in silicon”, **10**, 51-55,1970

C.3 On the Implemetation of the IPV Effect in SCAPS

Received via e-mail from Marc Burgelman on the 19th of August, 2021.

Implementation in SCAPS of the Impurity Photovoltaic effect (IPV)

Marc Burgelman
(formerly) Department of Electronics and Information Systems (ELIS), University of Gent
17-8-2021

1. Introduction

In our ELIS Lab, the IPV effect was studied by Samira Khelifi and Johan Verschraegen, and the implementation in SCAPS was by Johan Verschraegen. This document on the implementation of the Impurity Photovoltaic effect in SCAPS is based on the doctorate's theses of Samira[1] and Johan[2], on some basic articles, e.g. an article by Keevers and Green[3], and general textbook treatments of Shockley-Read-Hall (SRH) recombination.

2. General IPV equations

From the doctorate's thesis of Samira Khelifi [1], we take:

$$U = \frac{np - (n_1 + \tau_{n0} g_{nt})(p_1 + \tau_{po} g_{pt})}{\tau_{no}(p + p_1 + \tau_{p0} g_{pt}) + \tau_{po}(n + n_1 + \tau_{n0} g_{nt})} \tag{1}$$

with

$$\tau_{n0} = \frac{1}{c_n N_t} \text{ and } \tau_{p0} = \frac{1}{c_p N_t} \tag{2}$$

$$n_1 = N_C e^{-(E_C - E_t)/kT}, \; p_1 = N_V e^{-(E_t - E_V)/kT} \tag{3}$$

$$g_{nt}(x) = N_t \int_{\lambda_{n\min}}^{\lambda_{n\max}} \sigma_n^{opt}(x,\lambda) \phi_{ph}(x,\lambda) d\lambda \tag{4}$$

$$g_{pt}(x) = N_t \int_{\lambda_{p\min}}^{\lambda_{p\max}} \sigma_p^{opt}(x,\lambda) \phi_{ph}(x,\lambda) d\lambda \tag{5}$$

$$\phi_{ph}(x,\lambda) = \phi_{ext}(\lambda) \frac{1 + R_b e^{-2\alpha_{tot}(\lambda)(L-x)}}{1 - R_f R_b e^{-2\alpha_{tot}(\lambda)L}} e^{-\alpha_{tot}(\lambda)x} \tag{6}$$

Here $\phi_{ph}(x, \lambda)$ is the position and wavelength dependent light flux in the solar cell. The position dependent functions $g_{nt}(x)$ and $g_{pt}(x)$ describe the IPV generation terms. They are in units of $cm^{-3}s^{-1}$, thus the terms $\tau_{n0}g_{nt}$ and $\tau_{p0}g_{pt}$ in Eq. (1) are in cm^{-3}, as should be.

The total absorption coefficient is the sum of all absorption processes in the cell:

$$\alpha_{tot}(\lambda) = \alpha_{e-h}(\lambda) + \alpha_n(\lambda) + \alpha_p(\lambda) + \alpha_{fc}(\lambda) \tag{6}$$

where $\alpha_{e\text{-}h}(\lambda)$ the band-to-band absorption coefficient, and $\alpha_n(\lambda)$ and $\alpha_p(\lambda)$ are the defect absorption coefficients given by:

$$\alpha_n(\lambda) = f_t N_t \sigma_n^{opt}(\lambda) \text{ and } \alpha_p(\lambda) = (1 - f_t) N_t \sigma_p^{opt}(\lambda) \tag{7}$$

with f_t is the occupation probability of the impurity level. The free carrier absorption $\alpha_{fc}(\lambda)$ is given by

$$\alpha_{fc}(\lambda) = C_{fc}^n \lambda^2 n + C_{fc}^p \lambda^2 p \tag{8}$$

where C_{fc}^n and C_{fc}^p are empirical parameters. Free carrier absorption is not included in SCAPS.

All other symbols here have their usual (or intuitive) meaning. In particular, n_1 and p_1 are the electron and hole densities "when the Fermi level coincides with the trap level". These properties are often denoted as n_t and p_t in text books and other literature. It follows that

$$n_1 p_1 = n_i^2 \tag{9}$$

These equations were taken mainly from the work of Keevers and Green [3]. The notations of Keevers are slightly different. Also, Keevers inserts a numerical factor 2.0 in equations (4) and (5), with the motivation: "*The factor* 2 *is a geometrical factor to account for the oblique passage of light due to the texture of the cell surface*". This factor is not applied in SCAPS.

3. IPV equations as they are used in SCAPS

To describe the implementation of IPV in SCAPS, we will use the notations of Keevers[3]. We add here some explanation that should make this text readable in itself.

Recombination in the bulk of the cell is described using the Shockley-Read-Hall formalism. The standard SRH-equations are however adapted in order to be able to implement the IPV-effect, giving rise to extra terms g_{max} which are zero when no IPV is present.

With N_t and f_t the concentration and occupation probability of the defect levels, the recombination rates for holes and electrons are respectively given by (10). Most properties used below are functions of position x, notably R_n, R_p, n, p, $g_{n,\max}$, $g_{p,\max}$, n_t, p_t. Also the defect density N_t is a function of position x when grading is defined for this property in the SCAPS problem definition. We will omit the x-dependence in order not to overload the notations.

The final rate equations for electrons and holes are:

$$\begin{aligned} R_n &= N_t c_n \left(n(1 - f_t) - n_t f_t\right) \\ R_p &= N_t c_p \left(p f_t - p_t (1 - f_t)\right) \end{aligned} \tag{10}$$

Here we used:

$$\begin{aligned} n_t &= N_C \exp\left(-\frac{E_C - E_t}{kT}\right) + \frac{g_{n,\max}}{c_n} = n_1 + \frac{g_{n,\max}}{c_n} \\ p_t &= N_V \exp\left(-\frac{E_t - E_V}{kT}\right) + \frac{g_{p,\max}}{c_p} = p_1 + \frac{g_{p,\max}}{c_p} \end{aligned} \tag{11}$$

thus $n_1 p_1 = n_i^2$ but $n_t p_t \neq n_i^2$ when IPV is active, thus $g_{\max} \neq 0$

with c_n and c_p the capture constants for electrons and holes (both in cm^3s^{-1}). From the usual treatment of SRH recombination in text books we take the capture constants

$$c_n = v_{th,n}\sigma_n \quad \text{and} \quad c_p = v_{th,p}\sigma_p \tag{12}$$

The capture cross sections σ_n and σ_p, and the thermal velocities $v_{th,n}$ and $v_{th,p}$ are input parameters in SCAPS.

Note that the meaning of n_t and p_t in (11) deviates from a more common meaning in text books, where $n_t = n_1$ and $p_t = p_1$ is the usual meaning. The notation n_t and p_t here corresponds to n_1^* and p_1^* in Keevers article [3].

4. Derivation of Eq. (10)

Eqs. (10) follows from expressions for the detailed capture and emission processes. We denote a capture rate with C and an emission rate with E (both are in units of $cm^{-3}s^{-1}$). We give the subscripts n and p to denote electrons and holes. The superscript "opt" and "th" denote an optical process (here IPV) and a thermal process. The partial mechanisms are thus:

$C_n^{th} = N_t c_n n(1-f_t)$ thermal capture of electrons from the CB into the defect (13)

$E_n^{th} = N_t e_n f_t$ thermal emission of electrons from a defect to the CB (14)

$E_n^{opt} = N_t f_t g_{n,\max}$ optical emission of electrons from a defect (IPV) to the CB (15)

$C_p^{th} = N_t c_p p f_t$ thermal capture of holes from the VB into the defect (16)

$E_p^{th} = N_t e_p(1-f_t)$ thermal emission of holes from defect to the VB (17)

$E_p^{opt} = N_t(1-f_t)g_{p,\max}$ optical emission of holes from a defect (IPV) to the VB (18)

Here e_n and e_p are the emission constants (both in s^{-1}). The IPV generation is described here by the parameters $g_{n,\max}$ and $g_{p,\max}$; both are in s^{-1}. The relation between the $g_{\max}$ parameters here, and the g_{nt} and g_{pt} in Samira's doctorate is thus:

$$g_{n,\max} = \tau_{n0}c_n\, g_{nt} = \frac{g_{nt}}{N_t} \quad \text{and} \quad g_{p,\max} = \tau_{p0}c_p\, g_{pt} = \frac{g_{pt}}{N_t} \tag{19}$$

Note that there are each times (thus for electrons and for holes) two emission processes (thermal and optical or IPV), but only one capture process (only thermal capture, "optical capture" does not exist).

From Eq. (13) to (18) we can deduce the net electron and holes recombination rates:

$$R_n = C_n^{th} - E_n^{th} - E_n^{opt} \tag{20}$$

$$R_p = C_p^{th} - E_p^{th} - E_p^{opt} \tag{21}$$

In thermodynamical equilibrium, $R_n = R_p = 0$ (the principle of "detailed balance"). Also, in thermal equilibrium there is no illumination and thus no IPV, thus $g_{n,\max} = g_{p,\max} = 0$. This leads to the relation between the capture constants c and the emission constants e:

$$\begin{aligned} e_n &= c_n n_1 \\ e_p &= c_p p_1 \end{aligned} \tag{22}$$

Outside thermal equilibrium (thus when a voltage and/or illumination are applied), but in steady-state, it is required that $R_n = R_p$. This can be used to determine the occupation probabilities of the defect (occupation f_t with electrons, and 1-f_t with holes). We get:

$$f_t = \frac{c_n n + e_p + g_{p,\max}}{c_n n + e_n + c_p p + e_p + g_{p,\max} + g_{n,\max}} \tag{23}$$

$$1 - f_t = \frac{c_p p + e_n + g_{n,\max}}{c_n n + e_n + c_p p + e_p + g_{p,\max} + g_{n,\max}} \tag{24}$$

[SCAPS always calculates both f_t from Eq. (23) and 1-f_t from Eq. (24) to avoid numerical instabilities associated with subtraction of two nearly equal numbers; these could occur when f_t is either very close to zero or very close to unity].

With Eqs. (22) for the emission constants and Eqs. (11) for n_t and p_t, the equations (23) and (24) for the occupation probabilities can also be written as:

$$f_t = \frac{c_n n + c_p p_t}{c_n n + e_n + c_p p + e_p + g_{p,\max} + g_{n,\max}} \tag{25}$$

$$1 - f_t = \frac{c_p p + c_n n_t}{c_n n + e_n + c_p p + e_p + g_{p,\max} + g_{n,\max}} \tag{26}$$

Now we can write the total recombination U of the defect (SRH + IPV) as $U_{\text{SRH}} = R_n = R_p$. Using equations (10), (25) and (26), we get:

$$\begin{aligned} U_{\text{SRH}} = R_n = R_p &= N_t c_n c_p \frac{np - n_t p_t}{c_n n + e_n + c_p p + e_p + g_{p,\max} + g_{n,\max}} \\ &= N_t c_n c_p \frac{np - n_t p_t}{c_n \left(n + n_1\right) + c_p \left(p + p_1\right) + g_{p,\max} + g_{n,\max}} \end{aligned} \tag{27}$$

When one substitutes the equations (11) for n_t and p_t, we get Eq. (1) from Samira's doctorate.

Note that the numerator of Eq. (27) does not contain the familiar expression

$$np - n_1 p_1 = np - n_i^2 \tag{28}$$

but contains also IPV terms in $g_{n,\max}$ and $g_{p,\max}$. Nevertheless, $U = 0$ at thermal equilibrium since the $g_{\max}$ terms are zero in dark.

5. Comparison with the traditional Shockley-Read-Hall expression (without IPV)

The traditional SRH expression is

$$U_{SRH} = N_t c_n c_p \frac{np - n_i^2}{c_n(n+n_1) + c_p(p+p_1)} \tag{29}$$

Compared to the full expression (SRH_IPV) of Eq. (27), there is not only a simplification of the denominator (the IPV terms in $g_{\max}$ are dropped out), but also in the numerator (the term $n_i^2 = n_1 p_1$, instead of $n_t p_t$).

6. Intermezzo: a note on band-to-band processes in SCAPS

The processes discussed so far are interactions between the band (edges) and the defect. There are additional band-to-band processes possible (thus directly between valence band (edge) and conduction band (edge). Again, there are two emission processes: optical (this is the optical generation of *eh* pairs) and thermal (that is the inverse process of "band-to-band recombination" or "radiative recombination"). But there is only one capture process: the thermal band-to-band recombination. Necessarily, in band-to-band processes all electron rates are equal to hole rates. Thus, the partial processes are (taking the superscript "band-to-band"; we do not use "radiative", since band-to-band recombination can also be non-radiative):

$$C_n^{\text{band-to-band, th}} = C_p^{\text{band-to-band, th}} = K_r pn \tag{30}$$

$$E_n^{\text{band-to-band, th}} = E_p^{\text{band-to-band, th}} = K_r p_0 n_0 = K_r n_i^2 \tag{31}$$

(here n_0 and p_0 are equilibrium densities, and n_i the intrinsic carrier density).

$$E_n^{\text{band-to-band, opt}} = E_p^{\text{band-to-band, opt}} = G \tag{32}$$

where G is the (optical *eh* pair) generation rate, and is an important input property to set in SCAPS: it is set either directly as $G(x)$ (file or model), or by defining the incident light flux (spectrum (file or model), neutral density and/or cut-off filters) and the absorption constant $\alpha(\lambda)$ in all layers (file or model).

It follows that the net band-to-band recombination rate is:

$$U^{\text{band-to-band}} = C^{\text{band-to-band}} - E^{\text{band-to-band}} = K_r\left(pn - n_i^2\right) \tag{33}$$

Thus, to describe all band-band and band-defect interactions, there are nine basic (sub)processes, not twelve (since there is only thermal capture, not "optical capture").

SCAPS also implements a second band-to-band recombination/generation process: Auger recombination, which involves either two holes and one electron, or two electrons and on hole. See the SCAPS User Manual[4].

7. Displaying and visualising the recombination and IPV terms in SCAPS

The easiest way to visualise and display is to do at least one single shot simulation, and then go to the Generation/Recombination Profiles Panel. When one is interested in IPV, the simulation should be with the illumination switched on; a work point simulation is enough (a full *IV* or *QE* simulation is not needed). In the top left part of this panel, one can click off or on the display of several gen/rec curves, see Fig. 1. Each curve is displayed in the colour of the legend label of Fig. 1, so e.g. the *eh* generation rate $G(x)$ is displayed in light green, when

ordered. We admit that the legend text is not always clear or intuitive (e.g. the labels *Gross IPV Generation* and *Net Generation*), however the meaning is clarified in our Manual[4]. When toggling (checking or unchecking) one of the check boxes, the corresponding curve is drawn or not; however, the information of this curve, in a table form, is always listed (clicking the *show* or *save* buttons), regardless the state of the check box.

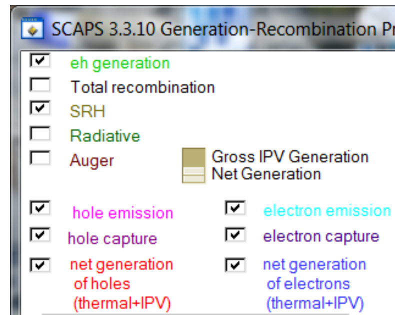

Fig. 1 Options for displaying total and partial recombination and generation, capture and emission curves in the *Generation-Recombination Profiles* Panel of SCAPS.

The correspondence between the labels in the SCAPS Gen/Rec Panel, the SCAPS Manual and the notation and equations in this document is given in below.

Table 1 Graphs that can be displayed in the Generation-Recombination Panel: correspondence of terminology

SCAPS User Interface: Generation-Recombination Profiles Panel	SCAPS User Manual Section 6.6, Table 6.4	This document	
eh generation	G_{eh}	$G(x)$	
Total recombination	Total recombination	U_{tot}	
SRH	SRH recombination	U_{SRH} ,	(27)
Radiative	Radiative recombination	$U^{\text{band-to-band}}$	(33)
Auger	Auger recombination		
hole emission	G_{pth}	E_p^{th}	(21)
hole capture	R_{pth}	C_p^{th}	(21)
electron emission	G_{nth}	E_n^{th}	(20)
electron capture	R_{nth}	C_n^{th}	(20)
"Gross IPV Generation" selected			
gross generation of holes (IPV only)	IPV G_p	E_p^{opt}	(21)

gross generation of holes (IPV only)	IPV G_n	E_n^{opt} (20)
"Net Generation" selected		
net generation of holes (thermal+IPV)	net G_p	$R_p = C_p^{th} - E_p^{th} - E_p^{\text{opt}}$ (21)
net generation of electrons (thermal+IPV)	net G_n	$R_n = C_n^{th} - E_n^{th} - E_n^{\text{opt}}$ (20)

8. Correction of a bug

In Eq. (27) we stated that $U_{\text{SRH}} = R_n = R_p$, meaning that the curves U_{SRH} , R_n and R_p should coincide. Tore Skauge Bysting of Norges Teknisk-Naturvitenskapelige Universitet (NTNU), Trondheim, Norway pointed out that the curves for U_{SRH} and R_n indeed coincide, but that the curve for R_p deviates, both in the graph and in the output table of SCAPS (12-8-2021; *takk for at du varslet oss, Tore!*).

The bug could be found, as one erroneous letter in one line of the 120.000 lines of SCAPS code… In the one line implementing E_p^{opt} with Eq.(18) (for the output graph), $g_{\mathbf{n},\max}$ was used instead of $g_{\mathbf{p},\max}$. The bug was quickly corrected of course, but one will need to update to the most scaps3310.exe dated 19-8-2021 (or later). When one has SCAPS 3.3.10, simply copying the file will do the job (no new installation is needed). For earlier versions of SCAPS also the gui3310.uir file, the script description file (and possibly also the .dll and .lib) file will have to be updated (by copying) also – or SCAPS 3.3.10 should be installed instead, before updating just the exe file. And those who decide not to look to the E_p^{opt} or R_p curves, do not have to do anything ☺.

It was checked that the bug only affects the output graph and output table of E_p^{opt} and R_p (that contains E_p^{opt}). In the SCAPS simulation itself, directly the expression Eq. (27) for U_{SRH} is used (and that is implemented correctly).

References

[1] S. Khelifi, "Characterization and modelling with SCAPS of the performance of solar cells", Ph.D. thesis, Universiteit Gent, 2010. Promoter: Marc Burgelman.

[2] J. Verschraegen, "Karakterisering en modellering met SCAPS van de CISCuT dunne-filmzonnecel" (in Dutch), Ph.D. thesis, ELIS, Universiteit Gent, 2006. Promoter: Marc Burgelman.

[3] M.J. Keevers and M.A. Green, "Efficiency improvements of silicon solar cells by the impurity photovoltaic effect", *Journal of Applied Physics*, **75/8** (1994) 4022-4031.

[4] Alex Niemegeers, Marc Burgelman, Koen Decock, Johan Verschraegen, Stefaan Degrave, "SCAPS Manual", Department of Electronics and Information Systems (ELIS), University of Gent, Belgium. This document is regularly updated. Latest version so far: 8-4-2021.

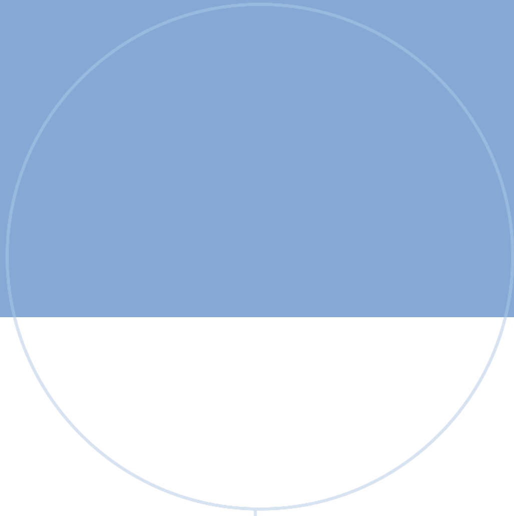

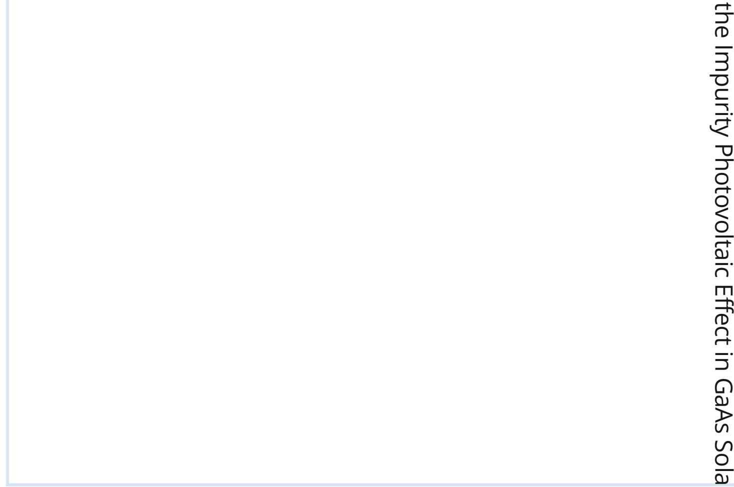

Tore Skauge Bysting

Simulation of the Impurity Photovoltaic Effect in GaAs Solar Cells

NTNU
Norwegian University of
Science and Technology